Structural Design and Control of High Performance Optical Delay Lines

by

Christopher G. Park

S.B. Massachusetts Institute of Technology (1989)

SUBMITTED TO THE DEPARTMENT OF
AERONAUTICS AND ASTRONAUTICS
IN PARTIAL FULFILLMENT OF THE REQUIREMENTS
FOR THE DEGREE OF

S.M.

at the

Massachusetts Institute of Technology

September, 1995

Signature of Author _____
Department of Aeronautics and Astronautics
August 18, 1995

Certified by _____
David W. Miller
Thesis Advisor, Principal Research Scientist, Department of Aeronautics and Asronautics

Accepted by _____
Professor Harold Y. Wachman
Chairman, Departmental Graduate Committee

Structural Design and Control of High Performance Optical Delay Lines

by

Christopher G. Park

SUBMITTED TO THE DEPARTMENT OF AERONAUTICS AND ASTRONAUTICS
ON AUGUST 18, 1995, IN PARTIAL FULFILLMENT OF THE
REQUIREMENTS FOR THE DEGREE OF
S.M.

The role of space-based interferometry in achieving astronomical goals of the 21st century, including precise mapping of the celestial sphere and detecting extra-solar planets, requires an infusion of advanced technology beyond that used in ground-based systems. High performance optical delay lines, which are used in many interferometers to control the optical pathlength difference to nanometer levels, need to be developed from a multi-disciplinary perspective in order to overcome optical pathlength disturbances which arise from increased system flexibility in space-based interferometers. This work utilizes a combined control-structure approach to investigate several optical delay line (ODL) structural design issues, including identifying good suspension characteristics, understanding the limitation of actuation noise and device staging, and posing the problem in an efficient framework to attain desired overall device characteristics in the presence of optical disturbance rejection. To complement the analytical work, the JPL Phase B optical delay line is used as an operationally proven device, which is traceable to both past and future optical delay lines, with which to investigate real performance limitations. Such limitations are studied by conducting a detailed characterization of the structure as well as by examining successively higher authority controllers. Finally, several other optical and mechanical design issues are qualitatively discussed as a completion to ODL design issues. Due to the vast number of topics in ODL design, high performance optical delay line design and evaluation must be conducted from a multi-disciplinary perspective which blends control, structure, sensor, and actuator technologies.

Thesis Supervisor: Dr. David W. Miller
Principal Research Scientist, Aeronautics and Astronautics

Acknowledgments

I would like to thank Gary Blackwood (JPL) for his tremendous support over the past two years in understanding the optical delay line problem. In addition, the help from others at JPL including Mark Colavita, Brad Hines, and Rob Calvet is greatly appreciated. The JPL Phase B ODL, loaned from Bob Laskin and Mike Shao at JPL, proved to be an invaluable asset to this thesis work. I hope it gets back to JPL sometime this century.

On the MIT SERC side of the continent, I appreciate the tolerance of all those who read parts of my thesis and helped me to really understand what I was doing.

Now I can re-introduce myself to my wife, Renie, and finally meet my daughter, Mariah, who appeared just as the thesis work became frantic.

This work was sponsored by a MIT NASA Code X Space Engineering Research Center grant.

Contents

List of Figures

List of Tables

Chapter 1

Introduction

Interferometers operating in the ultraviolet, visible, and infrared spectral bands represent the next great leap forward in space-based astronomy and astrophysics. As stated in the Bahcall Report [1], interferometry is the only method known to improve by orders of magnitude the angular resolution of current astronomical telescopes and thereby meet several key astronomical goals of the 21st century: extra-solar planet detection, precise measurement of galactic and cosmic distance scales, measurement of stellar diameters, and the resolution of close binary star systems.

Several interferometer concepts are currently being considered by NASA. The Astrometric Interferometer Mission (AIM) is the next mission slated after the Space Infrared Telescope Facility (SIRTF). The Orbiting Stellar Interferometer (OSI) of the Jet Propulsion Laboratory (JPL) and the Precision Optical Interferometer in Space (POINTS) of the Smithsonian Astronomical Observatory are the leading candidates for AIM, whose science goal is to map the celestial sphere to 5 microarcsecond accuracy. Proposed imaging interferometers as potential follow-on missions to the Hubble Space Telescope include the Laser Stabilized Imaging Interferometer (LASII), and the Dilute Lense Imager (DLI). In addition, the Astronomical Search for Extrasolar Planetary Systems (ASEPS) Program is actively pursuing optical interferometry for extra-solar planet detection. POINTS and the Small OSI for Narrow Angle Astrometry with Two Apertures (SONATA) are leading candidates for ASEPS-1, the first mission in the series.

To pave the way for these and other future missions, a significant infusion of advanced technologies beyond those required for ground operation must be developed. Ground based facilities such as the Mt. Wilson observatory utilize additional mass as a cost effective means to extend system dynamics beyond its components' operational bandwidths. In addition, massive pillars of concrete are available to provide a low vibration foundation on which to mount the optical hardware. In space-based systems, mass and power constraints result in lightweight, flexible systems. Compounding the issue of increased flexibility, space-based systems are subject to a more severe disturbance environment due to on-board power generation, reaction wheels, and station-keeping thrusters. In addition, lightly damped dynamical sub-systems, such as solar arrays and communications antennae, may vibrate for much longer than an observation period. The joint MIT-JPL Stellar Interferometor Technology Experiment (SITE) [2] is a proposed technology demonstration flight experiment on the space shuttle which will unambiguously evaluate the feasibility of space interferometry, demonstrate system integration of the critical component technologies, and quantify each technology's contribution to the overall optical performance metric (viz., the stellar fringe visibility).

Figure 1.1 represents a two aperture space-based interferometer with the associated control topology detailed in Figure 1.2. Light enters the system through two apertures which are spaced sufficiently far apart to obtain the desired angular resolution of the device. The large diameter science light is steered by siderostats through a beam compressor onto the more sensitive dynamic compensation components, namely the optical delay line (ODL) and fast steering mirror (FSM), and tracking sensors. The two beams are finally interfered in centralized combining optics. The quality, or visibility, of the central interference fringe is determined by the difference in intensity between the interference pattern peak and nearest null as given by (1.1).

$$V = \frac{I_{max} - I_{min}}{I_{max} + I_{min}} \tag{1.1}$$

The visibility, V, is reduced by a number of factors including the relative optical pathlength difference (OPD) between the two beams as well as the relative tilt of

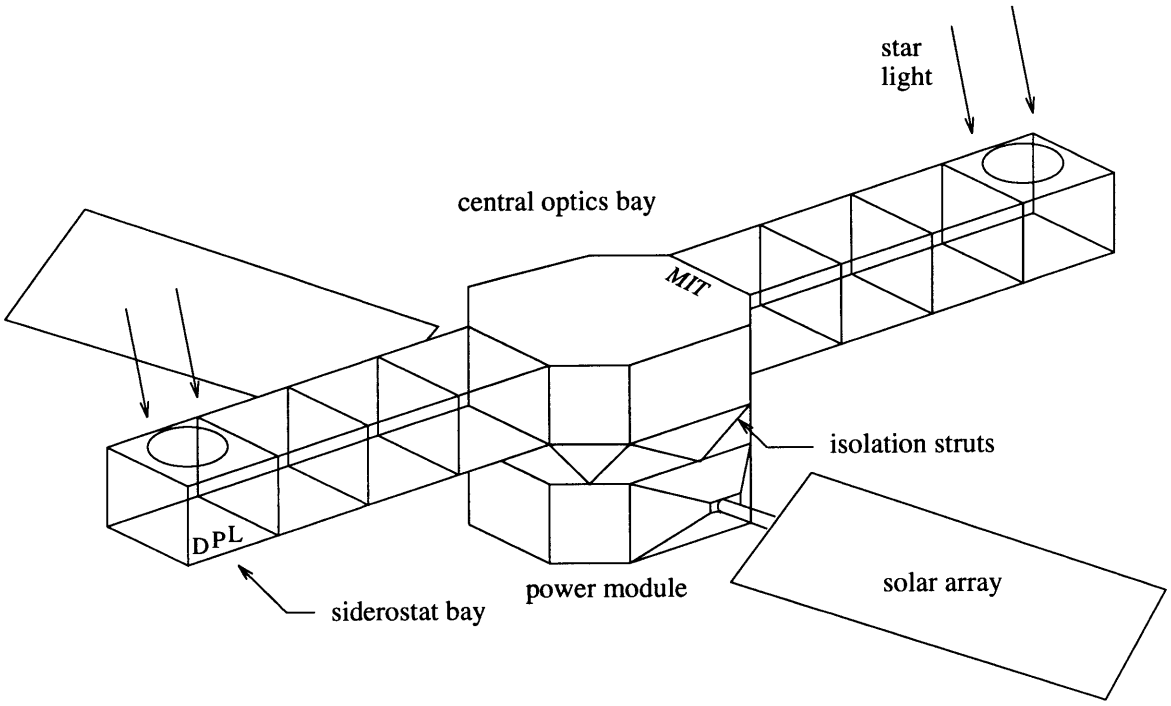

Figure 1.1: Two aperture space-based interferometer

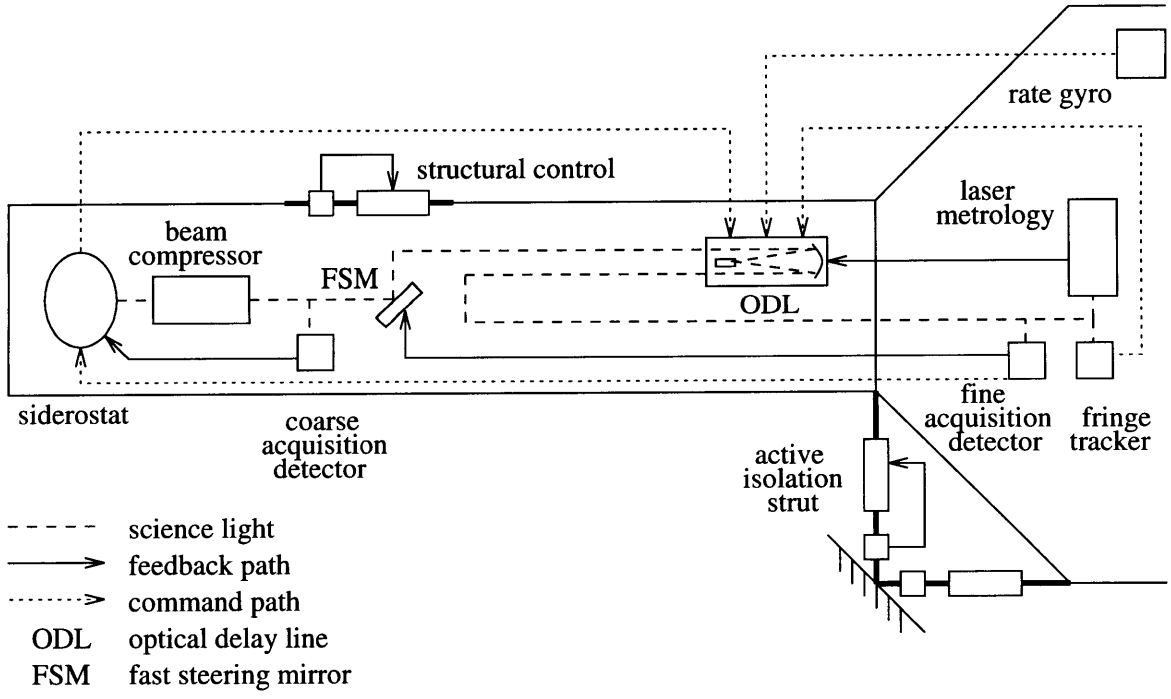

Figure 1.2: Control strategy for a spaceborne interferometer

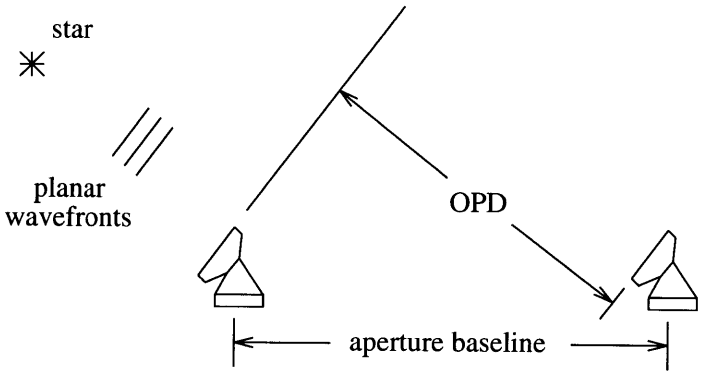

Figure 1.3: OPD due to angular range of target star lines-of-sight

their wavefront planes. The OPD is comprised of an external component due to one collector being closer to the star than the other, as shown in Figure 1.3, and an internal jitter due to structural vibrations shaking the optical elements. The external OPD is dominated by static spacecraft pointing accuracy and low frequency angular drift of the spacecraft between reaction control system (RCS) thruster firings. The internal OPD is a result of structural vibrations caused by on-board power generation, RCS firings and operation of the interferometer's active optical elements.

The internal OPD is measured by a laser metrology system which travels the same internal optical path as the science light, whereas the external quasi-static drift is estimated by a combination of siderostat angular position (star tracker) measurement and accelerometer or rate gyro information. The wavefront tilt in the science light is not directly measured, but is extrapolated from the optical steering system.

The laser metrology and acquisition detector information is fed back to the optical delay lines and fast steering mirrors to attenuate high frequency OPD fluctuations and relative wavefront tilt. The external OPD measurements are utilized in a feed-forward context to estimate the location of the central interference fringe. Once the central fringe is found through open-loop search algorithms, continuous fringe measurements are fed back to all of the active optical elements in order to maintain a fringe lock. In an optical interferometer, the fringe visibility may be measured once such a lock is obtained.

Interference of the incoherent stellar source to obtain useful science information re-

quires precise synchronization of both wavefront tilt and pathlength phasing between two or more light beams. Low and high speed optical devices are utilized to compensate for these angular and pathlength differences to milliarcsecond and nanometer levels, respectively. To accomodate initial target acquisition without repointing the entire spacecraft, these devices must be capable of large angular and translational displacements. In addition, they must be capable of rejecting disturbances due to on-board equipment, including the spacecraft attitude control system. The optical delay line (ODL), shown in Figure 1.4, is an actively controlled optical component which provides the primary disturbance rejection for optical pathlength fluctuations over a large dynamic range. The remainder of this work focuses on the design of a high performance ODL.

Given the multitude of disturbance sources, quasi-static attitude drift, spacecraft flexibility, and fact that the OPD must be controlled to a fraction of a wavelength, optical delay lines incorporated into space-borne interferometers are necessarily high performance devices. Satisfactory performance is typically characterized by nanometer level resolution over meter long travel and a 500 Hz operational bandwidth. In space-based operations, this performance must be met in the presence of optical disturbances which appear from optical element vibrations.

Historically [3] [4] [5] [6], ODL design has consisted of three stages, as shown in Figure 1.4, in order to meet the high dynamic range in stroke and bandwidth. A piezoceramic transducer (PZT) controls the piston type motion of a flat secondary mirror to provide for high resolution and high frequency disturbance rejection, whereas a voice coil which positions the optical cage is responsible for most of the dynamic stroke. A trolley stage permits large quasi-static stroke and initial target acquisition. The predominant control philosophy is to implement sequential loop closure such that the coarse stages desaturate the higher bandwidth stages. Such control designs have been successfully implemented by the Jet Propulsion Laboratory (JPL) [7] [8] and are in current use on the Mt. Wilson Mark III ODL [3] [6].

Further enhancement of ODL performance, as well as understanding high performance output disturbance rejection, necessitates examination of the interactions

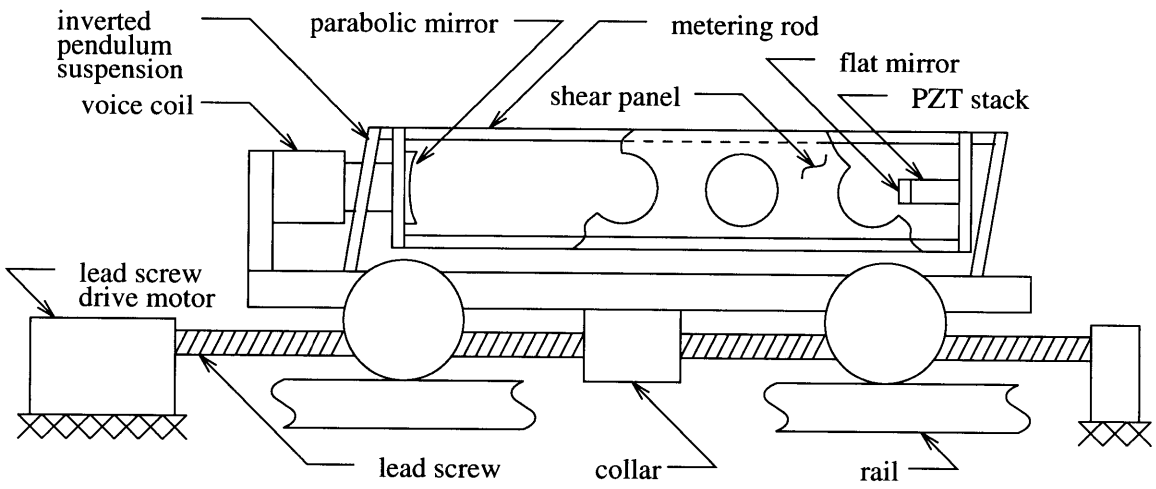

Figure 1.4: Typical optical delay line structure

between the control architecture and physical system. In engineering systems, it is well known that understanding the whole requires understanding the individual parts. It is also well known that optimization of the parts does not necessarily optimize the whole. In this study, optimization of the ODL is performed utilizing both simple and complex models to understand the physics of how a component behaves individually and as a member of a larger system.

As a precursor to such understanding of a high performance ODL, the remainder of this chapter reviews contemporary ODL designs. In addition, the framework in which control-structure design investigations are undertaken is laid out in a manner proposed by Crawley [9]. Finally, the specific objectives of this thesis are outlined in detail.

1.1 Contemporary ODL Developments

Over the past 10 years, optical delay lines have been sucessfully implemented in both laboratory testbeds and ground-based operational facilities. From the design of the Mark III interferometer for ground-based operations on Mt. Wilson to recent developmental research at JPL, careful optical design and classical control techniques have proven sufficient in achieving mission specifications. ODL modal characteristics have

received little attention beyond that necessary for controller design. Such practices, however, are well justified given the lack of power and mass restrictions in laboratory and ground based operations.

The early Mark III interferometer optical delay line [3] [6] is a ground-based device in operation at the Mt. Wilson observatory. To provide for target selection within a 30 degree field of view for the 20 meter baseline between siderostats, 20 meters of total ODL travel are required. To compensate for the Earth's rotation as well as meet sampling interval specifications, the ODL is required to maintain a 0.75 mm/s quasi-steady velocity. A root mean square (RMS) OPD of 15 nanometers is required for fringe acquisition and measurement. The Mark III ODL is similar to the ODL shown in Figure 1.4 except that the trolley is driven by a belt in lieu of a lead screw. The inverted pendulum configuration destiffens the suspension mode, thereby reducing quasi-static voice coil forces during control of the optical cage. In order to perform the specified task, the voice coil and PZT bandwidths are 10 Hz and 120 Hz, respectively. One key improvement for future ODL designs, noted during the qualification testing of the Mark III ODL, is the separation of compensation hardware for the PZT from the remainder of the system. Due to the high stiffness and light mass of the PZT, inertia does not impact PZT dynamic behavior below 1 kHz. Therefore, the PZT behaves as a position type actuator in the frequency range of interest and its controller could be run at a much faster rate thereby increasing the device performance. Overall, the Mark III is very successful in meeting its mission specifications.

The Jet Propulsion Laboratory developed a Phase B optical delay line testbed in response to their Focus Mission Interferometer conceptual studies, which were aimed at identifying the technology required to implement a space-based interferometer. Unlike the Mark III, the JPL Phase B ODL was evaluated on a flexible truss structure as shown in Figure 1.5. The Phase B ODL only consists of the voice coil and PZT stages. Under several different excitation conditions, JPL was able to successfully implement a sequential loop control architecture to obtain 100 to 500 nm pathlength control [7] [8]. Due to significant phase loss and increasing modal density at and

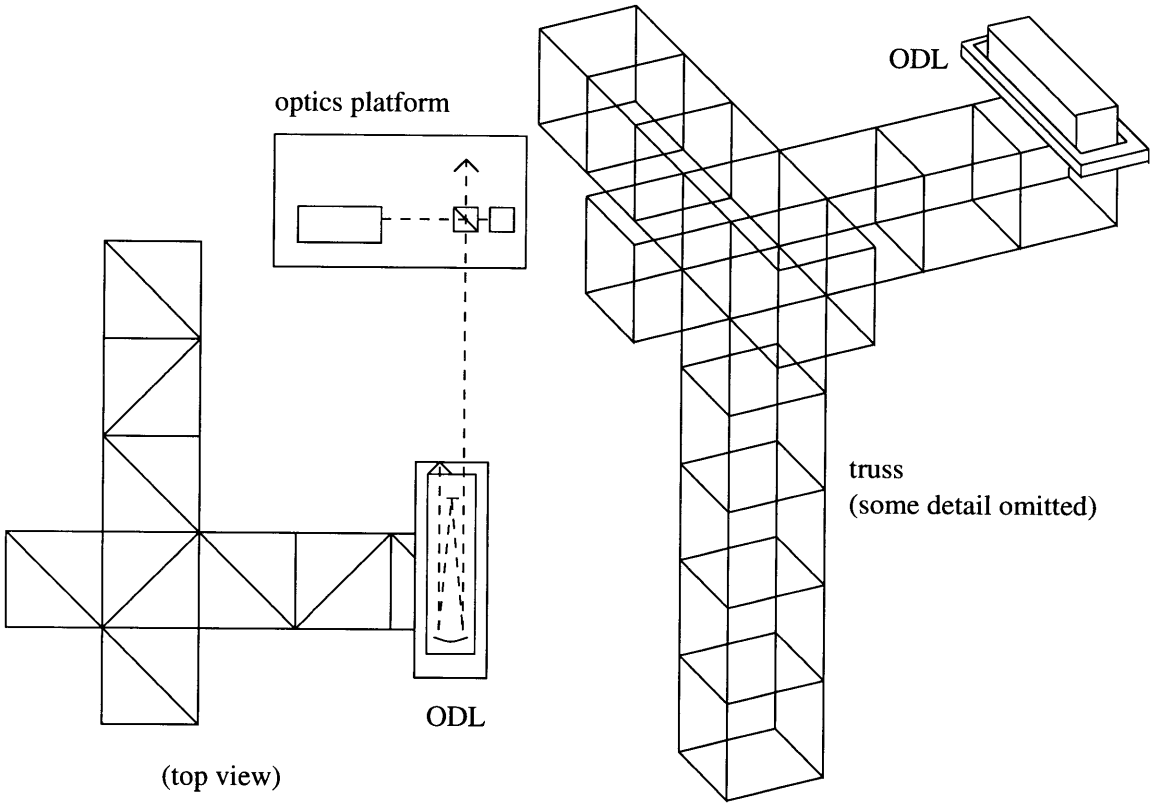

Figure 1.5: JPL Phase B testbed

beyond 86 Hz, the voice coil loop had a crossover frequency near 20 Hz. The PZT loop, however, exibited very little coupling with the other dynamics. Therefore, the PZT loop was crossed over near 350 Hz, thereby providing a net ODL bandwith near 400 Hz. JPL also explored implementation of control algorithms on multiple processors to increase the bandwidth of the PZT loop relative to the voice coil. All of these tests were specifically directed at investigating important features of ODL operation on a flexible platform and not to design the best controllers for such applications.

From their experiences with the Phase B delay line, JPL proceeded to construct a more complete testbed, the Micro-Precision Interferometer (MPI). As a system level testbed, MPI includes both pathlength and wavefront tilt compensation. The MPI design incorporates a belt driven trolley stage with an additional isolation stage between the optical cage suspension and trolley drive mechanism. This additional stage is intended to minimize drive motor disturbances and cable dragging effects on the optical components. Otherwise, the MPI ODL is very similar to the Mark III

design.

In general, the Mark III ODL is the baseline design from which contemporary and future optical delay lines are based. Sequential loop closure has proven effective on both stable concrete foundations and flexible truss structures. The interaction of the voice coil stage with the platform dynamics during JPL Phase B testing forshadows controller limitations and difficulties on a real space-based interferometer. The MIT Middeck Active Control Experiment (MACE) [10], however, has been very successful in implementing several robustly stable compensators to overcome these same difficulties in structural control. The MACE experiments were conducted in the space shuttle middeck experimental facility in order to investigate numerous issues associated with controlling flexible space structures including structural modeling [11], global structural control and control in the presence of structural uncertainty [12]. Therefore, the incorporation of the MACE technology in ODL control design will alleviate the limitations imposed by structural flexibility. Actually demonstrating these robustification techniques on real ODL hardware is expected to pose an additional challenge since 100 dB of optical disturbance rejection by the ODL is required as compared to the 40 dB gains obtained by the MACE experiments.

1.2 Controlled Structures Technology

The maturing field of controlled structures emphasizes an iterative system design process in order to satisfy performance specifications in the presence of a disturbance environment. Since ODLs for space-based interferometers utilize high gain compensators which result in interaction between the ODL and host structure, a controlled structures technology (CST) approach to ODL design is warranted. As shown in Figure 1.6, performance improvement may be achieved through the implementation of input and output isolation, structural redesign, controller design and sensor and actuator selection. The design approach involves propagation of the disturbance sources through the entire system to the final performance metrics. When the system is linearized, these transfer functions are examined in full detail and in dereverberated

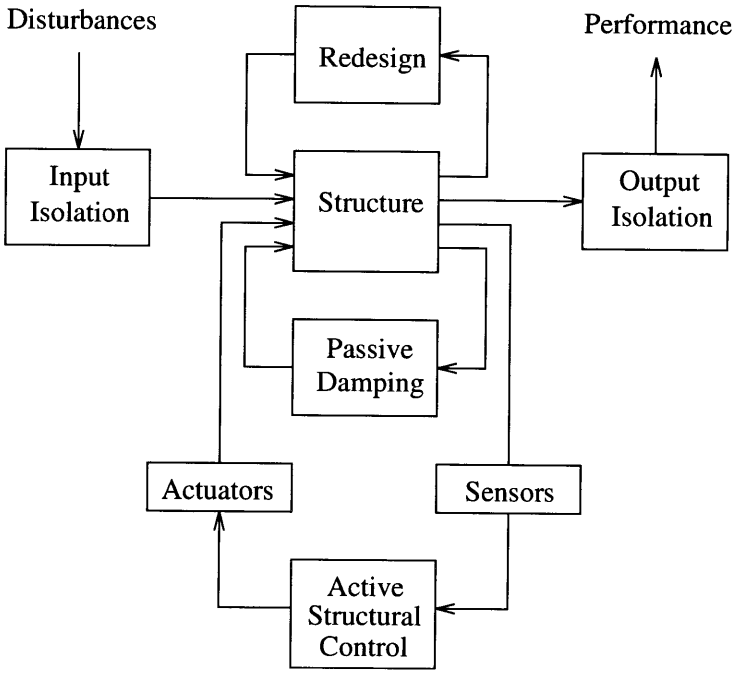

Figure 1.6: Controlled structure design topology

form and are compared to the target performance. These system level comparisons illuminate the degree and location of redesign which must be performed in order to meet the overall performance specifications. This iterative CST *preliminary* design methodology is presented in detail by Crawley [9].

In some instances, satisfactory performance over much of the frequency spectrum may be obtained entirely through input isolation and structural redesign. In the case of stellar interferometers, this is far from true. Without high performance active optical control, stellar interferometer performance is limited to very low magnitude, or bright, stars. Hence, such system level investigations are meaningless without the presence of control. For space based applications, the presence of control is further extended to include structural vibration control which is both low and high authority in nature.

Due to the importance of control on the function of the final system, the standard sequential design philosophy of first building the structure and *then* implementing control is modified to emphasize simultaneous structure and control design. The design process is no longer to just satisfy performance requirements but to do so

with minimal actuation effort. Some would say to utilize all of the actuator, however minimizing actuation effort effectively minimizes actuator mass. Smith, Grigoriadis and Skelton [13] propose a design methodology along this avenue which attempts to minimize control effort by careful redesign of plant characteristics. This end is achieved by starting with an initial plant design and implementing a controller to satisfactorally meet the performance objectives. Once a loop transmission is obtained which satisfies performance, the physical structure is redesigned so as to minimize the actuation effort. This is accomplished by designing the structure to provide the general shape of the loop transmission as opposed to expending control effort to cancel or modify the plant dynamics, such as done by Linear Quadratic Gaussian (LQG) control synthesis. The main drawback in this methodology is that the control cost is directly linked to initial controller design. The strength of this method lies in its simplicity and physical intuition.

In order to allow for gains which may be obtained through controller redesign as well as structural redesign, simultaneous ODL structure and controller design is emphasized. Miller and Jacques [14] present a preliminary design method in which a *typical section* of the structure is used in this parallel stucture-control design approach. The simplicity provides for valuable analytical solutions which illustrate the influence of the plant natural frequency and damping ratio on the control of displacement and rate states when subject to white Gaussian noise disturbances. However, the implications of frequency weighted performance specifications and disturbance characteristics are difficult to infer. Since such knowledge may significantly enhance system performance, the parallel structure-control design philosophy is extended to include such information. Since this additional information increases the problem size to such an extent that analytic solution are no longer feasible, numerical solutions must be invoked. Hence, more accuracte plant dynamics may be utilized in lieu of a typical section without losing insight to the problem. Simplicity in the plant model, however, has the appeal of having fewer parameters to vary in the design process. Therefore, simple modeling of the ODL structure is emphasized in the design process.

Whether classical, LQG, mu-synthesis or other control design techniques are utilized in the initial design process, the optimal plant characteristics are considered invariant by the argument that all good controllers exhibit the same fundamental characteristics given a fixed structure and performance specifications. However, small differences will appear depending upon the control synthesis method chosen. Therefore, the objective of the optimzation procedure is not to design the *best* controller, but rather to design a *good* controller which is *compatible* with the structure and performance specifications. Similarly, detailed optimization of the physical structure is neither efficient nor practical. Therefore rather than searching for *optimal* mass and stiffness distributions, parametric variations on normalized modal and actuator parameters, such as natural frequency and force per unit mass, are preferred so as to obtain a *good* structure which is *compatible* with performance specifications.

1.3 Thesis Objectives

The objective of this thesis is to explore the structural characteristics of optical delay lines and how they relate to output disturbance rejection performance. A combined structure-control design philosophy is emphasized to achieve high performance.

Chapter 2 implements numerical methods to investigate the influence of optical disturbance characteristics on the optimal selection of optical cage suspension frequency and damping ratio. In addition, the impact of the actuation noise floor on suspension optimization is examined in the context of staged actuation. The high dynamic range and high bandwidth nature of staged actuation results in multiple actuators being used to control the same states but with varing degrees of precision and frequency. Posing this problem for LQG controller synthesis in the presence of 64-bit precision computational capabilities is a challenge. Hence, Chapter 2 presents this numerical conditioning issue and a means by which to normalize the ODL staging problem in order to obtain viable LQG controllers. The SITE design requirements are then used as an instructive example in ODL design.

Chapter 3 experimentally explores the structural characteristics of the JPL Phase

B optical delay line in order to further understand performance limiting issues in a real system. In addition, successively higher authority LQG controllers are designed for the Phase B ODL to bolster insight into the controller limitations and trade-offs. Finally, other design issues are qualitatively discussed as a completion to high performance ODL design. Chapter 5 summarizes the thesis results and presents general recommendations for high performance ODL design.

Chapter 2

Structural Design Optimization of a High Performance Optical Delay Line

Much effort has been expended in understanding the optical and control aspects of the optical delay line problem [5] [15] [7] [8]. Justifiably, little attention has been placed on structural flexibility since an operational voice coil bandwidth below 100 Hz has proven sufficient in ground-based operations and the addition of mass is a cost effective means by which to stiffen internal modes to frequencies above these control bandwidths, thereby increasing stability margins. In space systems, utilizing mass to increase modal frequencies is no longer a cost effective solution. In addition, the problem is further complicated by spacecraft flexiblity within the ODL bandwidth, unlike ground-based systems which utilize massive concrete pillars to stabilize the system. Since space-based operation allows diffraction-limited observations, the need for higher performance increases thereby motivating the use of lightweight, higher bandwidth optical delay lines. Spacecraft power limitations also stress efficiency in the design. This requires that ODLs be designed from a combined structure-control perspective to understand the impacts of control-structural design details, other than stiffness and mass, which will help to alleviate performance limitations due to flexibility.

This chapter explores optimal selection of fundamental device characteristics. Studies include the impact of optical disturbance characteristics, actuation noise floor and optical cage suspension frequency on the cost to achieve the required OPD. In addition, the high dynamic range of the optical delay line resulting from staged actuation poses a unique problem for Linear Quadratic Gaussian (LQG) controller synthesis and requires special conditioning to obtain viable compensators. Hence, a means to circumvent the difficulties in posing the staged ODL problem for LQG controller synthesis is presented. Finally, the joint MIT-JPL SITE ODL performance requirements [2] are utilized as an illustrative design example. All investigations are made with the underlying assumptions of linearity and time invariance.

2.1 Optical Delay Line Problem Statement

The primary function of the optical delay line is to control the optical pathlength difference (OPD) between at least two optical paths such that the same wavefront of science light may be interfered. Table 2.1 indicates that ODL characteristics neccesary to perform this task vary according to mission, except that the ratio of piezoceramic transducer (PZT) bandwidth to voice coil (VC) bandwidth is approximately 10 and that a root mean square (RMS) OPD of approximately 10 nm is needed, due to the wavelength of visible light. The fundamental ODL design requirements are listed below:

(1) Control root mean square (RMS) OPD between two light paths so that the science light of the same wavefront may be interfered (required OPD $\sim$ 10 nm RMS for $\lambda/50$ accuracy of 500 nm wavelength science light)

(2) Static ODL travel must accomodate desired field of view (FOV)

(3) Dynamic OPD control to compensate for spacecraft vibrations ($\sim$ 3 mm RMS)

Table 2.1: Various interferometer optical delay line characteristics

Program	Platform	Baseline	FOV	RMS	Optical Delay Line				Ref
				OPD	Travel	Rate	BW [Hz]		
		[m]	[deg]	[nm]	[m]	[mm/s]	VC	PZT	
Mark III	ground	20	30	15	20	0.75	10	120	[3]
BOA	ground	400		10	5	15	75	900	[5]
OSI	space	7	30	0.34	2	5	80	500	[1]
SITE	space	4	0.5	25	< 1	< 1	100	600	[2]

[1] OSI is still in the design phase. These values were provided courtesy of JPL.

(4) Quasi-static OPD control to compensate for rotation of the Earth or attitude drift of the spacecraft (quasi-steady velocity)

(5) $\lambda/20$ or better wavefront distortion (focus specification)

To accomplish these high bandwidth and high dynamic range objectives, the ODL is typically composed of three layers of control as shown previously in Figure 1.4. Depending upon the total slewing requirement, a lead screw, as shown in Figure 1.4, or a belt driven cart may be used for the quasi-static positioning. The low frequency dynamic corrections are implemented using an electro-magnetic voice coil actuator to position an optical cage, whereas the high precision and high bandwidth control is performed using a PZT. Depending upon the optical geometry of the ODL cat's eye retroflector, a maximum PZT stroke on the order of 10 μm is permissible before the device is defocused. Given that many parameters are somewhat fixed, such as the science light diameter, the main free design parameters are the optical cage suspension frequency and distribution of control effort among the actuators. Other more subtle structurally related design parameters include actuator dynamic range, sensor signal-to-noise ratios, isolation, reactuation and thermal compensation.

The performance objective of the ODL is simple – provide pathlength OPD control to within a specified RMS magnitude for a given optical disturbance. However, several indirect design requirements, those that are imposed by system design rather than

mission specifications, may appear which subtly impact the ODL design such as actuator and sensor alignment and clearances. From a modal design and control viewpoint, satisfaction of the RMS OPD is sufficient.

In order to evaluate the quality of a high performance ODL, one must know the associated controller characteristics since performance is limited by both control and structural design. For each structural design iteration, a compatible controller must be synthesized to fully evaluate the incremental performance and cost. Since iterative design is expensive, finding the *best* structure is neither practical nor cost effective. Hence, the structural design objective is to design a *good* structure knowing that control will be utilized to satisfy the overall performance requirements. Similarly, synthesizing the *best* controller for each structural permeatation is not practical. Hence, only compatible control designs are necessary for the system optimization.

Numerous control sysnthesis tools are available, including classical pole and zero placement, eigenstructure assignment, linear quadratic cost optimization and mu-synthesis [16]. The following analysis concentrates on linear systems and, hence, will only utilize linear control. Classical control techniques, including sequential loop closure, are impractical in an iterative design procedure since a *good* design heavily relies upon intuition and physical understanding. A Linear Quadratic Regulator (LQR) approach is attractive since it enforces a certain amount of optimization and imposes certain stability guarantees, however, it has one critical drawback. Since disturbance dynamics cannot be directly included as such in LQR, iterative frequency weighting is required to converge to a good controller. LQR mathematics explicity target the issue of how to most effectively apply actuation effort given plant dynamics, not how to reject a disturbance. Hence LQR is no better suited than classical control for this iterative problem.

The next logical choice is Linear Quadratic Gaussian (LQG). LQG permits direct inclusion of disturbance dynamics in the filtering process in addition to some of the benefits of LQR, except stability margin guarantees no longer exist. Also, LQG tends not to be very robust for uncertain structural systems since it attempts to cancel the lightly damped plant dynamics. However, this can be alleviated through desensiti-

zation techniques such as sensitivity weighting [12] [17]. Due to a vast database of understanding the Kalman filtering and LQR problems, synthesizing consistent controllers and enforcing a fundamental amount of optimization, LQG is an ideal choice for an automated control generation technique in an iterative design process. For the ODL problem, the RMS OPD performance specification warrants H_2 cost functionals. Hence, LQG is compatible with the ODL design problem and will be used for controller synthesis.

2.2 Sizing Fundamental Device Characteristics

Simple models rarely capture the behavioral fidelity required for control of real structures, however they provide invaluable insight into fundamental issues and performance tradeoffs. Jacques [18] utilizes a typical section approach to generalize fundamental high performance versus structure characteristics when subject to white noise disturbances. Such simplifications permit attractive analytical investigations. However, the implications of frequency weighted performance specifications or disturbance characteristics are difficult to infer. Since such knowledge may significantly enhance system performance yet greatly compounds the problem size, analytic solutions are no longer feasible and numerical methods must be invoked. Since the size of the system to be *optimized* is the combination of the mathematics which describe the physical structure, disturbance environment and performance specifications, even a simple two state spring-mass-dashpot model can become analytically unwieldly. Yet a two state system contains much fewer physical parameters which may be varied relative to the corresponding control design model and, hence, remains valuable in selecting primary design features such as fundamental modal characteristics. This section models the optical cage as a simple spring-mass-dashpot system to explore the implications of physical parameter selection on performance when subjected to narrowband and broadband output disturbance spectrums.

The optical cage suspension model used in this section is shown in Figure 2.1. The mass-normalized dynamics are given by equation (2.1). The sensor measures the

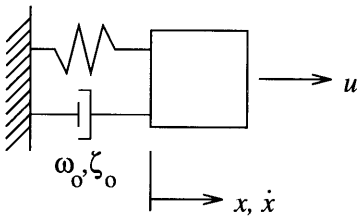

Figure 2.1: Simple spring-mass-dashpot model

position, x, of the optical cage and the optical disturbance , d_o, in the presence of sensor noise, n_s, as shown in equation (2.2). Due to the nature of the device, an optical cage displacement of x produces an optical pathlength change of $2x$.

$$\ddot{x} + 2\zeta_o\omega_o\,\dot{x} + \omega_o^2\,x = u \tag{2.1}$$

$$y = 2x + d_o + n_s \tag{2.2}$$

As disturbance spectra may widely vary, investigation of their impact is divided into two categories. First, well determined spikes typical of rotating systems such as pumps and reaction wheels or lightly damped structures such as solar arrays and antennaes are investigated. Second, less deterministic background disturbances are examined using a broadband spectrum.

Study of the impact of spikes which may be present in a disturbance spectrum, such as those due to host structure vibrations, is simplified to the disturbance autospectrum in Figure 2.2 with simple second order dynamics, given by equation (2.3) where w_o is white Gaussian noise of intensity Ξ_o and ω_d, ζ_d determine the frequency and magnitude of the disturbance spike, respectively, and α is a scaling parameter.

$$\begin{bmatrix} \dot{\phi} \\ \ddot{\phi} \end{bmatrix} = \begin{bmatrix} 0 & 1 \\ -\omega_d^2 & -2\zeta_d\omega_d \end{bmatrix} \begin{bmatrix} \phi \\ \dot{\phi} \end{bmatrix} + \begin{bmatrix} 0 \\ \sqrt{\Xi_o} \end{bmatrix} w_o \tag{2.3}$$

$$d_o = \alpha\omega_d^2 \begin{bmatrix} 0 & 1 \end{bmatrix} \begin{bmatrix} \phi \\ \dot{\phi} \end{bmatrix}$$

Figure 2.3 shows the system topology. The reference position, r, corresponds to command signals which compensate for steady spacecraft drift or rotation of the

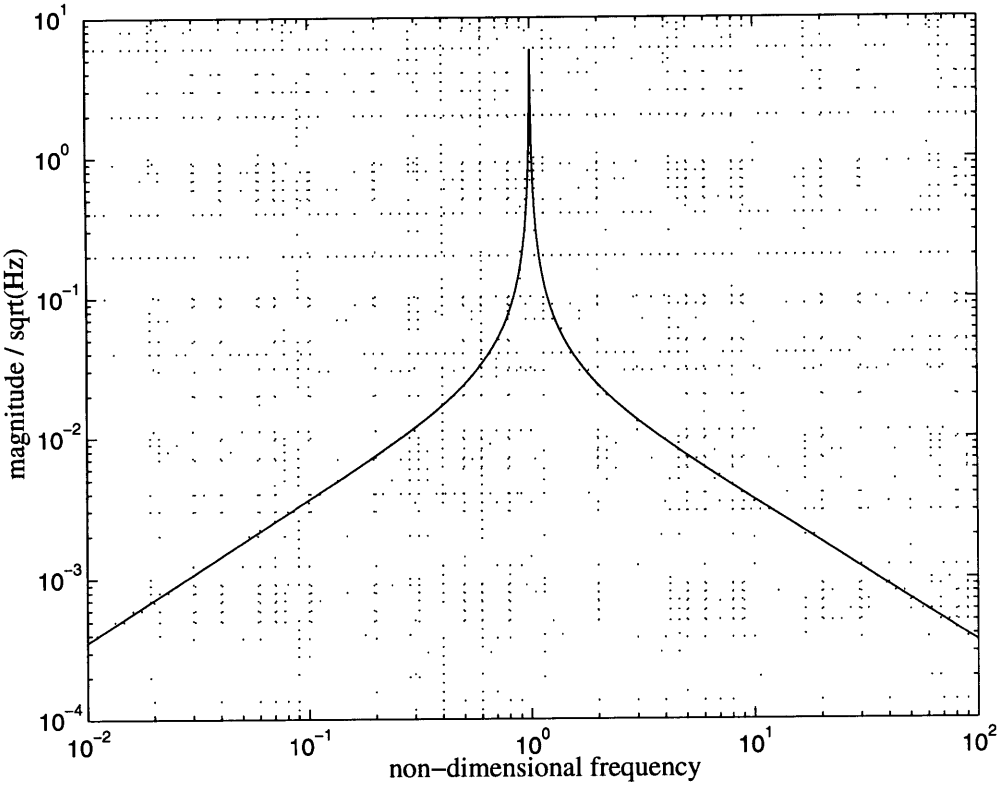

Figure 2.2: Narrowband disturbance autospectrum

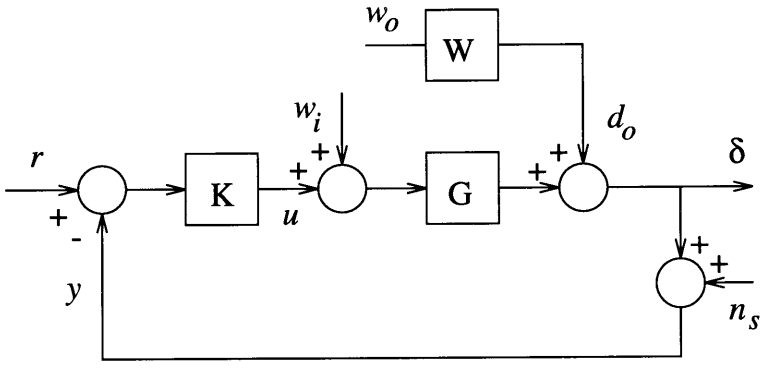

Figure 2.3: Optical cage control topology

Earth. This reference command is required since such motions are unobservable by the laser metrology system. A white Gaussian disturbance at the plant input,w_i, has been included in the figure, but will be ignored at present. The optical disturbance, d_o, is shaped by the filter, W, and driven by white Gaussian noise, w_o. The combined plant and disturbance dynamics, omitting w_i and setting $r = 0$, are given by equation (2.4). The performance is defined as the control effort, μ, and the OPD, δ, as given by equation (2.5). A control weighting parameter, ρ, has been included as a parameter which may be varied during the controller synthesis in order to meet the required RMS OPD, Δ_{rms}. Similarly, sensor equation (2.6) has been modified to permit variation of the sensor noise intensity, θ. Variation of the control and sensor parameters, ρ and θ, permit proper sizing of the actuator and sensor during the system optimization process.

$$\begin{bmatrix} \dot{x} \\ \ddot{x} \\ \dot{\phi} \\ \ddot{\phi} \end{bmatrix} = \begin{bmatrix} 0 & 1 & 0 & 0 \\ -\omega_o^2 & -2\zeta_o\omega_o & 0 & 0 \\ 0 & 0 & 0 & 1 \\ 0 & 0 & -\omega_d^2 & -2\zeta_d\omega_d \end{bmatrix} \begin{bmatrix} x \\ \dot{x} \\ \phi \\ \dot{\phi} \end{bmatrix} + \begin{bmatrix} 0 & 0 \\ 0 & 0 \\ 0 & 0 \\ \sqrt{\Xi_o} & 0 \end{bmatrix} \begin{bmatrix} w_o \\ n_s \end{bmatrix} + \begin{bmatrix} 0 \\ 1 \\ 0 \\ 0 \end{bmatrix} u \tag{2.4}$$

$$\begin{bmatrix} \delta \\ \mu \end{bmatrix} = \begin{bmatrix} 2 & 0 & \alpha\omega_d^2 & 0 \\ 0 & 0 & 0 & 0 \end{bmatrix} \begin{bmatrix} x \\ \dot{x} \\ \phi \\ \dot{\phi} \end{bmatrix} + \begin{bmatrix} 0 & 0 \\ 0 & 0 \end{bmatrix} \begin{bmatrix} w_o \\ n_s \end{bmatrix} + \begin{bmatrix} 0 \\ \sqrt{\rho} \end{bmatrix} u \tag{2.5}$$

$$y = \begin{bmatrix} 2 & 0 & \alpha\omega_d^2 & 0 \end{bmatrix} \begin{bmatrix} x \\ \dot{x} \\ \phi \\ \dot{\phi} \end{bmatrix} + \begin{bmatrix} 0 & \sqrt{\theta} \end{bmatrix} \begin{bmatrix} w_o \\ n_s \end{bmatrix} + \begin{bmatrix} 0 \end{bmatrix} u \tag{2.6}$$

Equation (2.7) compacts the notation to a more intelligible form where the state, disturbance and performance vectors have been contracted as shown in equations (2.8) through (2.10).

$$\begin{bmatrix} \dot{\xi} \\ z \\ y \end{bmatrix} = \begin{bmatrix} A & B_w & B_u \\ C_z & D_{zw} & D_{zu} \\ C_y & D_{yw} & D_{yu} \end{bmatrix} \begin{bmatrix} \xi \\ w \\ u \end{bmatrix} \tag{2.7}$$

$$\xi^T = [\ x \quad \dot{x} \quad \phi \quad \dot{\phi}\ ] \tag{2.8}$$

$$w^T = [\ w_o \quad n_s\ ] \tag{2.9}$$

$$z^T = [\ \delta \quad \mu\ ] \tag{2.10}$$

The corresponding LQG compensator transfer function matrix is given by equation (2.11) where G_{LQ} and H_{KF} are the constant gain matrices obtained by solving the associated linear time invariant Riccati equations (2.12) and (2.13). Since w does not directly excite the plant dynamics, the Kalman filter gain, H_{KF}, associated with the plant states is identically zero. Conversely, u only influences the plant dynamics, hence the regulator gain, G_{LQ}, is identically zero for the disturbance dynamics states.

$$K(s) = G_{LQ}\left[sI - A + B_u G_{LQ} + H_{KF} C_y\right]^{-1} H_{KF} \tag{2.11}$$

$$0 = A^T K + KA + C_z^T C_z - K B_u D_{zu}^T D_{zu} B_u^T K \tag{2.12}$$

$$0 = A\Sigma + \Sigma A^T + B_w B_w^T - \Sigma C_y^T D_{yw} D_{yw}^T C_y \Sigma \tag{2.13}$$

Rewriting equation (2.11) to explicitly separate the non-zero gains and illuminate the role of the plant dynamics $[A_p, B_p, C_p]$, equation (2.1), and disturbance dynamics $[A_d, B_d, C_d]$, equation (2.3), gives

$$K(s) = \begin{bmatrix} G_{LQ} & 0 \end{bmatrix} \begin{bmatrix} sI - A_p + B_p G_{LQ} & 0 \\ H_{KF} C_p & sI - A_d + H_{KF} C_d \end{bmatrix}^{-1} \begin{bmatrix} 0 \\ H_{KF} \end{bmatrix} \tag{2.14}$$

From equation (2.14), the role of the optical disturbance dynamics in shaping the closed-loop poles is quite clear since the poles of the compensator are given by equation (2.15). All of the compensator poles are given by the two independent Riccati equations on the plant dynamics and disturbance dynamics. If the optical disturbance was considered white Gaussian noise, the resulting Kalman filter gain would

have been exactly zero. In such a case, the disturbance at the plant input, w_i, would have to be included as the process noise in the LQG controller synthesis.

$$det(sI - A_p + B_p G_{LQ}) det(sI - A_d + H_{KF} C_d) = 0 \tag{2.15}$$

The LQR cost is chosen equivalent to the performance metric, δ, and the control effort, μ. The compensator synthesis parameters ρ and θ are decreased until the absolute closed-loop performance requirement, Δ_{rms}, is achieved. The actual closed-loop performance, δ_{rms}, and control cost, u_{rms}, are evaluated by the solution of the Lyapunov equation, (2.16), where C_δ and C_u extract the performance and control states from the closed-loop dynamics $[A_{CL}, B_{CL}]$ given by equation (2.19). Note that equations (2.17) and (2.18) for δ_{rms} and u_{rms}, respectively, are only valid for single-input single-output (SISO) models. In the multi-input multi-output (MIMO) case, the expected values should be computed.

$$0 = A_{CL}\Sigma_x + \Sigma_x A_{CL}^T - B_{CL} W B_{CL}^T \tag{2.16}$$

$$\delta_{rms} = \sqrt{C_\delta \Sigma_x C_\delta^T} \tag{2.17}$$

$$u_{rms} = \sqrt{C_u \Sigma_x C_u^T} \tag{2.18}$$

$$\dot{\xi} = (A - B_u K C_y)\xi + (B_w - BuK D_{yw})w \tag{2.19}$$

$$z = (Cz - D_{zu} K C_y)\xi - (D_{zu} K D_{yw})w \tag{2.20}$$

Since LQG attempts to invert the disturbance dynamics, the compensator will contain zeros with similar charateristics as the disturbance poles. In other words, the high sharp peaks will become deep and narrow valleys in K(s). Hence, if the location, or frequency, of the disturbance peak is slightly different from the real disturbance or the real disturbance frequency is prone to shifting, the notch will be ineffective. To improve the performance robustness in consideration of this frequency uncertainty, the filter disturbance dynamics $[A_\phi, B_\phi, C_\phi]$ contain more damping, ζ_d, than

the true narrowband disturbance. However, the true disturbance dynamics are utilized for closed-loop evaluation. For more information on methods of desensitization techniques, the reader is referred to the investigations of robustification techniques performed in connection with the MIT MACE program [12].

With the plant and disturbance models in place, the remaining task is to find the physical parameters, ω_o and ζ_o, which satisfy the performance requirement, $\delta_{rms} \leq \Delta_{rms}$, for the lowest cost, u_{rms}. As opposed to deriving the non-linear optimization problem through Lagrange multipliers and posing a numerical gradient search or other such algorithm, the solution space is simply mapped over a range of permissible parameters ω_o and ζ_o. For each ω_o and ζ_o, the independent LQG parameters ρ and θ are incremented upon until the performance requirement is met. The associated cost is then defined by u_{rms}.

Such cost mapping is shown in Figure 2.4 for a unit RMS disturbance with $\omega_d = 1.0$ Hz and $\zeta_d = 0.002$ for performance requirements of $\Delta_{rms} = 0.5$, 0.1 and 0.01. The main characterstic to note is the prominent valley in control cost for the 50% and 90% disturbance rejection cases. The absence of that valley in the 99% rejection case indicates that structural tailoring is only beneficial for low authority disturbance rejection. Under such circumstances, the discovery that the optimal optical cage suspension frequency coincides with the disturbance frequency is well understood for output type disturbances. Effectively, the best thing to do is to maximize control authority over the disturbance bandwidth. Another feature is that the influence of the suspension mode damping ratio is negligible for $\zeta_o < 0.05$. This indicates that the damping ratio should be chosen from a stability robustness perspective. Since LQG attempts to invert the plant dynamics, lightly damped modes pose stability problems. Conversely, heavily damped modes are stable, but require more effort to control.

Since the ODL problem results in high authority compensation, significant gains in control cost due to structural flexibility vanish. Figure 2.4(d:99% curve) indicates that all suspension frequencies below approximately 5 Hz result in the same optimal cost, u_{rms}. Other issues may or may not narrow the range of *good* suspension frequencies. For example, consider a two stage device which must reject an output

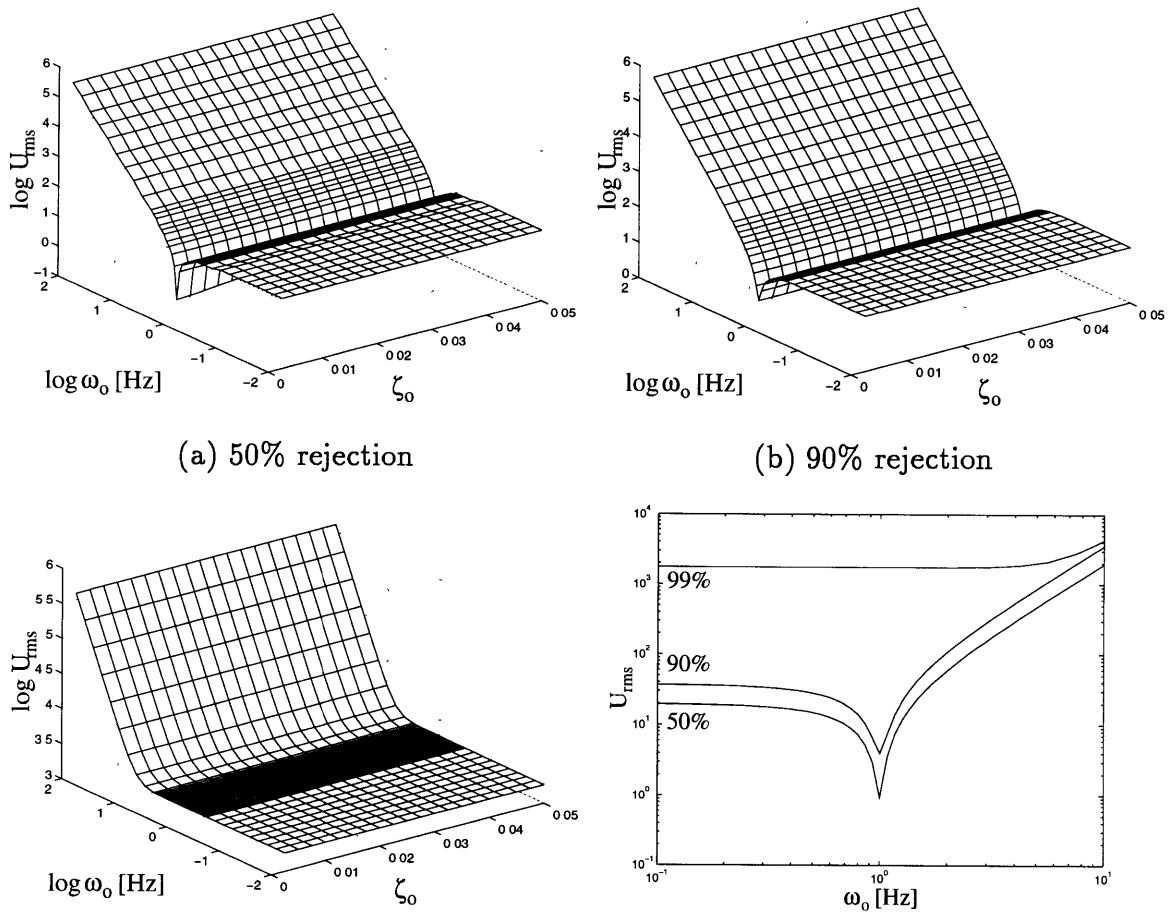

(a) 50% rejection

(b) 90% rejection

(c) 99% rejection

(d) composite trace at $\zeta_o = 0.02$

Figure 2.4: Optimal narrowband disturbance rejection

disturbance while tracking a position command input. A very soft suspension between the two stages would require additional control effort since the fine positioning stage must track the coarse stage. As the suspension stiffness increases, the cost to reject the output disturbance also increases. Hence, the optimal stiffness may arise from interaction with other stages thus requiring models with more detail. In the case of narrowband output disturbance rejection, the simple model only establishes an upper bound for the suspension frequency.

Similar to the narrowband disturbance, the broadband disturbance is assumed to contain finite energy as shown in Figure 2.5. This could be representative of noise generated by a device with an independent servo control. The mathematics is nearly identical to that of the narrowband disturbance rejection problem and, therefore, will

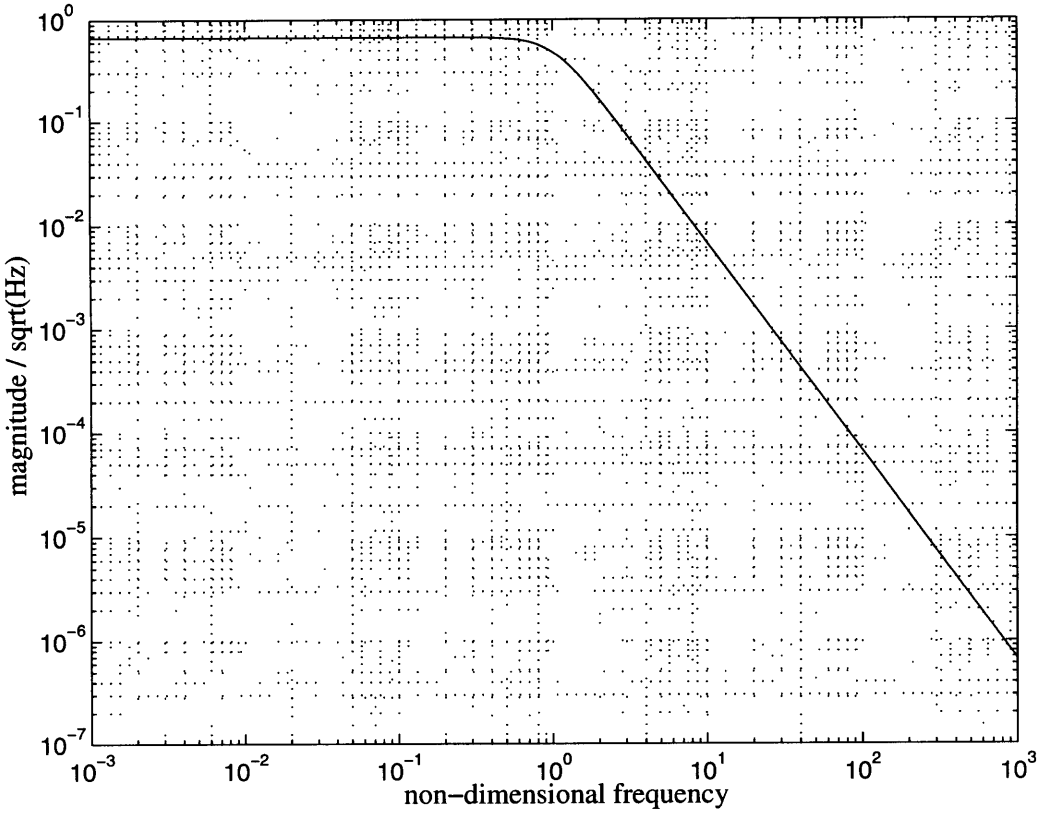

Figure 2.5: Broadband disturbance autospectrum

not be repeated. Figure 2.6 presents the cost to reject 50%, 90% and 99% of a unit RMS disturbance with $\omega_d = 1$ Hz and $\zeta_d = 0.707$. In contrast to the narrowband disturbance case, only a slight decrease in control cost is gained through selection of ω_o. This is due to the disturbance energy being spread out over a broad frequency range as compared to the plant flexibility which only provides a local increase in control authority. Similar to high authority narrowband disturbance rejection, the simple model only provides an upperbound on good suspension frequencies. In both cases, the upper bound on ω_o is a function of disturbance shape as well as the desired level of performance.

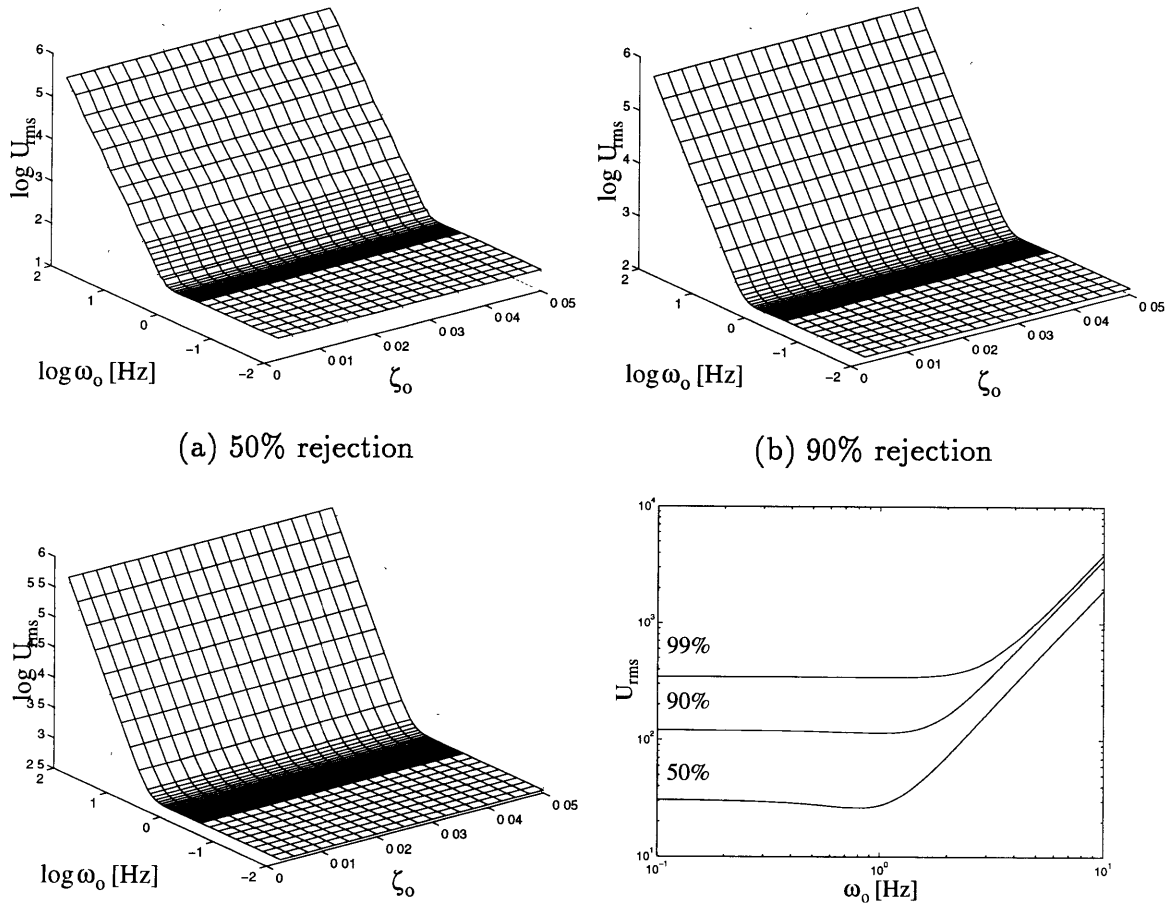

(a) 50% rejection

(b) 90% rejection

(c) 99% rejection

(d) composite trace at $\zeta_o = 0.02$

Figure 2.6: Optimal broadband disturbance rejection

2.3 Actuator Noise Limitations and the Staging Problem

An important consideration of real systems, as well as a prime motivator for actuator staging, is the presence of additive noise in the actuation signal. These noises as well as general physical disturbances on the plant result in perturbations of the performance metric. One of the more obvious noise sources is resolution of the control hardware digital-to-analog converters (D/A), usually 12 bit resolution, which generate the actuator signals. Another source is the fundamental noise inherent with the quality of electronics, typically 4mV per 10V. As control gain is increased to attain

higher authority, the magnitude of both actuation signal and noise is increased. Unlike an exogenous physical disturbance on the plant, the magnitude of the actuation noise, hereafter referred to as the actuator *noise floor*, is linked to the maximum actuator effort. Hence, incresing actuator size to reject the noise floor is ineffective and alternate methods must be utilized. One solution is to increase the resolution of the controller hardware D/A, thereby reducing the noise floor. Another method, which is required when a significant reduction in the noise floor is needed, is to stage actuators of different precisions and bandwiths. Returning to the optical delay line problem, the objective is to identify where each stage becomes ineffective so that the next higher precision stage may take over the compensation effort. In addition, it is desirable to identify how selection of the optical cage suspension characteristics, ω_o and ζ_o, is influenced by the actuator noise floor.

Again, consider the optical cage suspension model used in the previous section to investigate optical disturbance rejection. The actuator noise floor, w_i detailed in Figures 2.1 and 2.3, is added to equations (2.4) through (2.6). The optical disturbance, w_o, is retained to address the issue of optical disturbance rejection in the presence of the noise floor. The actuator noise floor is considered to be white Gaussian noise with an intensity, Ξ_i, which is related to the maximum actuator effort, $|max[u]|$, signal-to-noise ratio in the actuation electronics,N_u, and a scaling parameter, σ, as shown in equation (2.21). The resulting dynamics are shown in equations (2.22) through (2.24). The compacted form in equation (2.7) is unchanged.

$$\Xi_i = \left(\frac{\sigma}{N_u}|max[u]|\right)^2 \tag{2.21}$$

$$\begin{bmatrix} \dot{x} \\ \ddot{x} \\ \dot{\phi} \\ \ddot{\phi} \end{bmatrix} = \begin{bmatrix} 0 & 1 & 0 & 0 \\ -\omega_o^2 & -2\zeta_o\omega_o & 0 & 0 \\ 0 & 0 & 0 & 1 \\ 0 & 0 & -\omega_d^2 & -2\zeta_d\omega_d \end{bmatrix} \begin{bmatrix} x \\ \dot{x} \\ \phi \\ \dot{\phi} \end{bmatrix} + \begin{bmatrix} 0 & 0 & 0 \\ \sqrt{\Xi_i} & 0 & 0 \\ 0 & 0 & 0 \\ 0 & \sqrt{\Xi_o} & 0 \end{bmatrix} \begin{bmatrix} w_i \\ w_o \\ n_s \end{bmatrix} + \begin{bmatrix} 0 \\ 1 \\ 0 \\ 0 \end{bmatrix} u \tag{2.22}$$

$$\begin{bmatrix} \delta \\ \mu \end{bmatrix} = \begin{bmatrix} 2 & 0 & \alpha\omega_d^2 & 0 \\ 0 & 0 & 0 & 0 \end{bmatrix} \begin{bmatrix} x \\ \dot{x} \\ \phi \\ \dot{\phi} \end{bmatrix} + \begin{bmatrix} 0 & 0 & 0 \\ 0 & 0 & 0 \end{bmatrix} \begin{bmatrix} w_i \\ w_o \\ n_s \end{bmatrix} + \begin{bmatrix} 0 \\ \sqrt{\rho} \end{bmatrix} u \tag{2.23}$$

$$y = \begin{bmatrix} 2 & 0 & \alpha\omega_d^2 & 0 \end{bmatrix} \begin{bmatrix} x \\ \dot{x} \\ \phi \\ \dot{\phi} \end{bmatrix} + \begin{bmatrix} 0 & 0 & \sqrt{\theta} \end{bmatrix} \begin{bmatrix} w_i \\ w_o \\ n_s \end{bmatrix} + \begin{bmatrix} 0 \end{bmatrix} u \tag{2.24}$$

Since the noise floor excites the plant states, the resulting Kalman filter gain will be non-zero for system states. The regulator gain, however, will still be exactly zero for the optical disturbance states as in optical disturbance rejection. Hence, the disturbance dynamics do influence the performance, yet the separation obtained in equation (2.15) for optical disturbance rejection is no longer valid. However, the noise floor intensity, Ξ_u, is unknown since the required actuation effort is undetermined. In lieu of using equations (2.22) through (2.24), the optical disturbance rejection equations (2.4) through (2.6) will be used with the noise floor being introduced during closed-loop evaluation.

In order to further examine the influence of the noise floor on selecting the optimum optical cage suspension frequency, consider an example problem of a single spring-mass-dashpot which is to reject an optical disturbance in the presence of an actuation noise floor. The performance specification is $\Delta_{rms} = 0.1$ mm in the presence of a broadband optical disturbance with 10 mm RMS magnitude, $\omega_d = 6$ Hz and $\zeta_d = 0.707$.

The Riccati equations to be solved and the resulting compensator are exactly as before in equations (2.11) through (2.13). Introducing a performance margin $\sigma = 3$ and assuming that the noise floor is $\pm 1/2$ of the least significant bit of the hardware D/A, the noise floor is known given the resolution of the D/A.

For the example problem, the resulting closed-loop performance and actuation are shown in Figures 2.7 and 2.8 for 8, 12 and 16-bit D/A hardware, respectively. Figure 2.7 shows the performance, .1 mm RMS, without the noise floor in addition to the

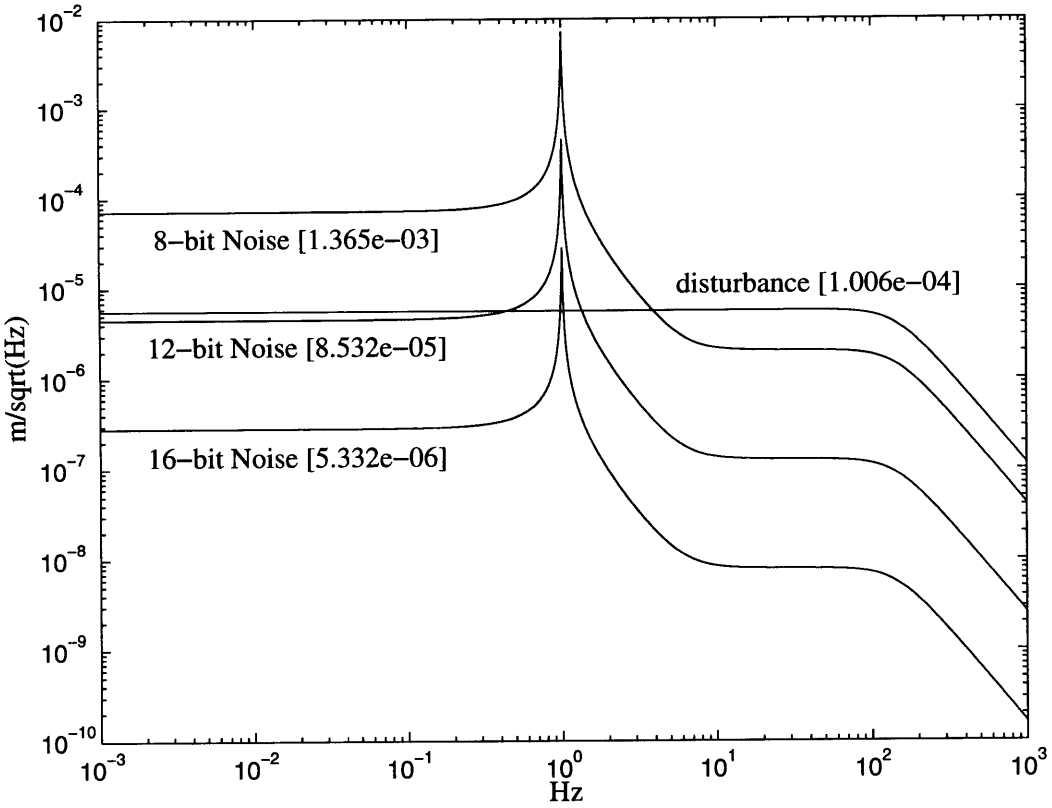

Figure 2.7: Performance perturbation due to actuation noise floor
(RMS values in brackets)

incremental performance perturbations of 1.37, .0853 and .00533 mm RMS resulting from the actuation noise floors of 8, 12 and 16 bits, respectively. In the absence of the noise floor, the performance requirement is met. The noise floor for the 8-bit D/A, however, results in a performance perturbation which is an order of magnitude greater than the required performance. Therefore, performance cannot be satisfied using 8-bit D/A hardware. With more work, 12-bit hardware may be acceptable whereas 16-bit hardware produces an insignificant performance degredation.

Figure 2.8 shows the corresponding control effort and incremental control effort to reject the disturbance and noise floors. Satisfaction of the performance requirement without any noise floor requires 119 actuation units, AU. As seen in Figure 2.8, an 8-bit D/A results in an additional 42.9 AU RMS, whereas a 16-bit D/A adds only 0.168

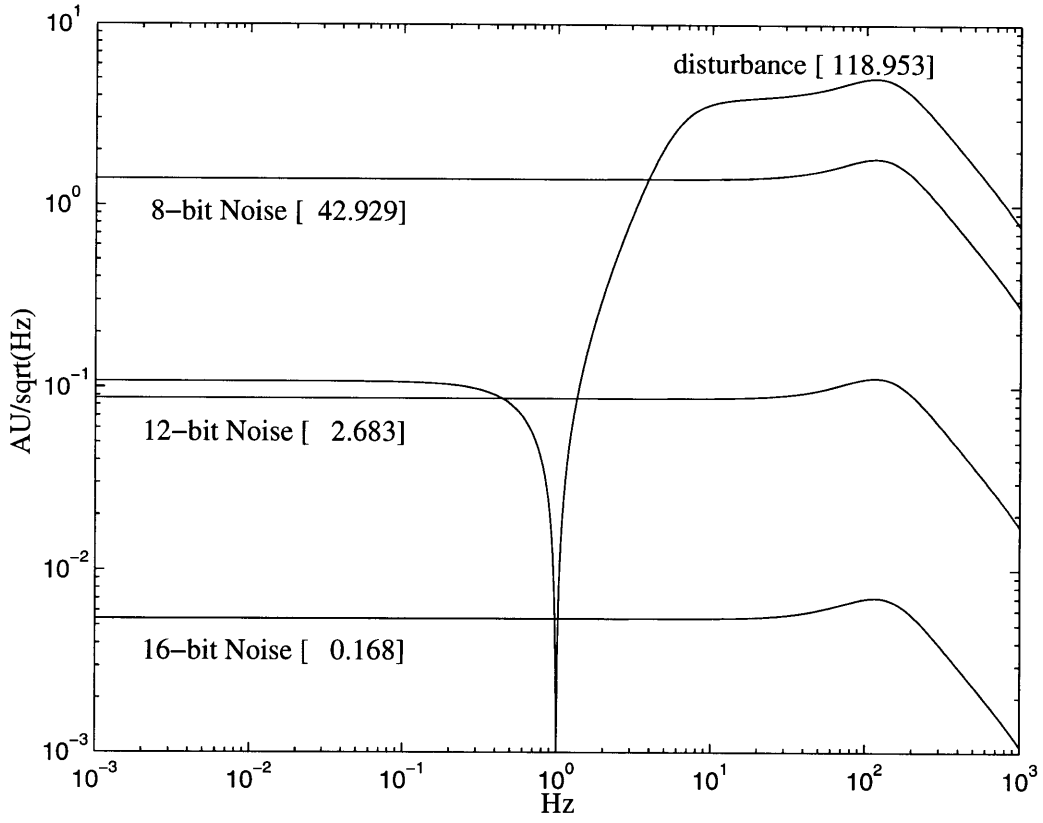

Figure 2.8: Incremental control cost due to actuation noise floor
(RMS values in brackets)

AU RMS. The 119 AU requirement just to reject the optical disturbance, bounded by the performance magin $\sigma = 3$, results in RMS noise floor magnitudes of 1.40, 0.0872 and 0.00545 AU RMS for 8, 12 and 16-bit D/A hardware, respectively. In other words, the additional 0.168 AU required by the 16-bit noise floor is well above the 0.00545 AU noise floor and, therefore, the corresponding analysis is valid. If the incremental actuation due to the noise floor was on the order of the noise floor, then the corresponding performance perturbation would be equivallent to the perturbation due to the noise floor if the control loop was not closed.

The increase in control cost and reduction in performance may require control design iteration and hardware redesign until the performance is met in the face of the noise floor. The incremental actuation due to the noise floor can be accounted in

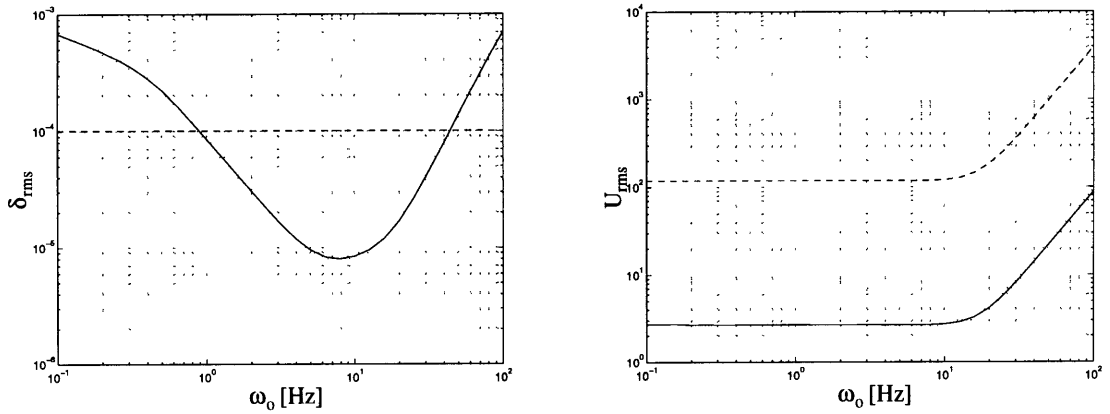

(a) Performance perturbation (solid line) performance requirement (dashed line)

(b) Cost perturbation (solid line) performance cost (dashed line)

Figure 2.9: Impact of suspension frequency on perturbation of (a) performance and (b) cost for 40 dB broadband disturbance rejection with 12 bit resolution

a few ways. The incremental actuation could be absorbed into the actuation margin thereby reducing the effective performance margin of safety, σ. Alternatively, the total actuator size could be increased by the incremental control effort. Doing so, however, increases the noise floor magnitude, thereby warranting further evaluation at the new Ξ_i. In addition, equations (2.22) through (2.24) could be invoked once the noise floor magnitude is established.

So far, the example problem has shown the incremental performance reductions and cost increases resulting from different magnitudes of the actuation noise floor. To evaluate the impact of suspension frequency on the cost and performance perturbations due to the noise floor, the previous model is utilized with the additional specification of 12-bit actuation hardware. Additionally, the damping ratio is set at $\zeta_o = 0.005$ and the system is evaluated for different suspension frequencies, ω_o.

The impact of structural stiffness is illuminated by Figure 2.9. Figure 2.9(a) shows the incremental RMS performance perturbation due to the noise floor and shows the target performance $\Delta_{rms} = 0.0001$. Similarly, Figure 2.9(b) shows the incremental RMS actuation cost due to the noise floor and shows the control cost to achieve the target performance in the absence of the noise floor. The benefits of stiffer suspension are clearly evident and well uderstood since plant disturbability decreases

with increasing stiffness. For the example problem, the performance perturbation due to the noise floor exhibits a significant decrease over $1 < \omega_o < 40$ Hz with the minimum over $7 \leq \omega_o \leq 10$ Hz. The incremental control cost due to the noise floor, however, is constant for $\omega_o < 10$ Hz. Therefore, the *best* suspension frequencies lie in the range $7 \leq \omega_o \leq 10$ Hz.

Examination of only optical disturbance rejection, as in the previous section, establishes an upper bound of approximately 10 Hz for *good* suspension frequencies. Inclusion of the noise floor further refines that range, for the example problem, to $7 \leq \omega_o \leq 10$ Hz. Although not directly addressed, practices for staged actuation can be infered from the previous example by designing each stage as follows:

(1) Increase the performance margin of safety, σ, to account for additional control cost due to the noise floor.

(2) Set initial bounds on the supension frequency as determined by satisfying performance in the absence of the actuation noise floor.

(3) Select the D/A resolution to be compatible with the amount of performance desired by a stage. (Need 12 bits for 99% optical disturbance rejection.)

(4) Refine the suspension frequency range by examining the closed-loop propagation of the noise floor to the performance metric.

Further refinements require more detailed models, but the results obtained by simple models are generally good first order approximations.

2.4 Numerical Conditioning

Synthesizing LQG controllers for a staged actuation device, such as an ODL, poses a challenge in conditioning the problem for numerical Riccati equation solvers. Staging is the result of a single actuator being incapable of providing necessary dynamic range and bandwidth. In a staged device, two or more actuators of different bandwidths and strokes are mated in series to achieve the desired characteristics. In a staged ODL, all

actuators control the same state, ODL position (or OPD), but with different precision. For example, the SITE ODL consists of a lead screw stage which provides centimeter level positioning at low frequencies, a voice coil which supplies a millimeter length stroke with a 100 Hz bandwidth, and a PZT which provides nanometer level precision with a kiloHertz bandwidth. In such a staged system, a simple LQG control design uses the PZT to accomplish the entire compensation task, especially since it behaves like a position actuator below one kilohertz. Such usage is inconsistent with the PZT capabilities. These constraints must be reflected in the mathematics. Limiting device strokes, however, is not sufficient. A lead screw is incapable of high frequency operation and, hence, must further have its actuation contribution frequency weighted to below 1 Hz. Similarly, since only the PZT is capable of high frequency operation, its usage at low frequencies would be inefficient, hence it should have its action weighted at higher frequencies.

Another issue which arises in multi-stage devices is that of state variable selection. A natural choice of state variables is that of inertially referenced position states, which are used when deriving the equations of motion in a Newtonian mechanics framework. Such state variables are a poor choice from a numerical conditioning perspective. For example, nanometer level displacements of the PZT are important in the ODL problem, yet this information is contained in the difference of two inertially referenced states which may have magnitudes on the order of meters. Hence, more than nine significant figures must be retained for the inertially referenced states in order to maintain just a few significant figures of PZT displacement. Similarly, retaining nanometer level positioning precision of the lead screw is inefficient and unrealistic. In order to preserve a uniform degree of significant figures for the various state values in the system, all states, control inputs, sensors and performance metrics should be normalized by their maximum desired or expected values. Such normalization results in dimensional units of percent stroke, range, force and performance. Doing so provides an equal number of significant figures for each state, thereby minimizing roundoff effects which become significant in matrix Riccati and Lyapunov solution procedures. This type of conditioning was found to be necessary to obtain viable

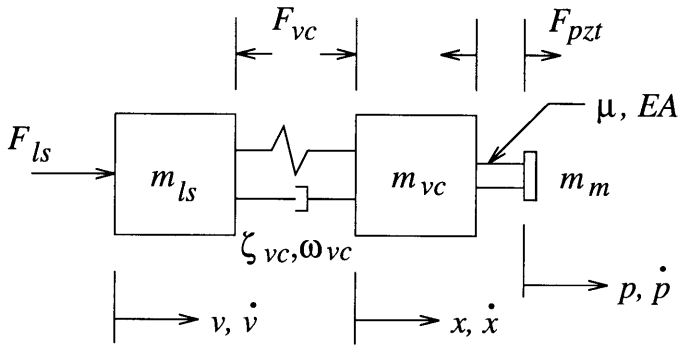

Figure 2.10: Three stage model of SITE ODL

solutions to the Riccati equations associated with LQG controller synthesis in the ODL problem.

As an example, the normalized equations of motion for the three stage SITE ODL, shown in Figure 2.10, are developed. In addition, the means and hazards involved with constraining device strokes and operational bandwidths are examined.

The equations of motion, derived using the Newtonian reference position states, v, x and p, for the lead screw, optical cage and ODL secondary flat mirror, are given by equation (2.25). Non-linear effects such as friction have been purposely neglected in the lead screw. The PZT is modeled as a consistent two-node rod type finite element, $q^T = [\ v \quad x \quad p\ ]$ is the position state vector and $f^T = [\ F_{ls} \quad F_{vc} \quad F_{pzt}\ ]$ is the control input vector.

$$M\,\ddot{q} + C\,\dot{q} + K\,q = Q\,f \tag{2.25}$$

$$M = \begin{bmatrix} m_{ls} & 0 & 0 \\ 0 & m_{vc} + \frac{1}{3}m_{pzt} & \frac{1}{6}m_{pzt} \\ 0 & \frac{1}{6}m_{pzt} & m_m + \frac{1}{3}m_{pzt} \end{bmatrix} \tag{2.26}$$

$$C = \begin{bmatrix} c_{vc} & -c_{vc} & 0 \\ -c_{vc} & c_{vc} + c_{pzt} & -c_{pzt} \\ 0 & -c_{pzt} & c_{pzt} \end{bmatrix} \tag{2.27}$$

$$K = \begin{bmatrix} k_{vc} & -k_{vc} & 0 \\ 0 & k_{vc} + k_{pzt} & -k_{pzt} \\ 0 & -k_{pzt} & k_{pzt} \end{bmatrix} \tag{2.28}$$

$$Q = \begin{bmatrix} 1 & -1 & 0 \\ 0 & 1 & -1 \\ 0 & 0 & 1 \end{bmatrix} \tag{2.29}$$

The damping matrix, C, is in terms of the voice coil and PZT damping coefficients, c_{vc} and c_{pzt}, instead of modal type parameters, ζ_{vc} and ζ_{pzt}. Similarly, the stiffness matrix is in terms of true physical stiffnesses.

Considering that the states of interst are the voice coil and PZT displacements and not the optical component absolute positions, the dynamics are better represented by introducing the transformation (2.30) which relates the inertially referenced states v, x and p to the actuator displacement states v, ξ and η.

$$\begin{bmatrix} v \\ \xi \\ \eta \end{bmatrix} = \begin{bmatrix} 1 & 0 & 0 \\ -1 & 1 & 0 \\ 0 & -1 & 1 \end{bmatrix} \begin{bmatrix} v \\ x \\ p \end{bmatrix} \tag{2.30}$$

Inverting, the desired transform , T, is obtained.

$$\begin{bmatrix} v \\ x \\ p \end{bmatrix} = \begin{bmatrix} 1 & 0 & 0 \\ 1 & 1 & 0 \\ 1 & 1 & 1 \end{bmatrix} \begin{bmatrix} v \\ \xi \\ \eta \end{bmatrix} \tag{2.31}$$

Substitution of equation (2.31) into equation (2.25) gives

$$MT\,\ddot{\tilde{q}} + CT\,\dot{\tilde{q}} + KT\,\tilde{q} = Q\,f \tag{2.32}$$

where $\tilde{q}^T = [\ v \quad \xi \quad \eta\ ]$ is the *actuator* position state vector. Since the effective scales of these displacements are meters, millimeters and micrometers, it is desirable to scale the transformed variables to coincide with percent device stroke. To do this, introduce a diagonal matrix of state scale factors, N.

$$\tilde{x} = N\bar{x} \tag{2.33}$$

$$N = \begin{bmatrix} max(v) & 0 & 0 \\ 0 & max(\xi) & 0 \\ 0 & 0 & max(\eta) \end{bmatrix} \tag{2.34}$$

Similarly, the control vector may be scaled by appropriate masses, forces or other metrics. For example, it is desirable to have the control vector in terms of normalized accelerations for the lead screw and voice coil stages and of commanded displacement for the PZT. An appropriate choice for the force scale transformation, F, is given by (2.36).

$$f = F\bar{f} \tag{2.35}$$

$$F = \begin{bmatrix} m_{ls} & 0 & 0 \\ 0 & m_{vc} & 0 \\ 0 & 0 & k_{pzt} \times 10^{-6} \end{bmatrix} \tag{2.36}$$

Introducing the actuator force scales into the equations of motion provides the final normalized equations of motion as

$$MTN\ddot{\bar{q}} + CTN\dot{\bar{q}} + KTN\bar{q} = QF\bar{f} \tag{2.37}$$

where $\bar{q} = [\ \bar{v}\ \ \bar{\xi}\ \ \bar{\eta}\ ]$ is now the normalized state vector which has units of percent device strokes. Also, $\bar{f} = [\ \bar{u}_{ls}\ \ \bar{u}_{vc}\ \ \bar{u}_{pzt}\ ]$ is the normalized control vector. Compacting the notation,

$$\bar{M}\ddot{\bar{q}} + \bar{C}\dot{\bar{q}} + \bar{K}\bar{q} = \bar{Q}\bar{f} \tag{2.38}$$

For SITE, appropriate state and force scale matricies are

$$N = \begin{bmatrix} 0.02 & 0 & 0 \\ 0 & 0.002 & 0 \\ 0 & 0 & 4.0 \times 10^{-6} \end{bmatrix} \tag{2.39}$$

$$F = \begin{bmatrix} 0.001 \times m_{ls} & 0 & 0 \\ 0 & m_{vc} & 0 \\ 0 & 0 & k_{pzt} \times 10^{-6} \end{bmatrix} \tag{2.40}$$

which result in state units of 2 cm, 2 mm and 4 μm and actuation units of mm/s^2, m/s^2 and μm.

In order to limit actuator strokes, the corresponding actuator states, $\bar{\xi}$ and $\bar{\eta}$, are included as performance variables in addition to the OPD, δ, and control penalty variables μ_{ls}, μ_{vc} and μ_{pzt}. Hence, additional penalties, q_{vc} and q_{pzt}, may be placed directly against these states instead of increasing the associated control penalty. Introduction of the issue of performance metrics warrants completion of the equations of motion and inclusion of the sensor equation. Since the equations become large for this problem, a contracted notation will be utilized from the outset and is given by equation (2.41).

$$\begin{bmatrix} \dot{x} \\ z \\ y \end{bmatrix} = \begin{bmatrix} A & B_w & B_u \\ C_z & D_{zw} & D_{zu} \\ C_y & D_{yw} & D_{yu} \end{bmatrix} \begin{bmatrix} x \\ w \\ u \end{bmatrix} \tag{2.41}$$

Unless stated otherwise, the variable x will be used to denote the entire state vector instead of the optical cage position as used earlier. The disturbance vector, w contains three disturbances which correspond to the actuation noise floors (process noise) of the actuators, one optical disturbance and one sensor noise. The control vector u is the three normalized control inputs. The only sensor, y, measures the OPD in the presence of the sensor noise. The performance vector, z, contains the OPD, three control penalty variables, and the relative normalized voice coil and PZT displacement states. The system dynamics are defined relative to the plant and disturbance dynamics $[A_p, B_p, C_p, D_p]$ and $[A_\phi, B_\phi, C_\phi, D_\phi]$, respectively. The $2n$ dimensional disturbance dynamics $[A_\phi, B_\phi, C_\phi, D_\phi]$ characterize the optical disturbance which is driven by white Gaussian noise w_o of intensity Ξ_o. The actuation noise floors are considered white Gaussian noises of intensities Ξ_{ls}, Ξ_{vc} and Ξ_{pzt}. The sensor noise, n_s, is also white Gaussian noise but of intensity θ. The variables are defined as follows:

$$x^T = [\ \bar{v}\ \ \bar{\xi}\ \ \bar{\eta}\ \ \dot{\bar{v}}\ \ \dot{\bar{\xi}}\ \ \dot{\bar{\eta}}\ \ \phi_1\ \ \phi_2\ \ \ldots\ \ \phi_n\ \ \dot{\phi}_1\ \ \dot{\phi}_2\ \ \ldots\ \ \dot{\phi}_n\ ] \tag{2.42}$$

$$z^T = [\ \delta\ \ \mu_{ls}\ \ \mu_{vc}\ \ \mu_{pzt}\ \ \bar{\xi}\ \ \bar{\eta}\ ] \tag{2.43}$$

$$w^T = [\ w_{ls}\ \ w_{vc}\ \ w_{pzt}\ \ w_o\ \ n_s\ ] \tag{2.44}$$

$$u^T = [\ \bar{u}_{ls}\ \ \bar{u}_{vc}\ \ \bar{u}_{pzt}\ ] \tag{2.45}$$

The performance and sensor variables are yet to be normalized. As with the states, introduce appropriate normalization values. For example,

$$z = P\bar{z} \tag{2.46}$$

$$y = S\bar{y} \tag{2.47}$$

$$P = \begin{bmatrix} \Delta_{rms} & 0 & 0 & 0 & 0 & 0 \\ 0 & 1 & 0 & 0 & 0 & 0 \\ 0 & 0 & 1 & 0 & 0 & 0 \\ 0 & 0 & 0 & 1 & 0 & 0 \\ 0 & 0 & 0 & 0 & max(\xi) & 0 \\ 0 & 0 & 0 & 0 & 0 & max(\eta) \end{bmatrix} \tag{2.48}$$

$$S = \begin{bmatrix} \Delta_{rms} \end{bmatrix} \tag{2.49}$$

To ease notation, y and z refer to the *normalized* values unless otherwise stated. The performance variable, δ, and the sensor are both normalized to the performance requirement, Δ_{rms}, and the control penalty variables are already normalized. The actuator strokes are normalized to their maximum displacements to cancel the normalization in equation (2.58), thereby recovering $\bar{\xi}$ and $\bar{\eta}$. Unlike the remaining variables, the sensor variable is required to retain over nine significant figures since it measures the absolute OPD. This characteristic is real and necessary for the ODL to meet the performance requirement. The plant dynamics are given by

$$A_p = \begin{bmatrix} 0 & I \\ -\bar{M}^{-1}\bar{K} & -\bar{M}^{-1}\bar{C} \end{bmatrix} \tag{2.50}$$

$$B_p = \begin{bmatrix} 0 \\ \bar{M}^{-1}\bar{Q} \end{bmatrix} \tag{2.51}$$

$$C_p = \begin{bmatrix} 2max(v) & 2max(\xi) & -2max(\eta) & 0 & 0 & 0 \end{bmatrix} \tag{2.52}$$

$$D_p = \begin{bmatrix} 0 & 0 & 0 \end{bmatrix} \tag{2.53}$$

The system dynamics are defined as follows:

$$A = \begin{bmatrix} A_p & 0 \\ 0 & A_\phi \end{bmatrix} \tag{2.54}$$

$$B_w = \begin{bmatrix} B_d & 0 & 0 \\ 0 & B_\phi & 0 \end{bmatrix} \tag{2.55}$$

$$B_d = B_p \begin{bmatrix} \sqrt{\Xi_{ls}} & 0 & 0 \\ 0 & \sqrt{\Xi_{vc}} & 0 \\ 0 & 0 & \sqrt{\Xi_{pzt}} \end{bmatrix} \tag{2.56}$$

$$B_u = \begin{bmatrix} B_p \\ 0 \end{bmatrix} \tag{2.57}$$

$$C_z = P^{-1} \left[\begin{array}{cccccc|c} 2max(v) & 2max(\xi) & -2max(\eta) & 0 & 0 & 0 & C_\phi \\ 0 & 0 & 0 & 0 & 0 & 0 & 0 \\ 0 & 0 & 0 & 0 & 0 & 0 & 0 \\ 0 & 0 & 0 & 0 & 0 & 0 & 0 \\ 0 & q_{vc}max(\xi) & 0 & 0 & 0 & 0 & 0 \\ 0 & 0 & q_{pzt}max(\eta) & 0 & 0 & 0 & 0 \end{array}\right] \tag{2.58}$$

$$C_y = S^{-1} \begin{bmatrix} C_p & C_\phi \end{bmatrix} \tag{2.59}$$

$$D_{zw} = P^{-1} \begin{bmatrix} 0 & D_\phi & 0 \\ 0 & 0 & 0 \\ 0 & 0 & 0 \\ 0 & 0 & 0 \\ 0 & 0 & 0 \\ 0 & 0 & 0 \end{bmatrix} \tag{2.60}$$

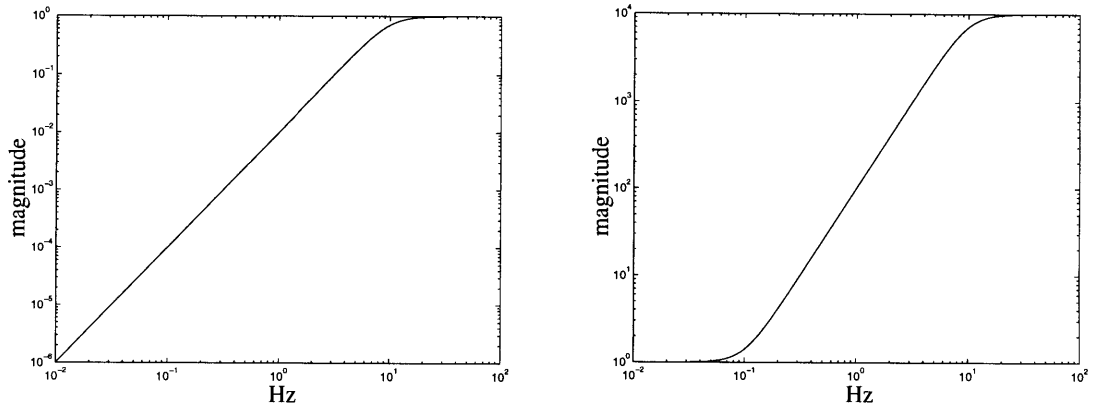

(a) low cost filter (b) high cost filter

Figure 2.11: Example bandwidth limiting filters

$$D_{zu} = P^{-1} \begin{bmatrix} 0 & 0 & 0 \\ \sqrt{\rho_{ls}} & 0 & 0 \\ 0 & \sqrt{\rho_{vc}} & 0 \\ 0 & 0 & \sqrt{\rho_{pzt}} \\ 0 & 0 & 0 \\ 0 & 0 & 0 \end{bmatrix} \tag{2.61}$$

$$D_{yw} = S^{-1} \begin{bmatrix} 0 & 0 & \sqrt{\theta} \end{bmatrix} \tag{2.62}$$

$$D_{yu} = S^{-1} \begin{bmatrix} D_p \end{bmatrix} \tag{2.63}$$

The control weighting penalties ρ_{ls}, ρ_{vc} and ρ_{pzt} have been included in the dynamics, above. The only missing ingredients are the mathematics which weight the actuator usages versus frequency. Such frequency weighting may be performed in many ways. Two basic weightings are shown in Figure 2.11. Figure 2.11(a) is a 2nd order low cost filter which makes low frequency usage of the weighted actuator cheap. Figure 2.11(b), on the other hand, is a 2nd order high cost filter which penalizes usage of the weighted actuator in the high frequency range. Various combinations of these filters may be utilized to tailor the frequency ranges over which usage of the actuators are emphasized in the cost.

$$
\begin{aligned}
J_{LQ} &= E[z^T z] \\
&= E[x^T C_z^T C_z x + 2x^T C_z^T D_{zu} u + u^T D_{zu}^T D_{zu} u] \qquad (2.64)
\end{aligned}
$$

The weighting filter dynamics are appended to the system dynamics, thereby further increasing the system size. Weighting matrices which impose a high cost may introduce new conditioning problems. To examine this effect, consider the LQR cost functional given by equation (2.64). Without frequency weights on the controls, equation (2.64) produces three observations. First, $C_z^T D_{zu} = 0$. No cross terms exist. Second, $C_z^T C_z$ is of the order of unity, depending upon C_ϕ. Third, $D_{zu}^T D_{zu}$ is of the order of the control weights. Introduction of control frequency weights with dynamics $[A_\psi, B_\psi, C_\psi, D_\psi]$ produce several effects which worsen the conditioning. The cross term $C_z^T D_{zu}$ becomes non-zero. The term $C_z^T C_z$ is augmented with weighting state contributions which are of the order of $C_\psi^T R C_\psi$ where R is the diagonal matrix of control weights and C_ψ is the control filter output matrix which is of the order of the low frequency penalty. Hence, conditioning on the order of the square of the largest low frequency penalty arises within $C_z^T C_z$. Susequently, $D_{zu}^T D_{zu}$ is augmented with the terms $D_\psi^T R D_\psi$ where D_ψ has a magnitude corresponding to the high frequency penalty. Hence, $D_{zu}^T D_{zu}$ has a condition number on the order of the square of the largest high frequency penalty.

Since frequency weights on the controls are required to obtain LQG controllers which are consistent with actuator characteristics, numerical anomolies which arise from the conditioning may occur. These problems are a result of stiff penalties within the frequency weights and not adequately normalizing the problem. The only current means to alleviate this problem is to decouple the dynamics or increase the computational precision.

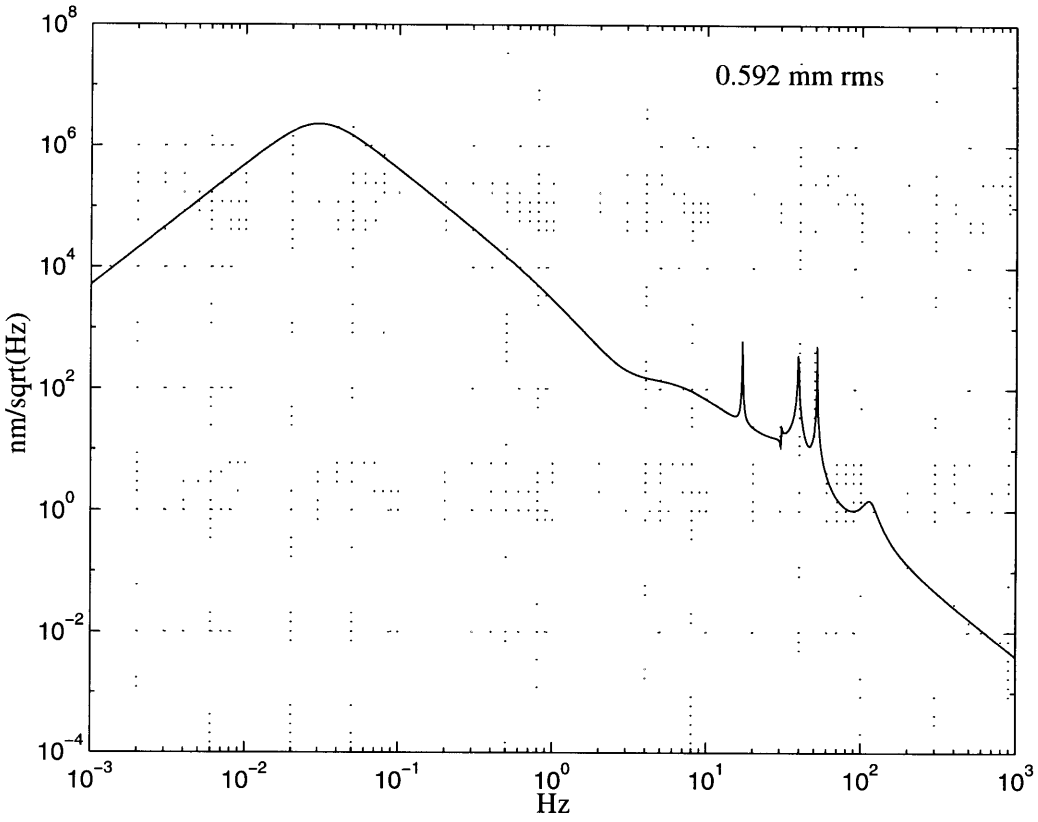

Figure 2.12: SITE optical pathlength difference autospectrum

2.5 SITE: A Design Example

In order to illustrate the design considerations of output disturbance rejection, this section examines the SITE optical delay line design problem. Being proposed to operate in the space shuttle main payload bay [2], the entire SITE interferometer is exposed to a disturbance environment which is composed of shuttle attitude control thruster firings, crew operations and numerous other disturbance sources. After being propagated through a model of the SITE platform, the optical pathlength disturbance autospectrum shown in Figure 2.12 is generated with a sample time history shown in Figure 2.13. In order for SITE to satisfy its overall science objective, an estimated 25 nm rms OPD is required.

To more clearly evaluate the results of sophisticated analyses, initial device char-

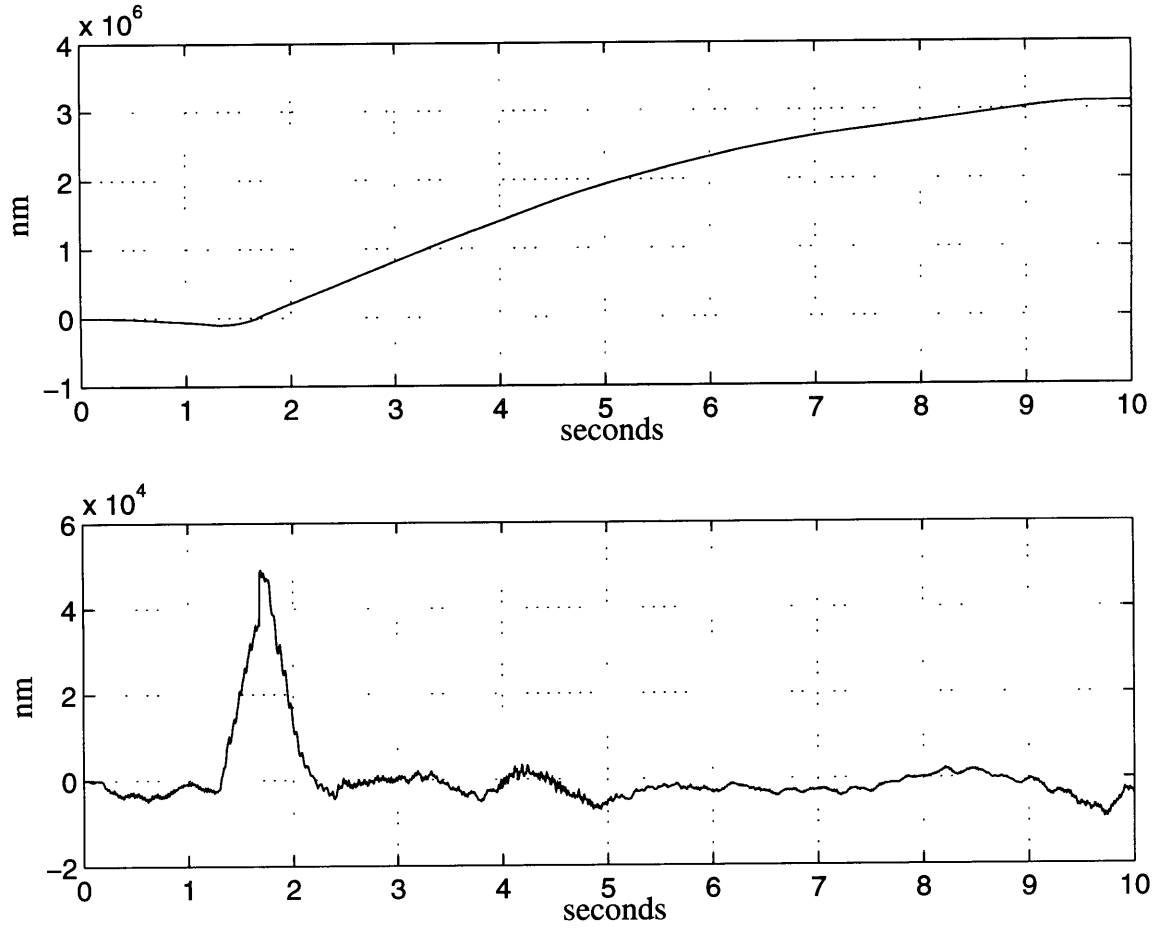

Figure 2.13: SITE optical pathlength difference unfiltered (top) and filtered [1 Hz] (bottom) time history

acteristics are estimated from known performance requirements and constraints. Afterwards, simple models provide good first order refinement to the preliminary characteristics. Finally, full detail models are utilized for final parametric trade off analysis. To assure a certain confidence in the design optimization, a performance margin, σ, of 3 is included in the subsequent studies.

Simplified bounding analysis is a crucial ingredient to identify permissible ranges of device characteristics, such as actuator strokes, with which to construct simple models for preliminary sizing. In addition, such analysis illuminates background parameters such as signal-to-noise ratios and bandwidths of associated electronics.

Two fundamental issues to address are how far each actuation level should move

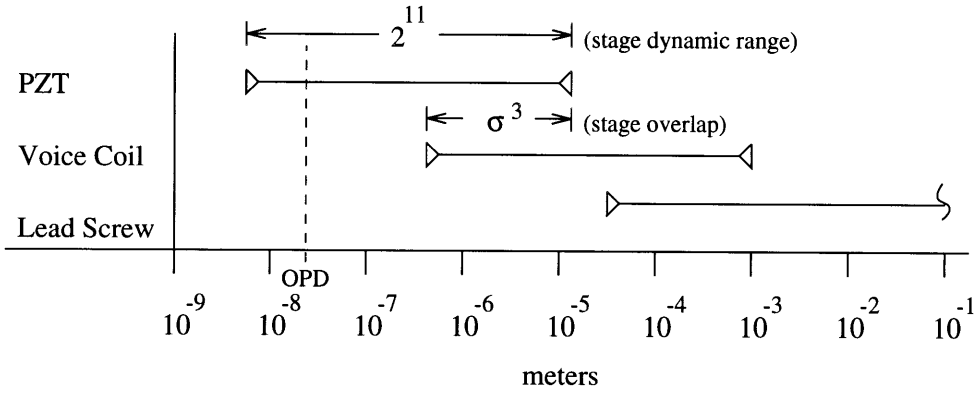

Figure 2.14: Dynamic ranges of SITE ODL stages

and how fast. The RMS disturbance, overbounded by a factor of 3, results in a total stroke of ± 1.7 mm RMS. The SITE OPD requirement of 25 nm results in 5 orders of magnitude of disturbance rejection. For reasons of cost and length, the SITE ODL optical $f\#$ is set at 5. Since the science light diameter is 25 mm, the parabolic mirror diameter is set at 80 mm, thereby setting the focal length, or nominal flat mirror position, at 240 mm. The maximum position error of the flat mirror relative to the focal point is established by the maximum amount of distortion of the science light which the ODL is permitted to cause. From more global program trade studies, this distortion level is set to correspond to a 5% reduction in the central fringe visibility. This further translates to a maximum depth of focus of 13 μm. Hence, the positioning contraints on the ODL are a maximum travel of at least 1.7 mm, at most 25 nm RMS OPD and a maximum of 13 μm of PZT displacement.

Using the maximum PZT displacement as a starting point and further assuming 12-bit stage dynamic range and a stage dynamic overlap of σ^3, the stage dynamic ranges may be determined as shown in Figure 2.14. The 12-bit (11 data bits plus 1 sign bit) dynamic range of the PZT results in a PZT resolution of 5.86 nm given a ± 12 μm stroke. Overlaping the PZT stroke by $\sigma^3 = 27$ gives a voice coil resolution of 0.444 μm and a stroke of ± 0.910 mm. The lead screw must have a resolution of 33.7 μm. Hence, a bounding and overlap exercise indicates that a 3 stage ODL with 12-bit stage dynamic ranges should be able to meet the performance requirements.

The critical undetermined modal parameter is the optical cage suspension fre-

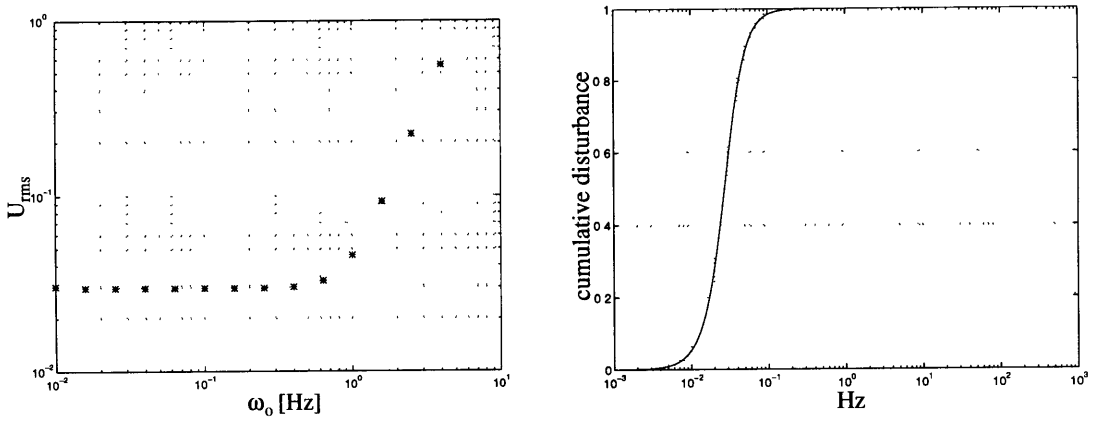

(a) Actuation cost versus suspension frequency

(b) Cumulative RMS disturbance

Figure 2.15: Suspension optimization for SITE ODL

quency. Barring resolution and noise arguments, a simple spring-mass-dashpot model is used to obtain the best suspension stiffness under the assumption that the SITE disturbance spectrum must be rejected to a residual RMS disturbance of 1.00 μm by the voice coil stage. As the damping ratio is of little importance, $\zeta_o = 0.005$ is assumed. In addition, the magnitudes and shapes of the spikes in the SITE disturbance autospectrum are reduced and broadened in the model since these spikes will manifest themselves in the form of zeros in the compensator. Effectively, the Kalman filter tends not to believe, and hence uses very low gain on, the sensor measurements in regions of high noise, which are indicated by the spikes. Deep compensator notches tend to be less stable, therefore, modifying the disturbance spike shapes in the model is an attempt to increase the stability robustness. In addition, this change in the model disturbance will help to provide robustness to frequency uncertainty in the spikes. The actual disturbance, however, is utilized in performance evaluation.

The rms actuation required to achieve the performance requirement of 1.00 μm OPD is shown versus suspension frequency in Figure 2.15(a). The cumulative RMS disturbance, defined by equation (2.65), is shown in Figure 2.15(b), where $\Phi_{dd}(\omega)$ is the disturbance power spectrum. As seen, most of the disturbance is located in the frequency range $0.01 \leq \omega \leq 0.1$ Hz. Much of the disturbance is due to the drift

between shuttle reaction control system thruster firings. The actuation cost, however, is relatively constant for suspension frequencies, ω_o, up to 0.5 Hz. The constant actuation effort for $\omega_o \leq 0.5$ Hz indicates that the control effort is dominated by control of the system inertia. Similarly, the linearly (on a log-log scale) increasing actuation effort for $\omega \geq 1$ Hz corresponds to actuation effort being dominated by control of the spring force. This balance of control effort between the inertia and spring forces determines the upper bound on *good* suspension frequencies. Note that the presence of the lead screw stage will desaturate some of the low frequency spring force requirement. This desaturation will shift the balance between the inertia and spring force dominated portions of Figure 2.15(a), thereby shifting the range of good suspension frequencies.

$$U_{cum} = \sqrt{\int_0^{\omega_d} \Phi_{dd}(\omega) d\omega} \tag{2.65}$$

Figure 2.16 shows the resulting actuation autospectrum for 0.01, 0.5 and 3.0 Hz suspensions with the corresponding cumulative RMS actuation shown in Figure 2.17. The two key features to note from Figure 2.16 are (1) the RMS actuation increase due to the increasing spring force, as indicated by the increasing low frequency actuation effort, and (2) the migration of the notch which corresponds to the suspension frequency. Figure 2.17 indicates, from a different perspective, how the voice coil effort shift from being dominated by high frequency usage to low frequency usage as the suspension frequency is changed from 0.01 Hz to 3.0 Hz.

The simple model provides an estimate of good suspension frequencies as being below 0.5 Hz. In order to futher understand the interactions of the three stage ODL and the associated design process, the model shown previously in Figure 2.10 is used to design an ODL with a 0.5 Hz suspension frequency. The lead screw stage is modeled as an unconstrained mass to which the optical cage suspension is attached. Since the mass of the PZT is greater than that of the flat mirror which it positions, the PZT is more appropriately modeled as a consistent 2 node rod type finite element instead of a massless spring.

High inertia actuators, such as lead screws, are usually modeled with the assump-

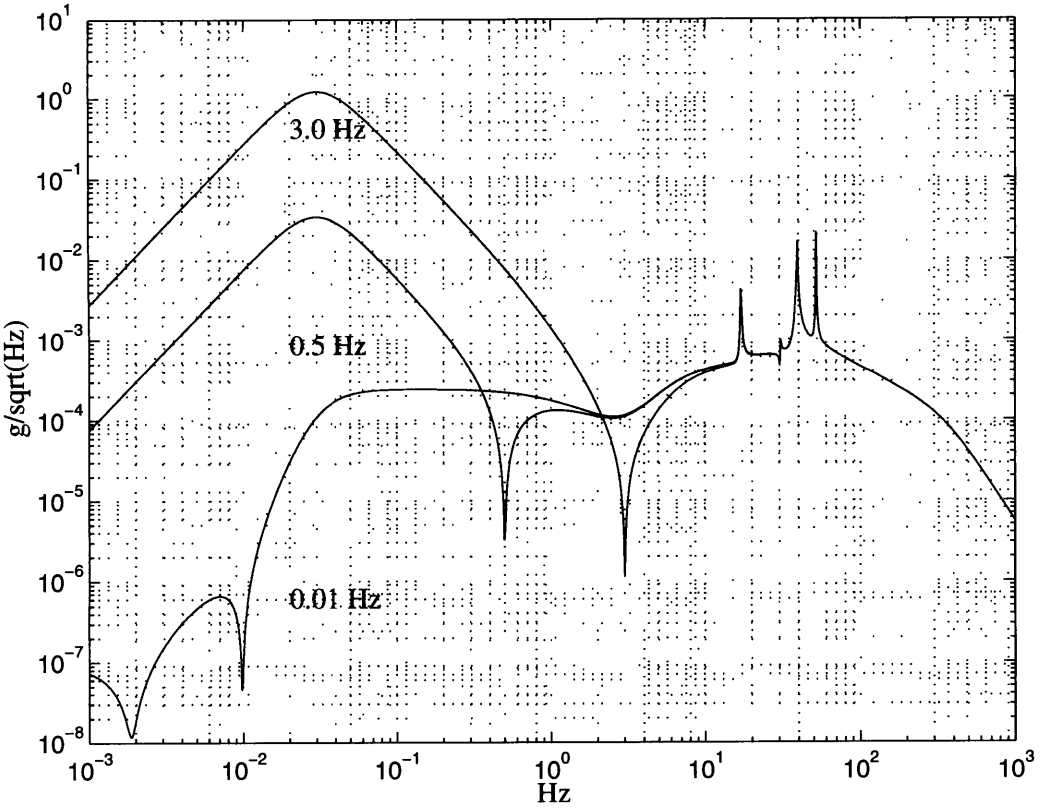

Figure 2.16: Actuation effort autospectra to obtain 1.0 μm rms OPD

tion of a locally closed servo loop such that the lead screw operation is position command. Doing so, however, precludes the inclusion of trade studies, such as relative bandwidths, between the lead screw and voice coil. Therefore, the dynamics of the lead screw are directly included. The high inertia nature of such a device can be represented as an effective mass, $\overline{M}$, as in equation (2.66) given the thread pitch, p, spindle diameter, D, and net rotary inertia,I_θ. An example lead screw with $I_\theta = 7.06 \times 10^{-6} kg - m^2$, $D = 13mm$ and $p = 1mm$ results in an effective mass of 27.9 kg. Physically, this results in a lead screw stage mass which is an order of magnitude greater than the voice coil stage mass. In turn, the voice coil stage mass is ten times that of the PZT.

$$\overline{M} = \frac{4\pi I_\theta}{D\, p\, tan\, \alpha} \tag{2.66}$$

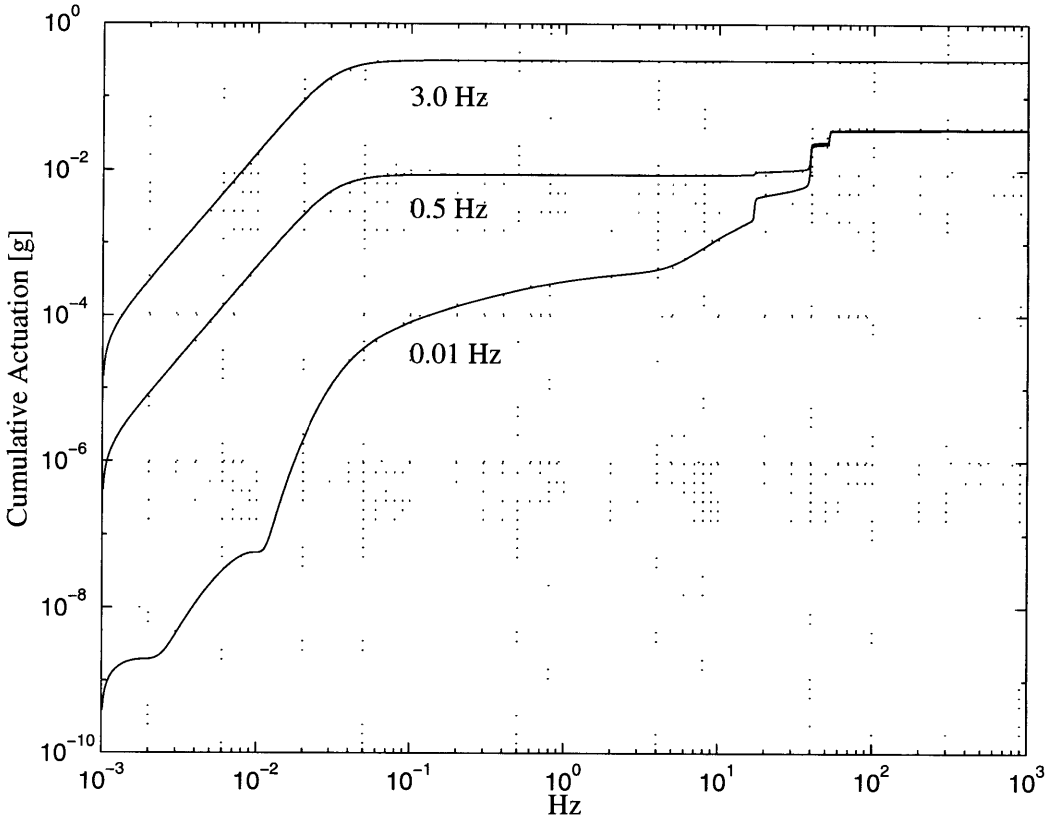

Figure 2.17: Cumulative RMS actuation effort to obtain 1.0 μm rms OPD

$$tan\,\alpha = \frac{\pi D}{p} \tag{2.67}$$

Since this exact problem was utilized to illustrate the normalization procedure for posing the ODL problem for numerical LQG solvers, the mathematics will not be repeated. Instead, the reader is referenced to Section 2.4.

In the previous section, the only free parameter was ω_o. Now that the lead screw and PZT have been added to the model, the distribution of the compensation task must also be considered. In other words, RMS levels of relative stage stroke, ξ and η, as well as stage operational bandwith are also undetermined. Like the suspension frequency, the maximum voice coil and PZT stage strokes ξ and η, respectively, are inputs to the problem in the sense that they are parameters which should be specified, or constrained. Within the computational framework of the LQG problem,

however, these parameters are outputs of the problem. The LQG problem inputs are the plant model (which includes the suspension frequency), the disturbance model, the performance metrics and the control weights. Hence, given a fixed plant, the results of the LQG problem are determined by control weighting factors, performance weights, sensor noise level and disturbance intensity. Since all of these weights may be frequency weighted, clarity in the influence of these LQG input parameters is lost. Therefore, in order to simultaneously achieve the required OPD, voice coil stage stroke, and PZT stage stroke, the input parameters must be varied in an iterative procedure. Instead of revisiting the suspension frequency optimization with this more complex model, a single design is examined. From this single example, a fundamental understanding of the design process and its complexity is illuminated.

The iterative procedure utilized is to fix the plant characteristics, the disturbance intensity, the sensor noise intensity and the performance weight. In doing so, the only remaining input parameters to the problem are the frequency weighted control weights for the lead screw, voice coil, and PZT control inputs. In effect, everything is fixed except the actuator force levels, or sizes, and their respective bandwidths. Iteration on these parameters is performed until the following criteria are met or shown impossible to meet:

(1) RMS OPD < 25 nm

(2) PZT stroke < 4 μm

(3) Voice coil stroke < 1 mm

(4) Lead screw bandwidth ~ 1 Hz

(5) Voice coil bandwidth ~ 100 Hz

(6) Distribution of RMS actuator usage spread out over the device operational bandwidth. For example, using the entire PZT stroke to compensate low frequency disturbancies is inefficient.

In order to somewhat balance the sensors and actuators, the sensor noise is then

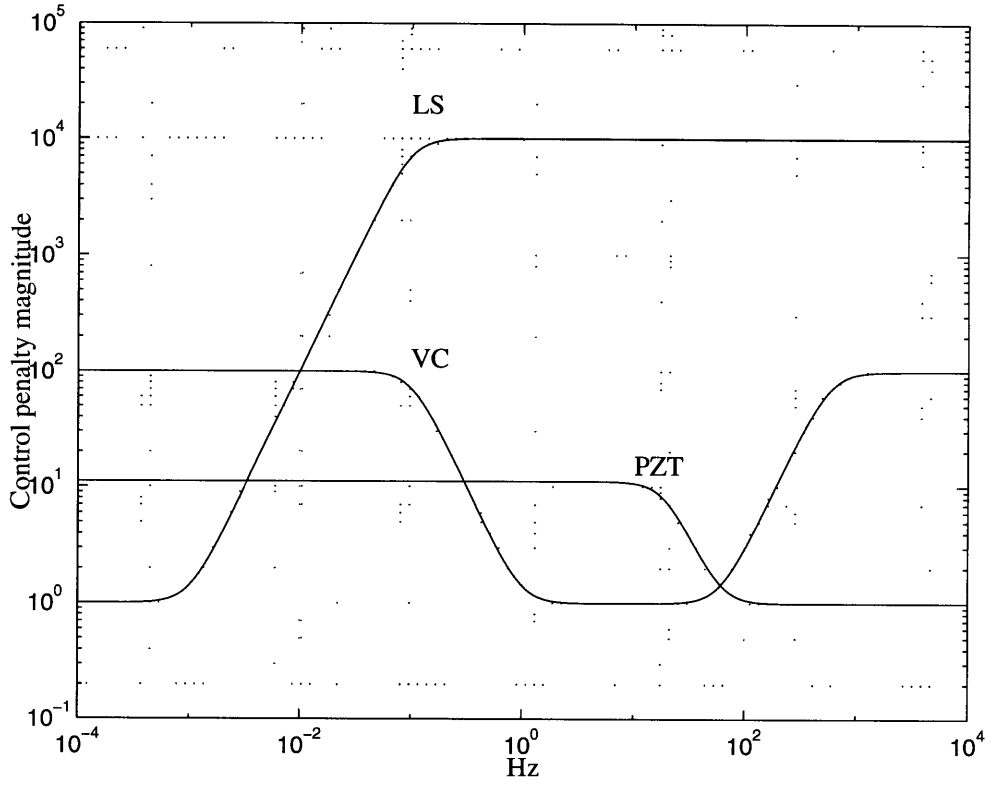

Figure 2.18: Control weights versus frequency for the lead screw (LS), voice coil (VC) and PZT actuators

adjusted so that the Kalman filter and regulator gains are of the same order of magnitude.

For a suspension frequency of 0.5 Hz, one such system design is performed. In order to attain satisfactory actuator bandwidths, the frequency weighting on the control weights shown in Figure 2.18 are used. Effectively, high frequency use of the lead screw and voice coil is penalized. Similarly, low frequency use of the voice coil and PZT is discouraged by high control weights. The filters basically make usage of a particular actuator cheap over the desired range of operation and expensive everywhere else. Iteration of these weights in both frequency and magnitude is required to achieve satisfactory results. As shown in Figure 2.19, these weights are successful in tailoring the actuator bandwidths. The resulting crossover frequencies and bandwidths are detailed in Table 2.2. As seen in Figure 2.19, the PZT loop provides a uniform level

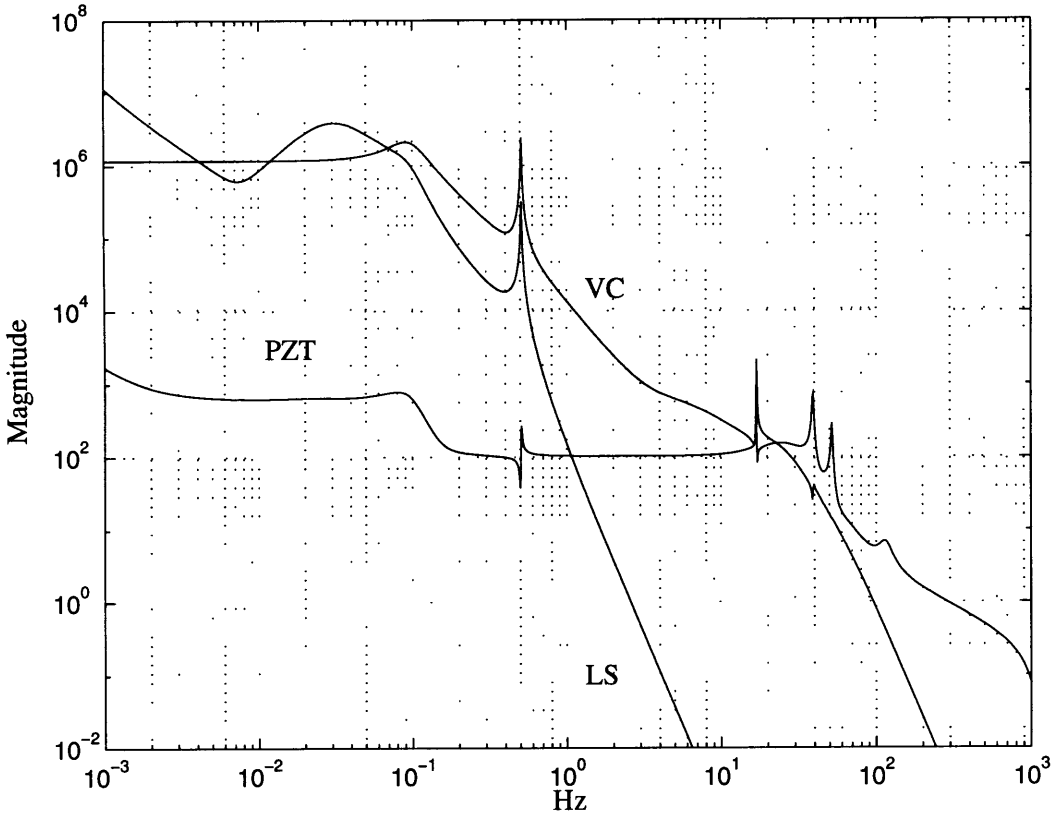

Figure 2.19: ODL loop magnitudes for the lead screw (LS), voice coil (VC) and PZT stages

of loop gain down to low frequencies in order to provide its high resolution capabilities over the entire ODL bandwidth. The PZT further provides most of the compensation for the disturbance spikes above 10 Hz, where the PZT high frequency capabilities are useful. Due to its mass, approximately 2 kg, the voice coil stage would excite these modes. Therefore, compensation of these higher frequency spikes is better accomplished through the PZT rather than the voice coil. Both the lead screw and voice coil are used to obtain the high loop gain at low frequencies necessary to reject the large disturbance content due to the steady drift of the shuttle between attitude control system (ACS) thruster firings. The total SISO loop transmission is shown in Figure 2.20. As seen, the resulting system has a gain margin $>$ 10 dB and phase margin $>$ 30 degrees. Since the phase drops below -180 degrees at several frequencies

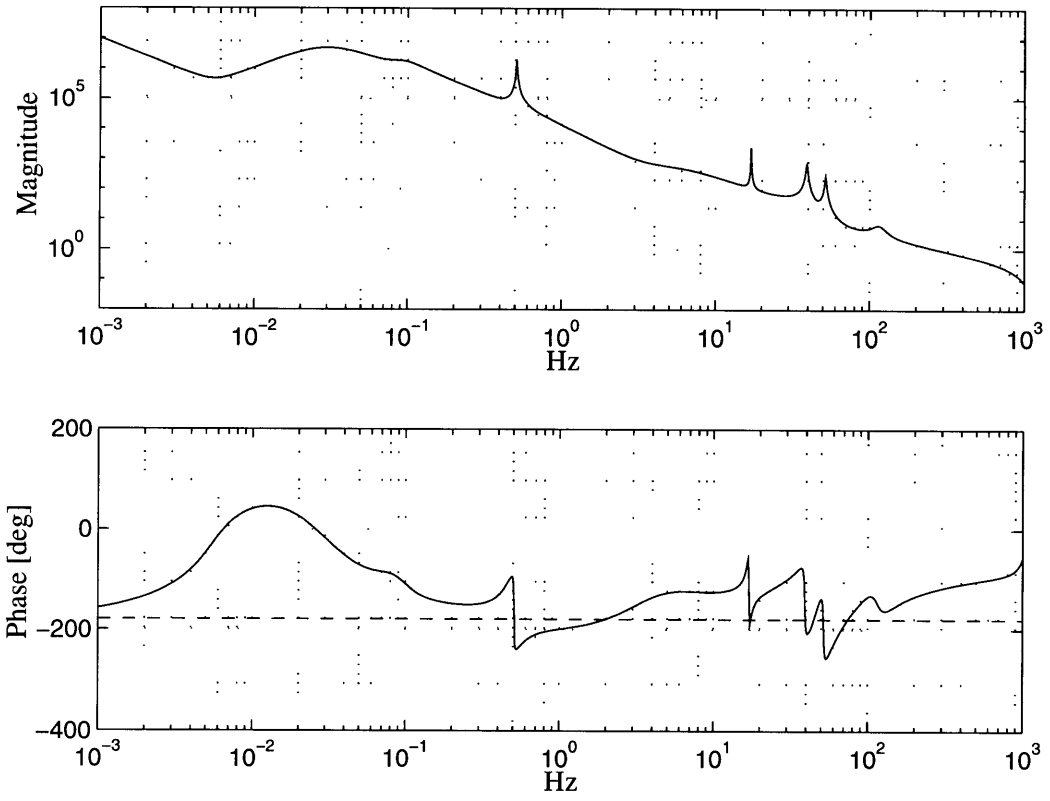

Figure 2.20: ODL total loop gain and phase

below the loop gain crossover, both upward and downward gain margins must be observed.

Figure 2.21 shows the 1.7 mm RMS optical disturbance and the resulting 15 nm RMS OPD. With the exception of the spikes between 10 and 100 Hz, the ODL is good at uniformly reducing the disturbance transmission to OPD. The spikes could be better rejected by not artificially reducing their magnitude in the Kalman filter disturbance model. As previously discussed, doing so would reduce the performance robustness to frequency uncertainty in these modes. Time simulation results are shown in Fugures 2.22 and 2.23. The OPD, shown in Figure 2.22, is generally below 25 nm. The only major deviation is during the shuttle ACS thruster firing period near 1.75 seconds. Since the OPD during this time exceeds 200 nm, either additional measures must be taken to reduce this disturbance throughout the interferometer or science data acquisition should not be performed during this time period. The

Table 2.2: Stage bandwidth to reject the SITE optical disturbance

Stage	ω_c Hz	BW Hz
LS	2.6	2.8
VC	95	103
PZT	285	385

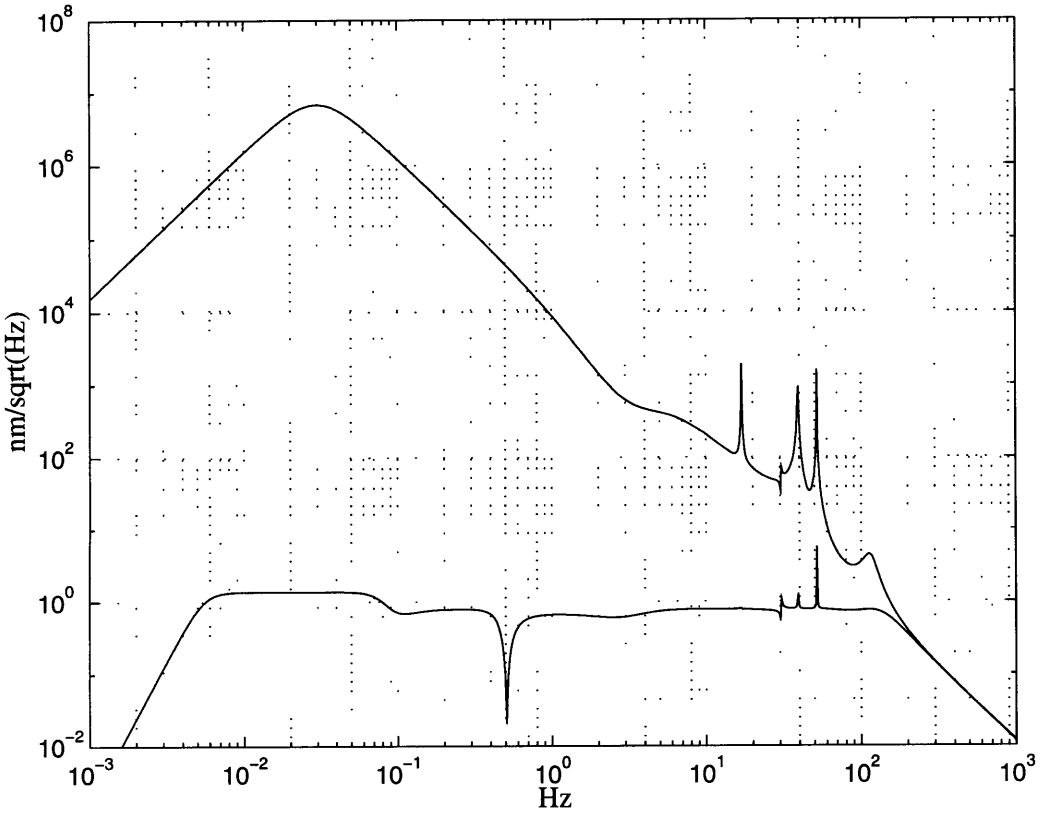

Figure 2.21: SITE Optical disturbance and resulting OPD autospectra

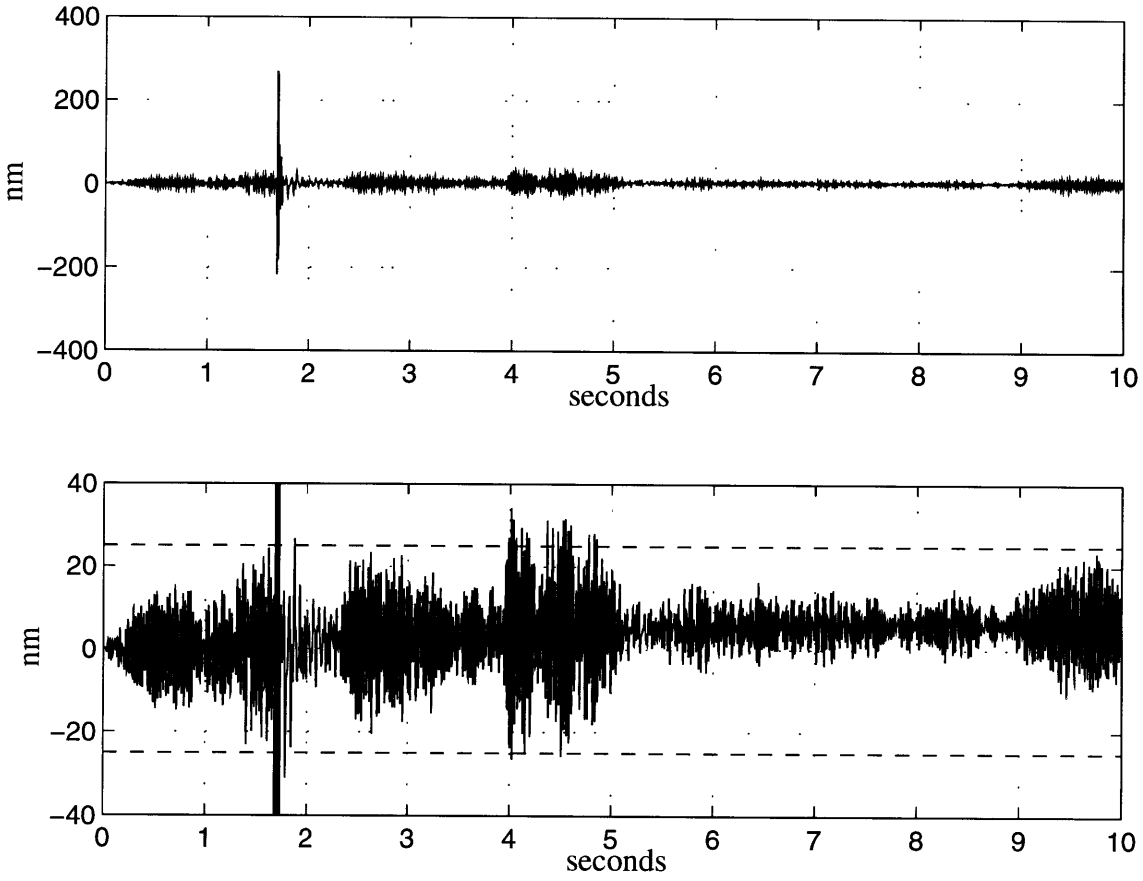

Figure 2.22: OPD time history due to SITE optical disturbance

resulting actuator forces u_{ls}, u_{vc}, and u_{pzt}, and their strokes v, ξ, and η, respectively, are shown in Figure 2.23. The time simulation indicates that 0.3 N force and 6 μm stroke capabilities for the voice coil and PZT, respectively, are required. Since time history of the voice coil force, u_{vc}, is relatively constant compared to its stroke, ξ, the force requirement is dominated by controlling the stage inertia rather than the spring force. In other words, the 0.5 Hz suspension frequency is not requiring significant effort just to overcome the spring force, and, therfore, is a good suspension frequency. This is not necessarily the best design, but it is considered a good design, which is the underlying objective of the structural design process.

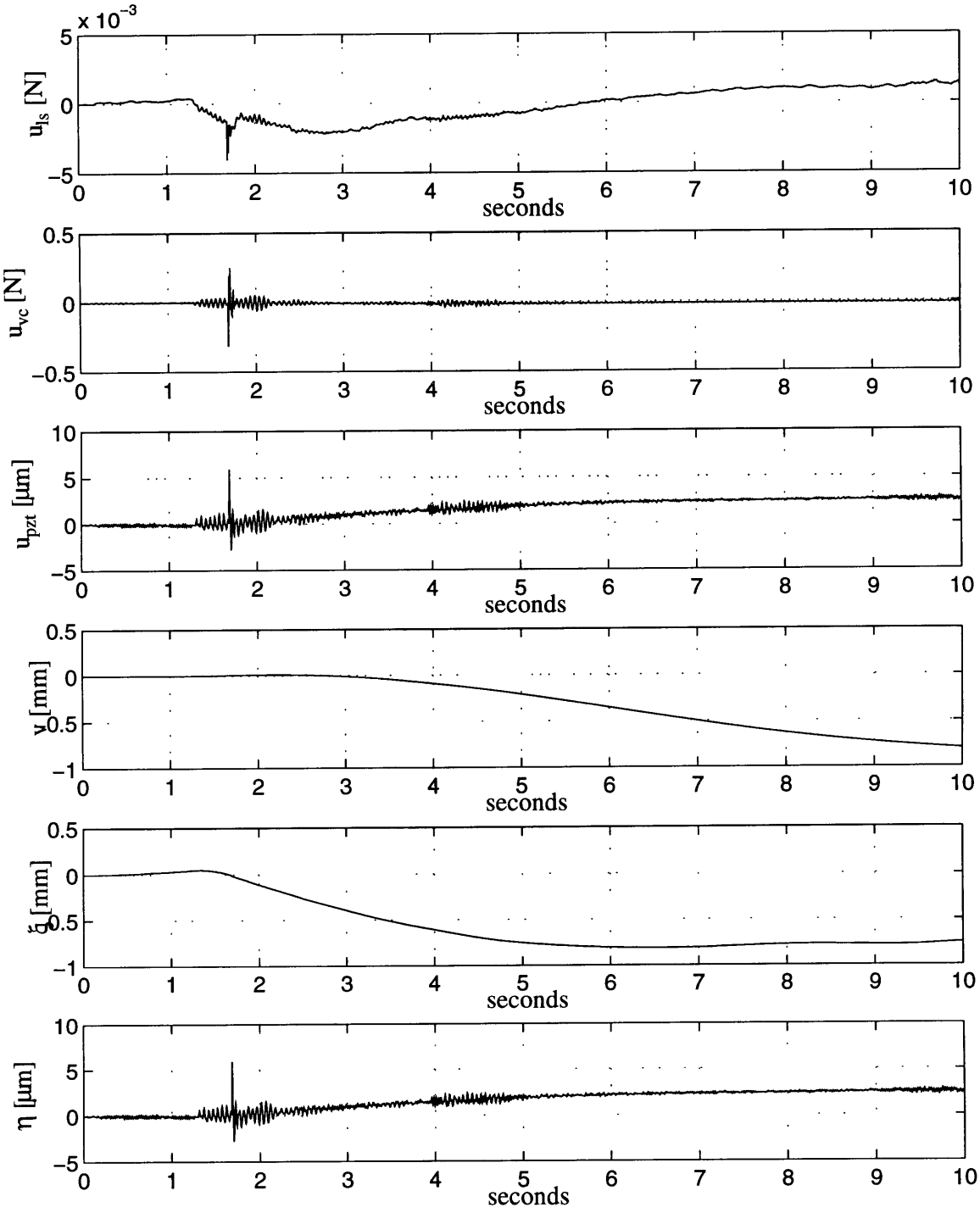

Figure 2.23: Actuator force and stroke time histories due to SITE optical disturbance

Chapter 3

Experimental Structural Characterization and Control of the JPL Phase B Optical Delay Line

Experimental characterization of the optical delay line provides a more accurate model with which to evaluate the true performance and stability margins of the device. Being traceable to both past and future ODL designs, the JPL Phase B ODL is a useful device for experimental investigations. The mechanical design of the Phase B ODL is explored in great depth to obtain insight into its static and dynamic behavior. After the ODL is characterized, successively higher bandwidth LQG based compensators are implemented on Phase B ODL test data to evaluate overall performance limitations. In addition, the relative cost, i.e. actuator size and sensor resolution, to attain increasing performance is evaluated.

The Mark III optical delay line and its successors have undergone extensive operational testing and optical and control developments [3] [6] [5] [15] [7] [8]. The JPL Phase B delay line was developed as an experimental testbed to investigate the impact of platform flexibility. Since the JPL Phase B ODL is similar in design to the Mark III ODL and future optical delay lines, experimental investigations using the

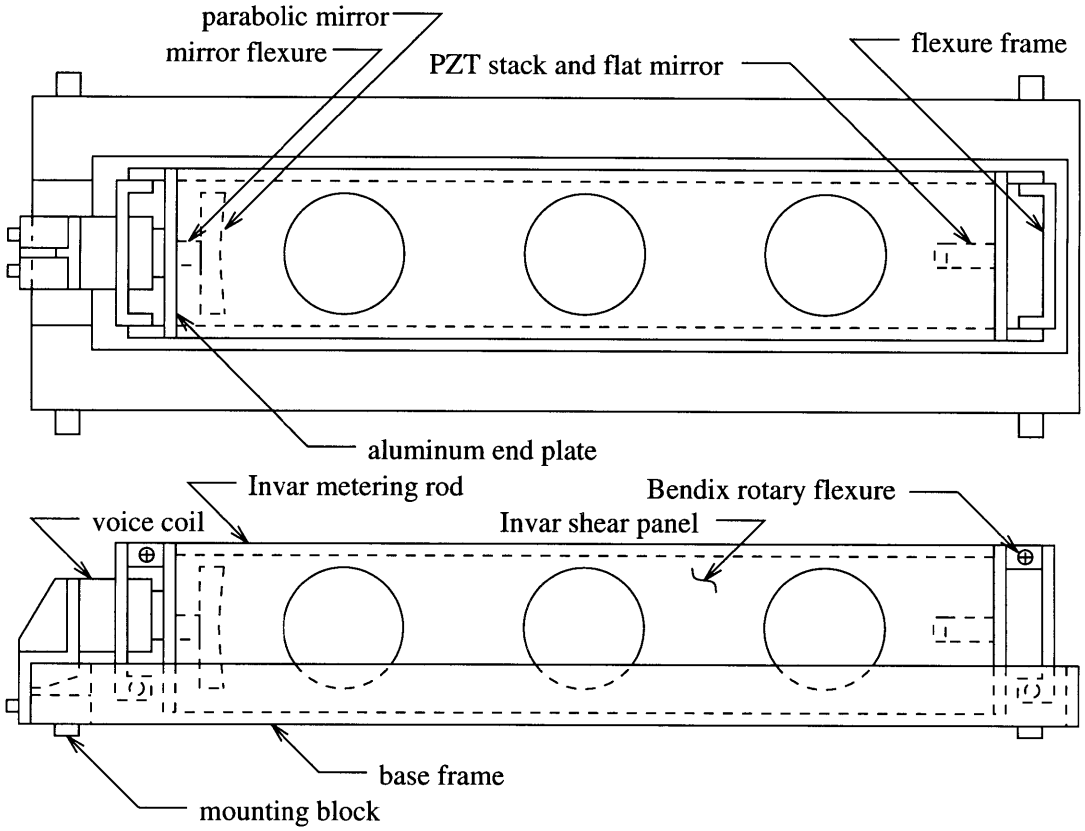

Figure 3.1: JPL Phase B Optical delay Line

JPL ODL are compatible with previous and future devices.

The Phase B ODL only consists of the voice coil and PZT stages, as shown in Figure 3.1. The optical cage suspension is an inverted parallelogram configuration with a support frequency of 0.56 Hz. The optical configuration is a standard cat's eye retroreflector with an optical f# of 5. The mass of the optical cage is approximately 13 kg, therefore actuation of the voice coil is expected to significantly *reactuate* the support platform. A second PZT, not shown in the figure, is located back-to-back with the PZT which actuates the flat mirror. By driving both PZTs with the same signal such that they both expand and contract simultaneously, a near zero net force exists at the PZT interface with the optics cage. This *reactuation* further decouples the high frequency dynamics of the PZT actuator from the voice coil stage dynamics.

The MIT laboratory setup of the Phase B delay line is shown in Figure 3.2 as part of a measurement interferometer on an optics bench. In an operational science

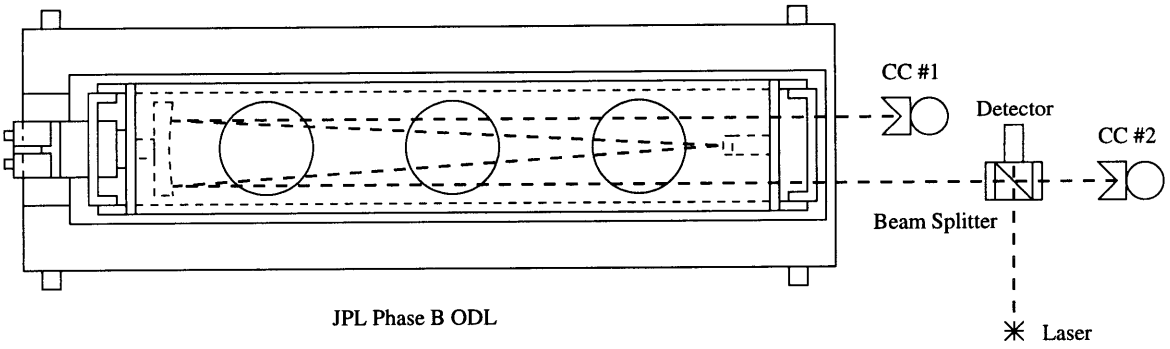

Figure 3.2: Phase B ODL setup at MIT

interferometer, such a measurement interferometer is used to measure the optical pathlength difference (OPD) due to vibration of the optical components. Since the science light and measurement, or *metrology*, beam traverse the same internal optical path, rejecting these OPD fluctuations in the metrology system rejects the same OPD fluctuations in the science light. The dynamics of the two corner cube retroreflectors, cc #1 and cc #2, interact with the voice coil stage dynamics. This coupling provides a flavoring of control structure interactions which will occur in a full scale device.

The transfer function from voice coil force input, F_{vc}, to the laser measurement output, δ, is shown in Figure 3.3. Many more modes exist than are captured by a simple spring-mass-dashpot model, yet the need to include these modes is dependent upon the required bandwidth of the voice coil stage. Regardless, these unmodeled modes ultimately limit the system performance and are instructive to identify.

Immediate performance hurdles evident in Figure 3.3 are the 360 degree phase loss at 86 Hz and the poor characterization near 170 Hz. Further investigations identify the 360 degree phase loss at 86 Hz as being caused by the coallescence of the voice coil mount first bending mode with the first mode of corner cube #1. The addition of a backing plate to the voice coil mount interface with the base frame, as shown in Figure 3.4, shifts the voice coil mount mode to 98 Hz and cleans up the voice coil to laser transfer function, shown in Figure 3.5. The phase fluctuation near 170 Hz is more clearly identified as another 360 degree phase loss, this time due to the presence of a complex pole and a complex non-minimum phase zero combination. A sine sweep on the voice coil input, without the backing plate, reveals that the response bifurcates

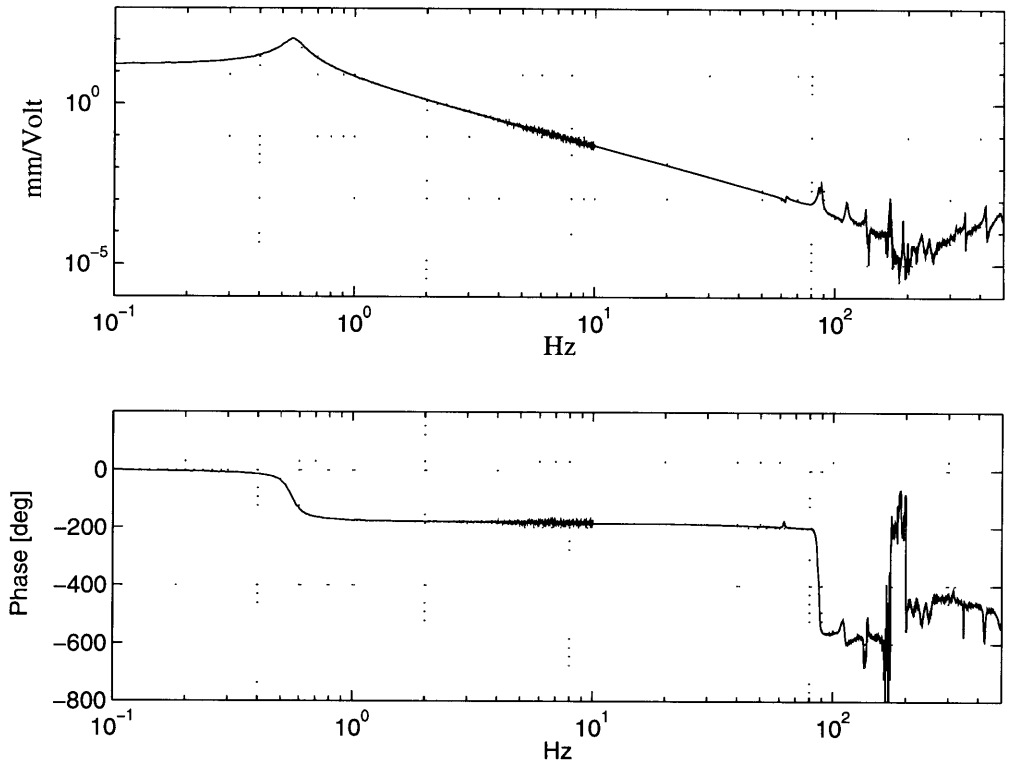

Figure 3.3: Measured voice coil to laser transfer function

for a 86 Hz voice coil actuation frequency as shown in Figure 3.6. This bifurcation has a very strong second harmonic component. Coincidentally, the second 360 degree phase loss occurs near this second harmonic. Hence, the dynamics causing the 360 degree phase loss interact with the dynamics near 170 Hz, thereby greatly reducing the transfer function measurability and linear system compatibility. Addition of the backing plate greatly improves the transfer function coherence to 1 kHz, hence this modified configuration will be used in all subsequent investigations.

A more subtle feature in Figure 3.5 is the significant damping ratio, $\zeta_o = 0.073$, compared to what one might expect from a flexure type suspension, typically 0.005. The electro-magnetic damping characteristics of voice coil actuators are well known and are most likely responsible for the increased damping. A comparison of unforced time histories of the optical cage position with and without the voice coil present is shown in Figure 3.7. The damping increases from 0.0029 to 0.073 when the voice coil

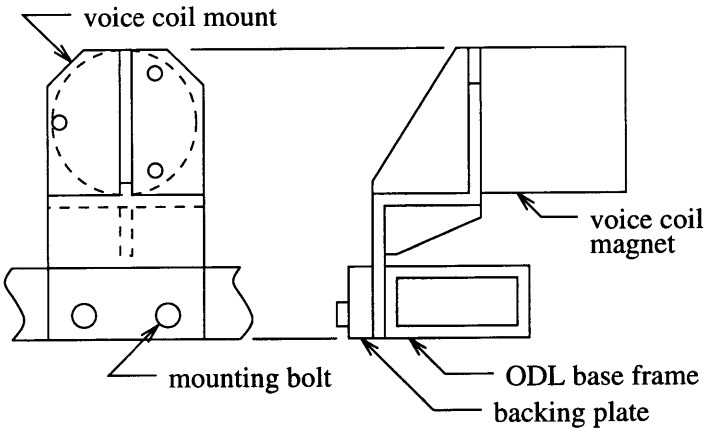

Figure 3.4: Voice coil mount interface detail

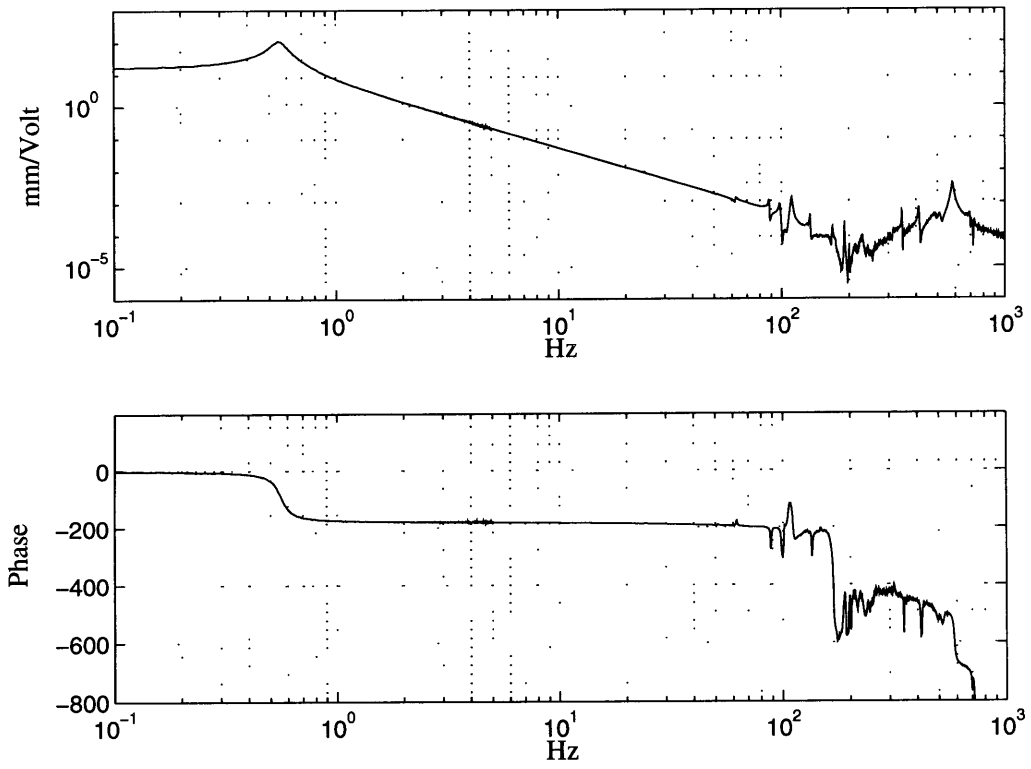

Figure 3.5: Modified voice coil to laser transfer function

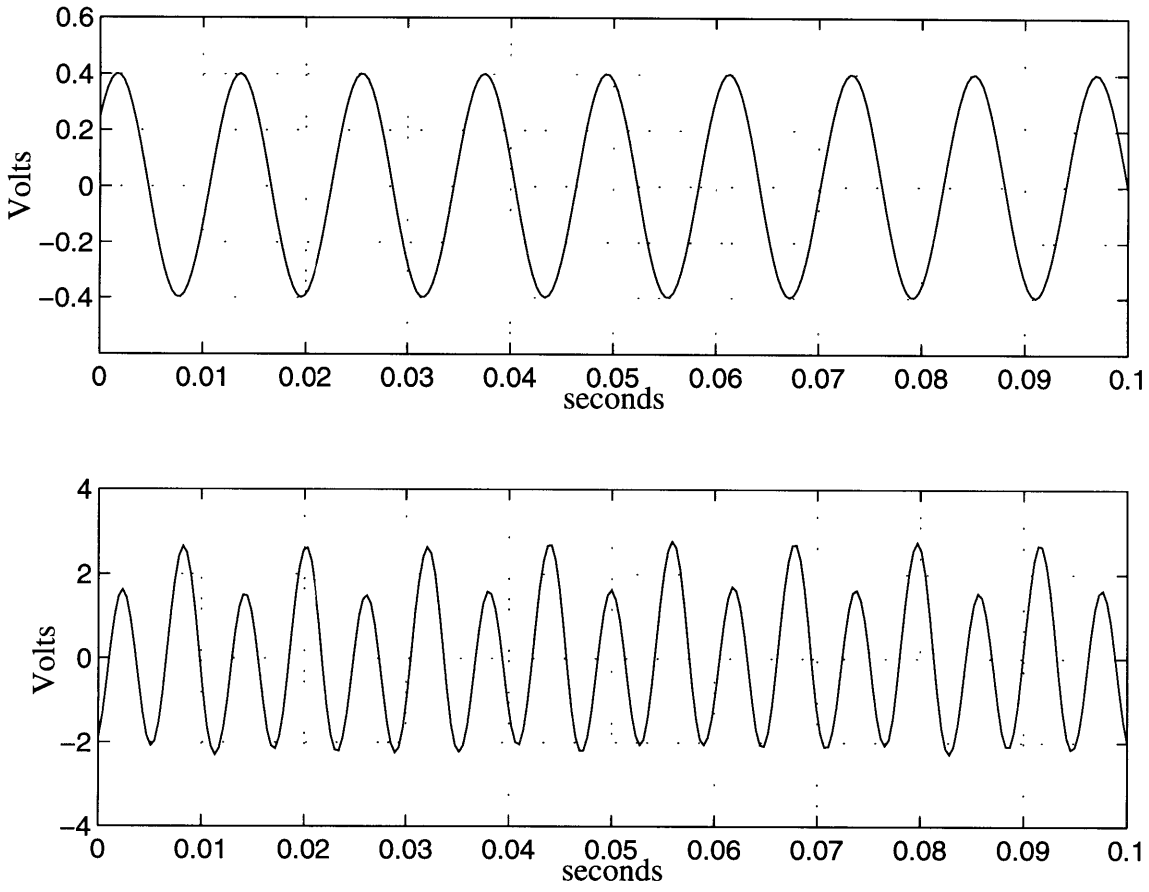

Figure 3.6: Time history of 86 Hz driving force (top) and response (bottom)

magnet is installed. Therefore the damping is associated with the voice coil. Another characteristic difference is the reduction in suspension frequency, ω_o, from 0.67 Hz to 0.56 Hz. This change in ω_o is due to the magnetic interaction between the voice coil magnet and the ferromagnetic materials, Invar and steel, on the optical cage. Since such forces are generally proportional to $1/r^2$, a shift in the natural frequency is not suprising. In addition, some degree of non-linearity may be present. Figure 3.8 shows the directly measured restoring force of the suspension with and without the voice coil installed. As seen in the figure, the magnetic forces are linear over the operating range. In addition, a strong static magnetic force is present and must be compensated by the voice coil. As with the pendulum effect, the magnetic force destiffens the suspension. In contrast to the pendulum effect, the magnetic effects do not vanish in a micro-gravity environment.

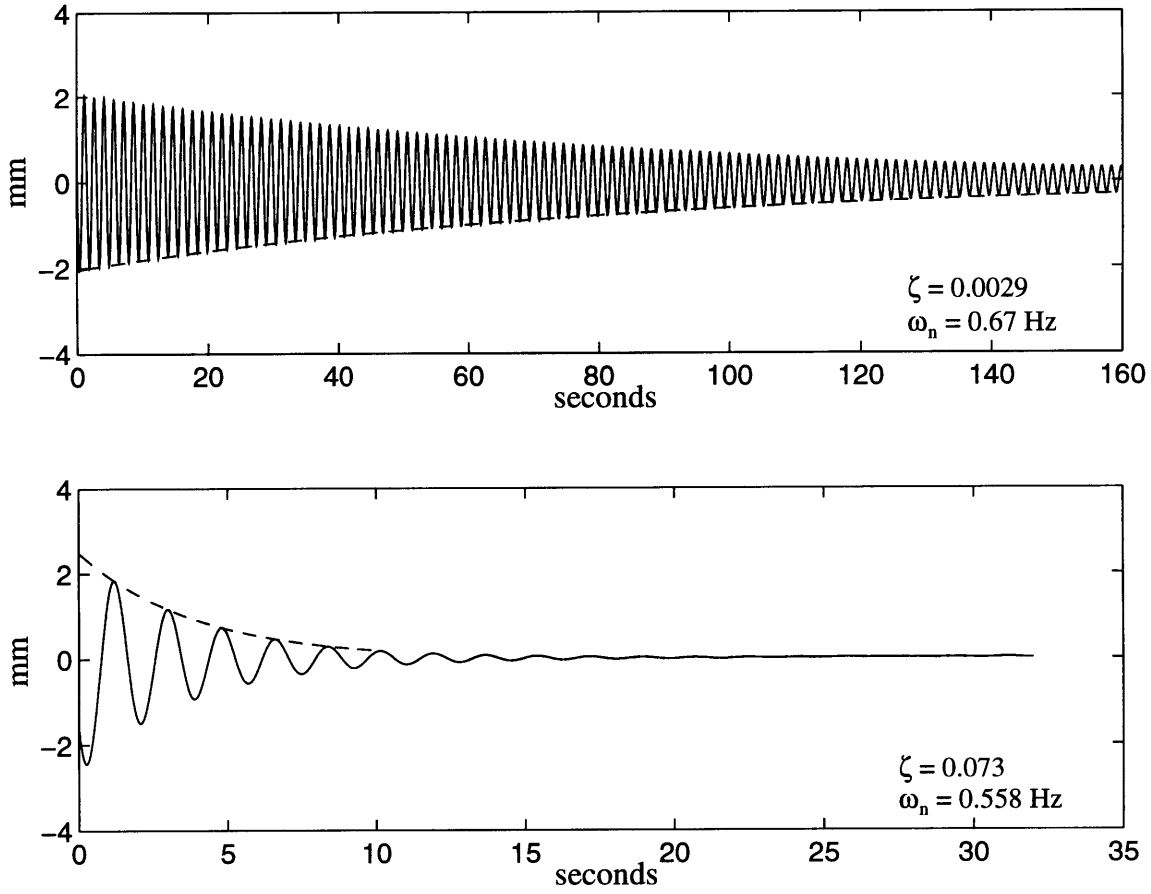

Figure 3.7: Optical cage position time history from an initial displacement with the voice coil magnet removed (top) and installed (bottom)

The first several modes of the voice coil transfer funtion are identified in Table 3.1. The 360 degree phase loss, due to the combination of a complex pole and a complex non-minimum phase zero, near 170 Hz still poses a local control hindrance. The multiple 360 degree phase losses after 600 Hz pose an absolute limitation on the voice coil stage performance. The strong presence of corner cube mount modes and other dynamics foreshadow hazards which will exist on a kinematic structure such as the SITE precision optics bench. Three methods to overcome these dynamics in order to extend the voice coil bandwidth are explained below:

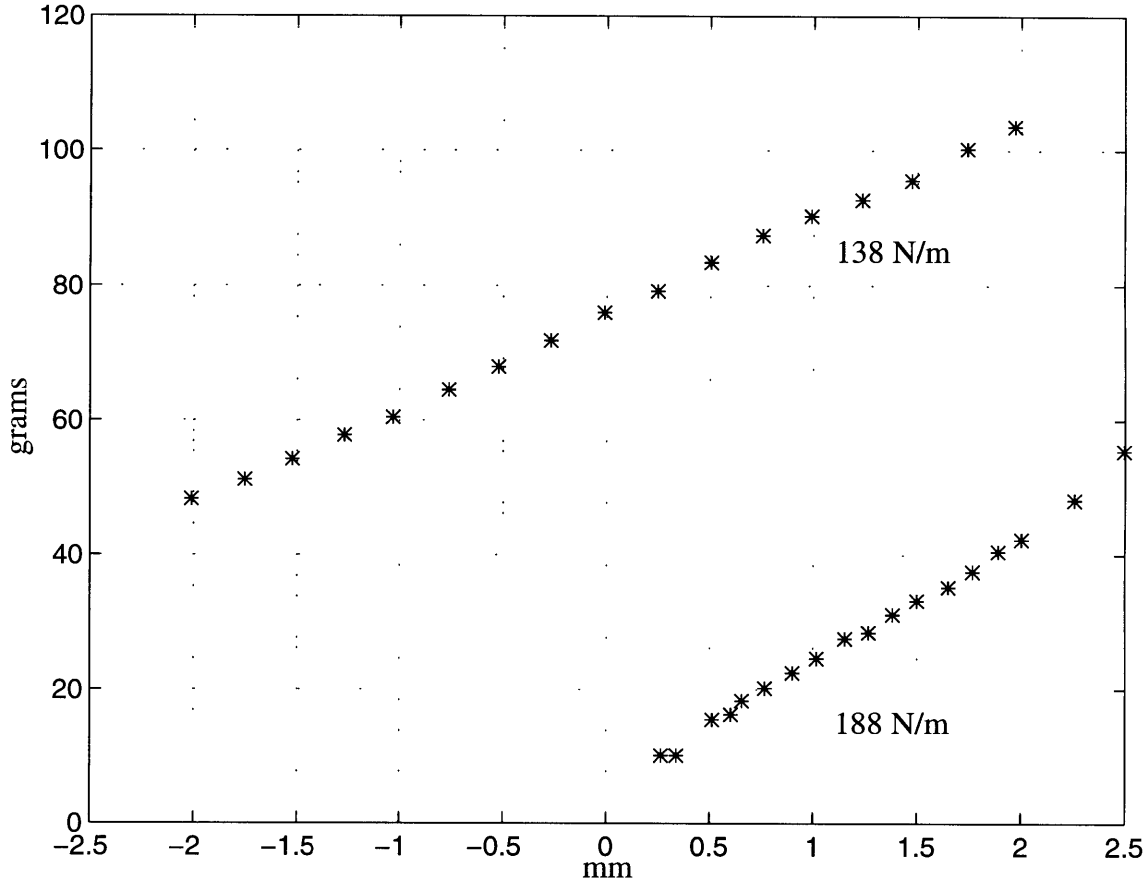

Figure 3.8: Measured suspension restoring force of 138 N/m with and 188 N/m without the voice coil installed

(1) *Decouple dynamics* - decouple the voice coil stage dynamics by introducing a back-to-back voice coil and throw mass as previously done for the PZT. This method may be prohibative in space-based applications due to additional mass and power requirements. Near collocation of two active ODLs will provide some degree of global reactuation, but cannot influence internal ODL modes.

(2) *Local control* - compensate the voice coil transfer function dynamics directly. Need to develop compensators which are robustly stable. Several such synthesis methods are available including sensitivity weighted LQG, multiple model, and Popov controller synthesis [12] [17].

Table 3.1: Modified JPL Phase B voice coil to laser modes

Hz	mode	Hz	mode
0.56	suspension	200	base frame
62	optical cage	212	
85	cc #1	228	cc #1
98	voice coil mount	244	base frame
110	cc #1	300	
133	cc #1	316	
168	cc #2	346	parabolic mirror
175	base frame	413	voice coil mount
192	base frame		

(3) *Global control* - utilize more actuators to attenuate the voice coil induced vibrations throughout the host structure or to directly control the OPD. This solution is a fundamental change in the philosophy of how to control the OPD and should only be implemented if the first two methods are inadequate.

Direct reactuation of the voice coil stage is not investigated, however results may be inferred from examining reactuation of the PZT stack. The transfer function from PZT actuation to laser measurement is shown in Figures 3.9 and 3.10 without and with local PZT reactuation. Both transfer functions are relatively uninteresting except to note the phase loss consistent with the laser sampling rate and the presence of two modes, one at 570 Hz and the other at 740 Hz, in the unreactuated case. Overall, the benefit of PZT reactuation is not significant since the dynamics within the bandwidth of interest, 1 kHz, are simple and easily compensated. Hence, PZT reactuation must be considered from a more qualitative perspective. In general, the program level cost of PZT reactuation is insignificant. The result is a cleaner dynamic response, which may benefit measurement of the central interference fringe. Since the voice coil stage dynamics are much more complicated than the PZT dynamics, reactuation is

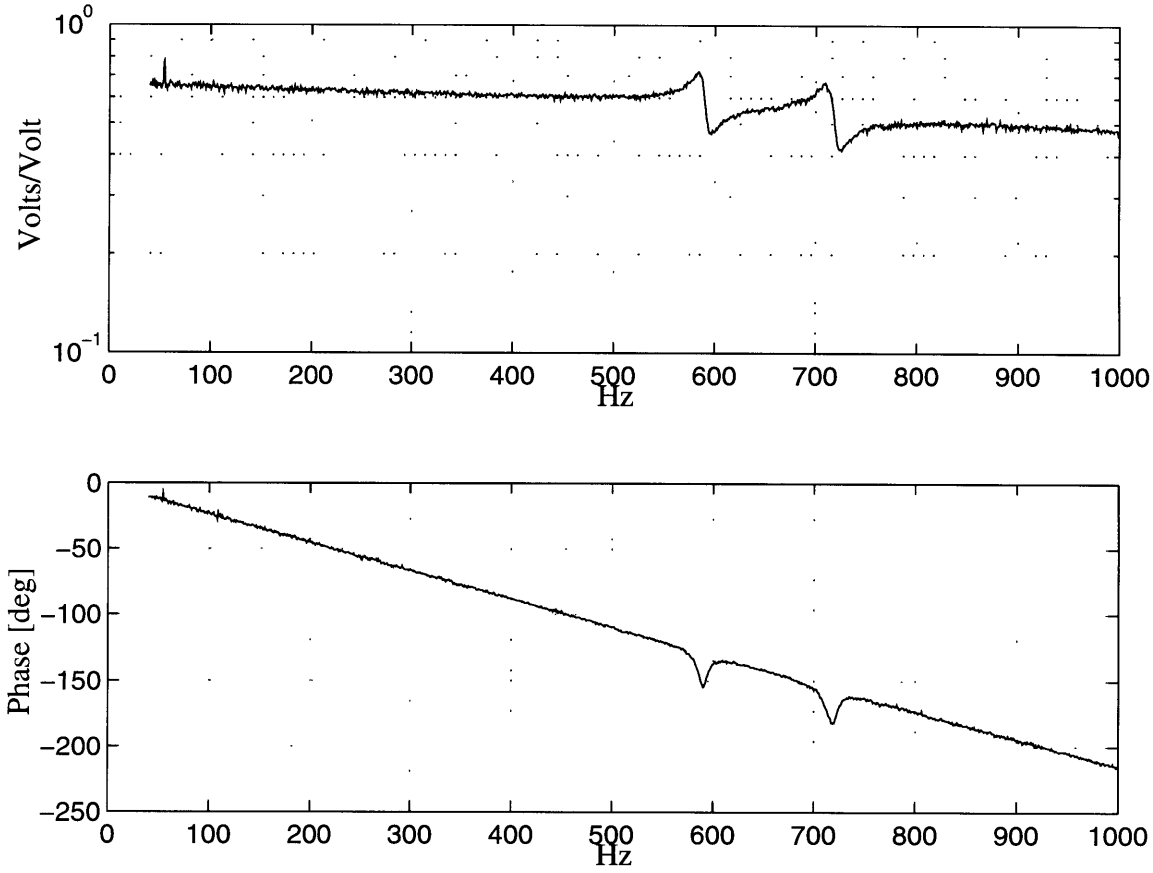

Figure 3.9: Transfer function from PZT to laser without reactuation

much more profound. Local reactuation of the voice coil at the voice coil mount will significantly decrease the exitation of external optical elements. Doing so will reduce the size and increase the stability margins of the corresponding compensator. The cost is additional mass and power.

As opposed to incurring the additional cost and power of reactuating the voice coil stage, the next section examines the cost of local control of the ODL. The cost and performance of local control are evaluated by designing successively higher bandwidth controllers. The cost is evaluated in terms of required hardware and stability robustness, whereas the performance is measured by the loop gain and maximum sensitivity. Note that the local control performance metrics are different from the ODL design evaluation metric, which is the OPD. The terminology *controller performance*

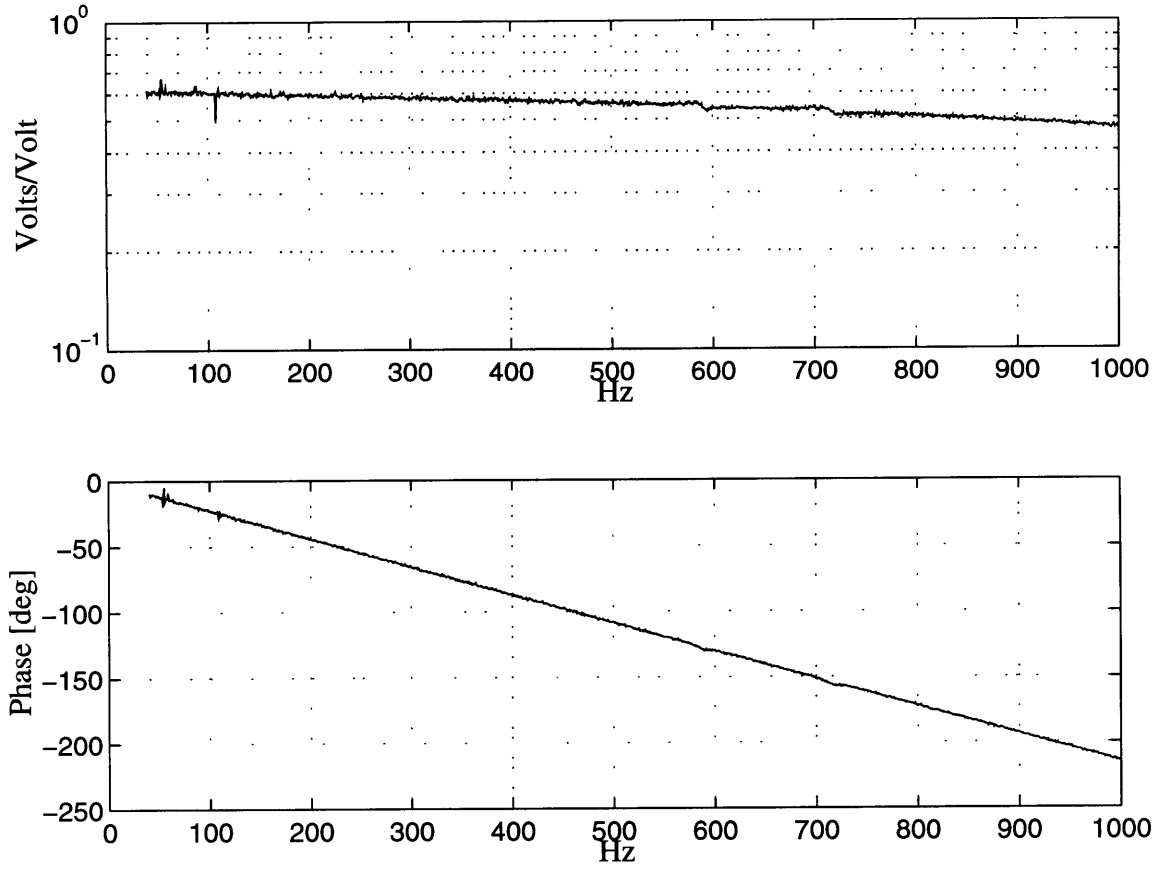

Figure 3.10: Transfer function from PZT to laser with reactuation

metrics is utilized in the following local control discussion to reference the controller design evaluation metrics, whereas *ODL performance metric* references the OPD. The contributions to the controller cost are detailed as follows:

(1) *actuation intensity* $[\rho]$ - measure of the size, which is proportional to $\sqrt{\rho}$, of the actuator required to perform the compensation task. Decreasing ρ corresponds to increasing actuation intensity.

(2) *sensor noise intensity* $[\theta]$ - measure of the sensor quality, which is proportional to $\sqrt{\theta}$, required to perform the compensation task. Decreasing θ corresponds to decreasing sensor noise intensity.

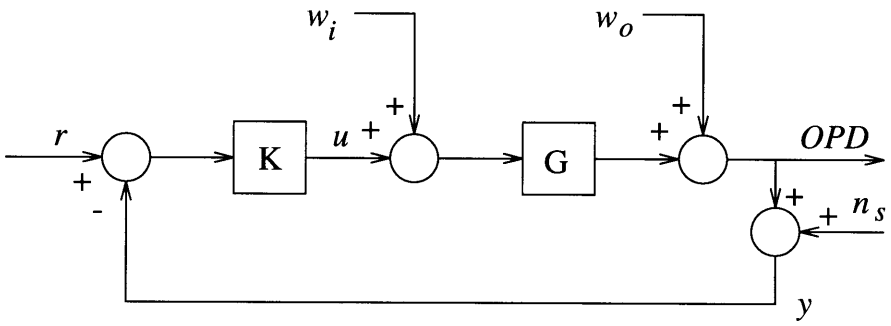

Figure 3.11: Control topology for JPL Phase B ODL control designs

(3) *compensator size* $[n_{st}]$ - the number of compensator states. Generally, the smaller the compensator, the faster the sampling time and, hence, shorter the time delay.

(4) *bandwidth* $[BW]$ - measure of the frequency range of dynamics with which the device will interact. Generally, a ratio of the bandwidth to the first loop crossover, ω_c, near unity is desirable. A high ratio indicates that the device only controls a small portion of the frequency range with which it interacts.

(5) *gain margin* $[\gamma]$ - a stability robustness metric. Increasing gain margin corresponds to increasing robustness to loop gain errors.

(6) *phase margin* $[\phi]$ - a stability robustness metric. Increasing phase margin corresponds to increasing robustness to loop time delay errors.

Similarly, the contributions to the controller performance metric are:

(1) *loop crossover* $[\omega_c]$ - the first loop crossover frequency measures the frequency range out to which the ODL is effective.

(2) *loop gain* $[T_{.10}]$ - the loop gain, measured by the gain at 0.10 Hz for the JPL Phase B ODL, is a measure of the effectiveness of the ODL.

(3) *maximum sensitivity* $[S_{max}]$ - measures the maximum amplification of the optical disturbance through the ODL.

All controllers are single input, single output (SISO) for a voice coil force input, u, and laser metrology displacement output, y, as shown in Figure 3.11. Since the laser output, y directly measures the ODL design performance metric, *OPD*, the

problem is considered *output degenerate*. This means that shaping the disturbance, w, to measurement, y, transfer function is the same as shaping the disturbance, w, to performance, z, transfer function as defined by the contracted problem statement in equation (3.1). Since the problem mathematics have been detailed several times throughout Chapter 2, they will not be repeated.

$$\begin{bmatrix} \dot{\xi} \\ z \\ y \end{bmatrix} = \begin{bmatrix} A & B_w & B_u \\ C_z & D_{zw} & D_{zu} \\ C_y & D_{yw} & D_{yu} \end{bmatrix} \begin{bmatrix} \xi \\ w \\ u \end{bmatrix} \tag{3.1}$$

A time delay consistent with 3 kHz sampling is built into the measured voice coil stage dynamics. In actuality, the sampling rate is inversely proportional to compensator size. Hence, smaller compensators may be implemented at higher sampling rates, thereby reducing the resulting time delay and corresponding phase roll-off. These differences in the time delay, however, are neglected in the subsequent studies.

The plant dynamics are represented by a 48 state model based upon the transfer function in Figure 3.5. Since the design of a controller is very specific to the plant dyamics, the meaning of frequency weight details which desirably shape the loop transmission loses generality. Hence, frequency weights will not be utilized in the following control designs. Therefore, the sensor noise intensity, θ, and actuation intensity, ρ, are the only design variables. This permits a fair evaluation of the impacts of sensor quality and actuator size on the controller performance. It also provides a more clear identification of how different limiting factors enter the problem. Such clarity may become lost once loop shaping techniques are invoked. Therefore, the objective of the control designs is not to design the *best* compensator, but rather to identify performance limitations and evaluate design trade-offs.

Since the only design variables are the actuator size and sensor quality, their incremental effects on the system performance are evaluated. First, the actuation intensity is fixed while the sensor noise intensity is varied. Then sensor noise intensity is fixed while actuation intensity is varied. The LQG controllers are synthesized using the full 48 state plant model. Afterwards, the controllers are reduced using a

balanced reduction method [19]. In all cases, the system evaluation is performed by implementing the control design on the open-loop transfer function test data.

The controller reductions were performed until the crossover frequency noticably shifted or the maximum sensitivity exceeded 10 dB. Controller reductions based entirely upon modal cost values [20] were found to be inadequate. Roughly, this type of reduction process eliminates compensator states based upon their contribution to the norm of the full-order compensator. Hence, states which form the basic *backbone* of the compensator are kept, whereas those which produce small peaks and valleys on the backbone are eliminated. Such reduction criteria, by themselves, were found to be poor for compensators which have crossover frequencies in the vicinity of high plant modal density. In such cases, retaining the states which contribute to the peaks and valleys, however small, is very important. Preserving the frequency and magnitude content local to the crossover regions was found essential to maintaining stability margins and sensitivity magnitudes. In order to keep states which only contribute locally to crossover regions as well as retain those which significantly contribute to the overall compensator shape, a hybrid reduction process was used. This was performed by placing the compensator in a tri-diagonal real modal form such that the states correspond to the individual modes of the compensator. Then, a trial-and-error process was implemented in which states were eliminated based upon both modal cost values and their proximity to gain and phase critical regions. All stated were eliminated using a balanced reduction procedure.

The impact of sensor noise intensity on the system performance is shown in Table 3.2 with a few corresponding loop transmissions shown in Figure 3.12. As expected, as the first crossover frequency increases, correspondingly more states are required to compensate the rich modal density of the plant, which occurs above 60 Hz. The bandwidth, however, exhibits a significant jump for all compensators which have a crossover frequency above 40 Hz. Examining Figure 3.12, this increase in bandwidth is due to a dominant peak at 570 Hz exceeding unity gain. Hence, another gain and phase critical region appears. Also, stability margins are further comprimised by the multitude of dynamics, and hence phase fluctuations, within the crossover regions.

Hence, in addition to the jump in bandwidth, a significant reduction in gain and phase margins occurs. Correspondingly, the maximum sensitivity also increases.

For the high quality sensors, $log_{10}\theta \leq -8$, LQG utilizes an unstable complex mode near 170 Hz to compensate for the 360 degree phase loss near that frequency. The increasing benefits of a better sensor quickly taper above a 100 Hz crossover frequency. This is due to having a mismatched ability in being able to measure the system and an ability to use that information. In other words, the actuator size needs to be increased in order to use the sensor information to its fullest extent. Considering that optical delay lines are staged devices and that the bandwidth of the voice coil stage exhibits a jump to 600 Hz, further extending the first crossover frequency is not considered beneficial. The slight gains which would be attained from such an increase are weighted against the implications of introducing stronger interactions with the PZT stage and reducing stability margins. In addition, actuator noise floor issues, as discussed in Chapter 2, become more pronounced.

The benefits and costs of increasing actuator zize are shown in Table 3.3 with a few corresponding loop transmissions shown in Figure 3.13. The trends and driving influences are the same as for increasing the sensor quality except that none of the compensators are unstable. This is due to the sensor not being good enough to estimate the system dynamics in the presence of the 360 degree phase loss near 170 Hz. Hence, as the sensor gains were ultimately limited by needing a compatible actuator, the actuator gains are limited by the need for a compatible sensor.

Overall, the first crossover frequency of the voice coil stage of the JPL Phase B ODL should be limited to 100 Hz for the following reasons:

(1) The second dynamic peak at 570 Hz results in simultaneous loop gain in excess of unity for $100 \leq \omega \leq 600$ Hz. The presence of the high modal density in this simultaneous *jump* will require orders of magnitude in sensor quality and actuator resolution (not size) to assure adequate gain and phase stability margins. Even if such margings could be maintained, loop sensitivity would be compromised.

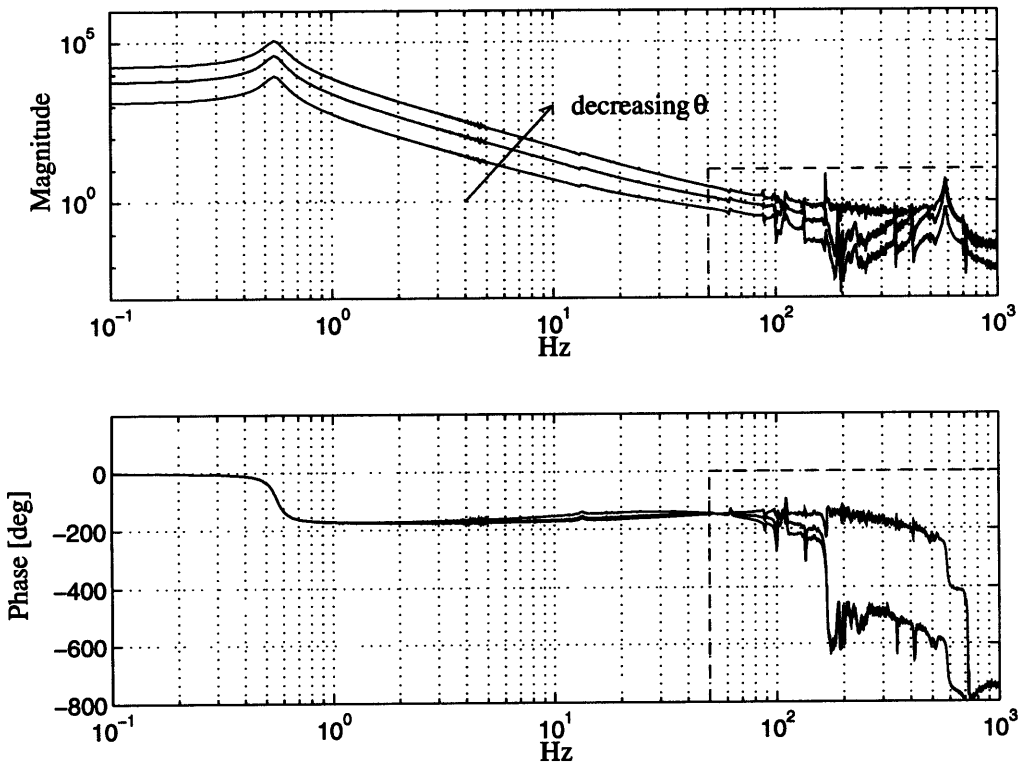

Figure 3.12: Loop transmission for $log_{10}\rho = -6$ and $\log_{10}\theta$ =–3, –6 and –10

(2) A standard 12-bit actuator noise floor may be incompatible with further increases in loop gain. The ODL actuators are staged because one actuator is incapable of providing the necessary dynamic range and bandwidth.

(3) The PZT is a good actuator out to 1 kHz and the dynamic disturbances in its range ($\omega > 10$ Hz) are generally small.

Table 3.2: Comparison of LQG controllers ($log_{10}\rho = -6$) versus sensor noise intensity on the JPL Phase B ODL

ID	$log_{10}\theta$	n_{st}^1	ω_c^2 [Hz]	BW^3 [HZ]	γ^4 [dB]	ϕ^5 [deg]	$T_{.10}^6$ [dB]	S_{max} [dB]
Q3	-3	8	20	35	14	48	55	2.8
Q4	-4	8	31	68	9.4	41	63	4.6
Q5	-5	10	46	579	4.9	17	70	7.5
Q6	-6	14	60	587	3.2	24	75	10
Q7	-7	28	80	596	4.4	20	80	10
Q8[8]	-8	44	94	595	4.2	18	83	11
Q10[8]	-10	46	101	593	3.2	18	85	10
Q14[8]	-14	46	101	593	1.8	18	85	10

[1] number of compensator states

[2] first loop crossover frequency

[3] bandwidth defined by last -3 dB point

[4] critical gain margin (upward in all cases)

[5] critical phase margin

[6] loop gain at 0.10 Hz

[7] maximum closed-loop sensitivity

[8] unstable compensator

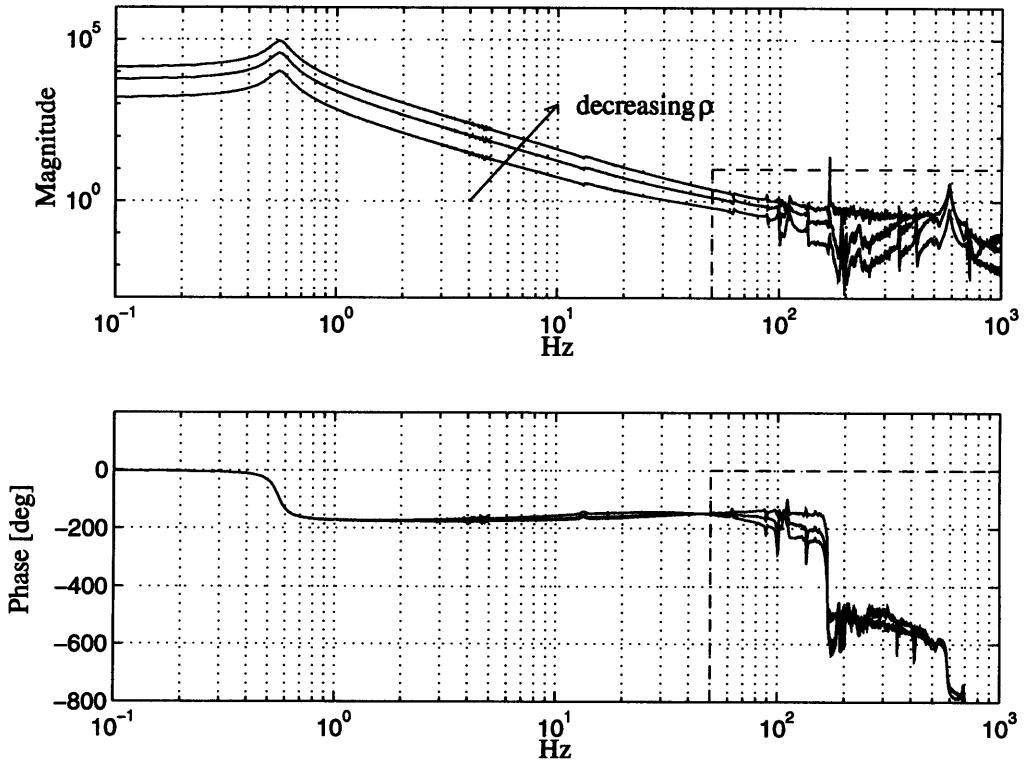

Figure 3.13: Loop transmission for $log_{10}\theta = -6$ and $\log_{10}\rho$ =–4, –6 and –10

Table 3.3: Comparison of LQG controllers ($log_{10}\theta = -6$) versus actuation intensity on the JPL Phase B ODL

ID	$log_{10}\rho$	n_{st}^{1}	ω_c^{2} [Hz]	BW^{3} [HZ]	γ^{4} [dB]	ϕ^{5} [deg]	$T_{.10}^{6}$ [dB]	S_{max} [dB]
R4	-4	8	34	73	8.6	36	64	5.7
R5	-5	10	48	580	4.7	15	70	7.8
R6	-6	14	60	587	3.2	24	75	10
R7	-7	30	76	598	4.6	25	79	8.8
R8	-8	44	90	590	4.7	25	81	9.6
R10	-10	48	101	590	4.3	23	83	8.6
R12	-12	48	101	590	4.2	24	83	8.5

[1] number of compensator states

[2] first loop crossover frequency

[3] bandwidth defined by last -3 dB point

[4] critical gain margin (upward in all cases)

[5] critical phase margin

[6] loop gain at 0.10 Hz

[7] maximum closed-loop sensitivity

Chapter 4

General Optical and Mechanical Design Issues

Chapters 2 and 3 present important analytical and experimental results which provide insight to the design of a high performance optical delay lines. To more completely address the development of optical delay lines, this chapter provides a cursory look at other issues including general optical and mechanical design.

4.1 Optical Design Issues

The optical design of the ODL is at least as important as the mechanical design. This section is intended to highlight some of the fundamental equations, trade-offs and design constraints associated with the optical design. One should pursue the work done at JPL by Colavita [5] [15] for a more rigorous examination.

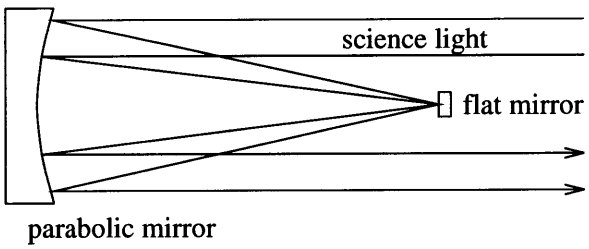

Figure 4.1: Cat's eye optical configuration

The fundamental optical layout is a cat's eye retroreflector shown in Figure 4.1. The science light and laser metrology beam ideally enter the device parallel to its priciple axis, focus to a point on the flat secondary mirror, expand and recollimate on the primary mirror, and exit parallel to the device axis. Physical propagation delays are introduced into the optical path by moving the entire optical cage, the structure which supports the cat's eye, relative to the other optical elements in the interferometer or by displacing the secondary flat mirror relative to the primary one. These displacements result in optical pathlength changes which are twice device position changes. Since the laser metrology beam passes through the optical delay line multiple times, the resolution of the laser metrology system may be increased by a factor of two with each pass.

Examination of the relationships among optical and physical design parameters associated with the ODL reveals that the parabolic mirror f# and diameter ,D, determine most other parameters to first order. The quality of the device, on the other hand, is determined by the required optical wavefront distortion, λ/n, of the science light, of wavelength λ. For interferometer applications, $n \geq 20$ is usually required. The diameter of the parabolic mirror is set by the diameter of the science light which passes through the system.

Once the fidelity of the device is determined through more global interferometer system performance studies, the science light fringe visibility degradation due to the optical pathlength difference can be approximated by

$$\Delta V = exp\left[-\frac{1}{2}(2\pi\sigma_{OPD})^2\right] \tag{4.1}$$

where σ_{OPD} represents the RMS pathlength fluctuations of the science light in waves. Given the science light wavelength, λ, and the ODL $f\#$, the depth of focus (dof), defined as the maximum tolerable position error of the flat secondary mirror relative to the cat's eye focal point, resulting in a 5% reduction in the science light's central fringe visibility is approximated by equation (4.2). Essentially, the dof specifies the maximum stroke of the PZT actuator which controls the motion of the secondary mirror.

$$dof = \pm\lambda f\#^2 \tag{4.2}$$

The selection of the optical $f\#$ is made in consideration of geometrical and mass constraints, cost and other system level issues. Since the primary mirror diameter is independently established by the science light diameter , selection of the $f\#$ prescribes the physical ODL length. The additional choice of materials then provides the thermal expansion sensitivity. Since the $f\#$ provides the device length scale, it strongly influences device modal characteristics and actuator force requirements. Given a fixed optical diameter, the net mass of the optical cage is approximately a linear model versus device length, or $f\#$. Additional considerations of $f\#$ are that increasing $f\#$ corresponds to decreasing cost and increasing field of view. Hence, the $f\#$ is one of the most critical parameters in ODL design. The $f\#$ selected for the joint MIT-JPL SITE project ODL is 5.

Static internal alignment of the ODL is an important issue which must be considered when performing detailed mechanical design. One of the most important static alignment issues is that of thermal stability. For a maximum 5% reduction in visibility due to an ODL which has a 80 millimeter diameter, $f\#$ of 5, and science light diameter of 25 millimeters, the depth of focus is $\pm 12\mu$m. Given mean thermal expansion coefficients of aluminum and stainless steel as $13\mu\epsilon/^oF$ and $6\mu\epsilon/^oF$, respectively, small temperature changes quickly defocus the device. Typically, this problem is alleviated by using near zero CTE materials, such as Invar and Super Invar, as metering rods between the primary and secondary mirrors. Such compensation, however, is only adequate for $\pm 50^oC$ temperature variations from room temperature. Outside this range, the thermal expansion characteristics of Invar significantly drift from nominal. For ground based systems and laboratory environments, these specialized materials are sufficient. For more extreme thermal conditions, additional measures must be taken. For contained environment operation, active heaters and insulation may be used to control the thermal environment within acceptable tolerances but may require significant additional mass and power requirements which may be intolerable in space-based systems.

4.2 Mechanical Design Issues

Chapters 2 and 3 analytically and experimentally investigated several structural design issues from a linear time invariant perspective. In real systems, however, non-linearities are present and may limit system performance or place additional constraints on ODL design and operation. Several sources of non-linear behavior which exist in real optical delay lines are discussed. Since the optical cage suspension is one of the more critical aspects of the ODL design problem, this section also examines that component in more qualitative detail and presents an alternate suspension configuration. Finally, the severe disturbance environment during the launch phase of a space-based system is briefly discussed to envoke an awareness of design issues which are not present in ground-based systems.

When using voice coil actuators, one is generally aware of their electro-mechanical damping properties. A phenomenon which is more subtle is that of ferromagnetic interactions between the voice coil magnet and the actuated structure. For small displacements, this is a valid neglection. In the cases of high displacement and high performance, this may no longer be true. In optical delay lines, Invar is used for its thermal expansion characteristics. Unfortunately, Invar is highly ferromagnetic as are many flexure materials, such as the 300 series austentitic steels, and standard fasteners. As discussed in Chapter 3, this magnetic effect is sufficiently linear over the range of operation for the JPL Phase B ODL. This effect must be evaluated for each ODL design and may pose a contraint on maximum voice coil displacement so as to maintain a certain degree of force linearity.

The inverted pendulum suspension of the Mark III and JPL Phase B optical delay lines is well proven in ground-based operations, however, it invokes a certain level of uncertainty when performance is extrapolated to a micro-gravity environment. Such uncertainty is due to the removal of the destiffening pendulum effect. An alternative suspension method is to utilize axial flexures, similar to one shown in Figure 4.2, at both ends of the optical cage. Under short stroke limitations, the flexures retain linear behavior and permit only axial deflections as compared to the vertical translation

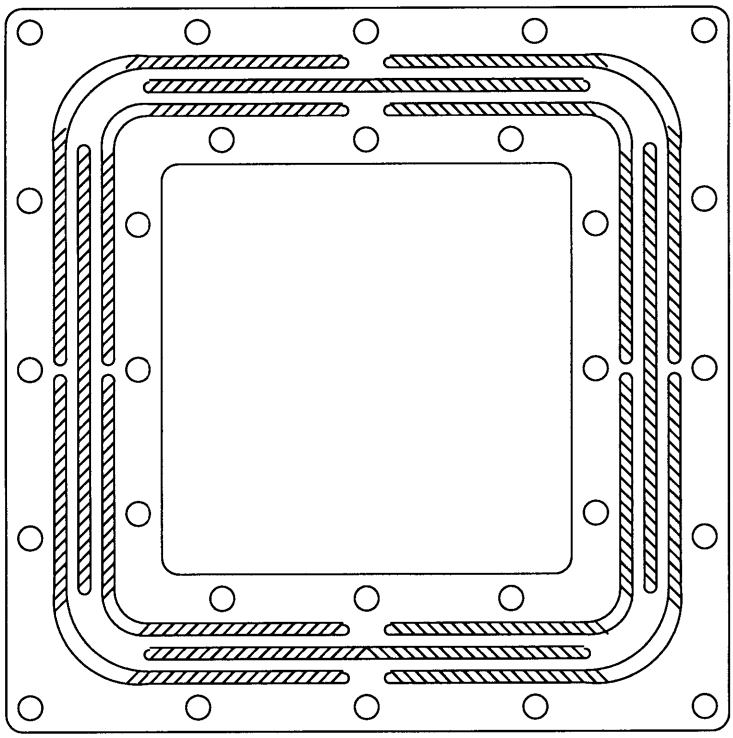

Figure 4.2: Axial flexure detail

present in a pendulum suspension. Axial flexures provide an ambiguous axial orientation with respect to gravity, therefore the ground-based and space-based suspension characteristics are nearly identical. Hence, uncertainty in suspension frequency is eliminated, however, other issues arise.

Table 4.1 provides a comparison of the axial and pendulum suspension configurations. Since the pendulum suspension is traceable to previous optical delay lines, the risk in such a design is low. Axial flexures may not be traceable to ODL applications, but they have been developed for use in other systems, such as mechanical shakers and active struts [21], which require axial motion. For space-based usage, however, issues of axial flexure *snap-through* and *lateral stability* pose additional risk to proper ODL function. These risks may be mitigated to acceptable levels by extensive environmental testing.

Snap-through is defined as a local flexure instability which is characterized by the inability to stabily maintain a zero deflection state. Instead of being stable at zero deflection, the flexure has two stable positions, one at each side of the zero deflection

position. Motion through the region between the two stable positions is characterized by a *snap-through* type motion due to local compression of the flexure details. This compression may be a result of either manufacturing defects or thermal expansion. Environmentenal testing at various temperatures is required to verify the existance or absence of axial flexure *snap-through.*

Axial flexure *lateral stability* is defined as local buckling of the flexure due to transverse loading. During normal space-based operation, this is not an issue since lateral loads are small. During launch of a space-based system, however, these loads may be quite large, but may be mitigated by an additional lock-down mechanism. *Lateral stability* is an issue in ground-based systems due to gravity loading. Alleviation of flexure buckling in ground-based systems may be achieved through flexure design.

Beyond the stability issues, axial flexures are superior to the pendulum suspension in mechanical simplicity. In addition, the axial flexure provides for true axial motion, whereas the pendulum suspension action is a combined axial and transverse displacement. Axial flexures also provide for the ability to easily stack flexures, thereby permitting efficient variation of the suspension characteristics during evaluation and testing processes. Furthermore, several axial flexures of the same design may be manufactured simultaneously, thereby reducing manufacturing costs. The basic trade-offs between the axial flexure and inverted pendulum suspension configurations are mechanical simplicity versus design traceability and flexure stability mitigation versus suspension frequency uncertainty.

For space-based applications, launch load integrity enters as a significant design requirement. For the ODL to be able to survive the launch phase of a mission, additional attention must be paid to acoustic fatigue and device lock-down requirements. Since the ODL has one operational degree-of-freedom which is unconstrained, some form of launch latch, and possibly relatch, mechanism must be incorporated into the design. A less obvious consideration is that the optical cage support flexure may not be able to withstand the internal shear loads encountered during launch and, therefore, must also be provided additional luanch phase support. Even more obscure are the poor fatigue charachteristics of PZT stacks which require a mechanical preload

Table 4.1: Comparison of suspension configurations

Issue	Pendulum	Axial
traceability	ODL	isolation
action	axial + shear	axial
linearity	short stroke	short stroke
Δ to micro-g	shift in ω_o	no effect
complexity	moderate	low
stability	good	snap-through and lateral instability

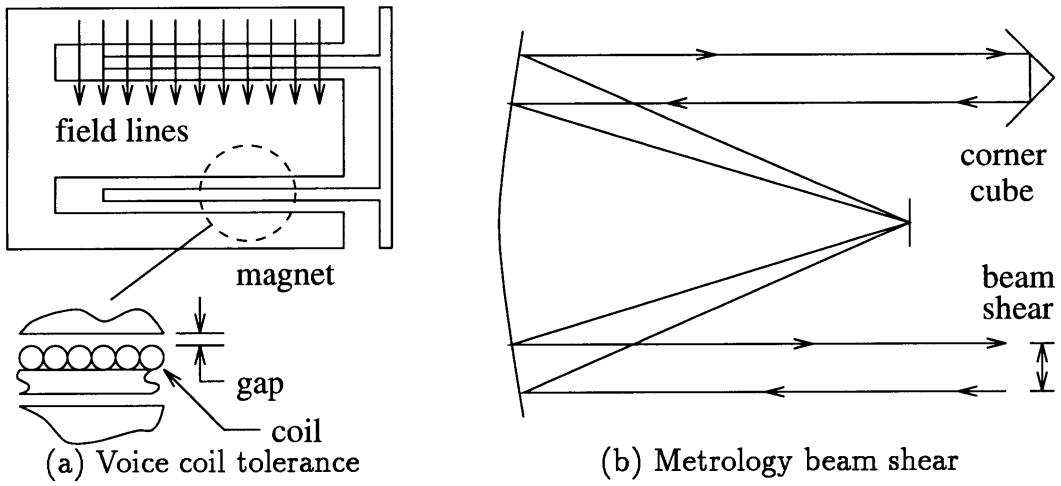

(a) Voice coil tolerance (b) Metrology beam shear

Figure 4.3: Constraints on optical cage shear deflection

to survive launch.

As with launch considerations, other design constraints may exist which are independent of the performance requirements. One issue arises from the action of the inverted pendulum optical cage support. Due to the action, a vertical shear translation of the optical cage is associated with the desired axial motion. This shear motion is constrained in magnitude by two principal factors. First, to obtain an efficient magnetic field for the voice coil actuator, a tight tolerance between the magnetic core and coil, shown in Figure 4.3(a), is desirable. This physical gap limits the acceptable magnitude of shear translation.

Second, as shown in Figure 4.3(b), vertical translation of the optical elements results in a two-fold translation of the science light and, more importantly, a four-fold translation in the laser metrology beam since the metrology beam passes through the ODL twice. Proper function of the metrology system detector requires a prescribed amount of beam overlap. A typical 6 mm diameter laser beam and a 95% radial beam overlap requirement translate to an acceptable optical cage shear translation of 100μm. This shear displacement limit imposes a contraint on the relation between the suspension length scale and maximum voice coil displacement.

The aforementioned mechanical design issues are by no means a complete listing of mechanical considerations as several of the issues are design specific. The number and importance of these issues, however, are intended to promote an awareness of additional limitations and constraints which result from mechanical design.

Chapter 5

Summary and Conclusions

The role of space-based interferometry in achieving astronomical goals of the 21st century is well understood. It is also understood that an infusion of advanced technology beyond that used in ground-based systems is required due to the increased flexibility in space-based platforms. Optical delay lines are active optical components which are utilized to control the optical pathlength difference between two beams of science light down to the nanometer level so that the central interference fringe of the science light may be acquired and measured. In order to perform this task in a space-based system, ODLs in space-based interferometers are necessarily high performance devices. Therefore, ODL design must be performed within a combined control-structure framework in order to maximize its performance and minimize associated mass and power costs. To these ends, this work pursues ODL structural design and control from both analytical and experimental perspectives. The objective of this work is not to produce *optimum* structural designs, but to create *good* designs knowing that control will be implemented in order to achieve the overall performance goals.

In order to evaluate incremental performance and cost of ODL design permeatations, knowledge of both structure and controller characteristics is required. Due to the iterative nature of the design process, Linear Quadratic Gaussian (LQG) controller design is considered an efficient method with which to synthesize compatible and representative controllers while enforcing a certain amount of optimization. LQG also

permits direct inclusion of the disturbance spectrum, thereby providing additional performance gains when the disturbance environment is well characterized. As with the structural design, the objective of the control design is to produce *good* controllers which are compatible with the structure.

The control-structure design process was utilized to investigate the influence of the optical cage suspension frequency to reject simplified narrowband and broadband optical disturbances. In the case of low authority narrowband disturbance rejection, choosing the optical cage suspension frequency to coincide with the optical disturbance frequency exibited significant reductions in control cost to reject the disturbance. Effectively, this choice in suspension frequency utilizes the high contol authority local to the vicinity of the flexible modes of lightly damped structures. When high authority disturbance rejection is required, as is the case for space-based optical delay lines, such reductions in control cost vanish. In the case of broadband disturbances, the disturbance energy is spread out over a much wider frequency range than in the narrowband case. Since heightened control authority in lightly damped structures is only present in the vicinity of the flexible modes, the increased control authority is only effective over a fraction of the total disturbance. Therefore, no significant reductions in control cost through selection of the suspension frequency exist for bradband disturbances. In both cases, examination of the disturbance only identifies an upper bound on *good* suspension frequencies. This upper bound exists due to the tradeoff between control effort being exrted to control the system inertia and effert to overcome the suspension stiffness. Hence, this upper bound is also a function of the level of control authority.

The notion and limitations of sensor noise are well understood, however the same is not true for actuators. Optical delay lines consist of three stages which have different, but overlapping, dynamic ranges and bandwidths since no single device is adequate to provide nanometer level resolution over meter long travels and a kiloHertz bandwidth. As with sensors, all real actuators have an inherent level of noise due sources such as background electronic noise and bit level resolution of controller hardware. In the presence of high gain compensators, the small performance peturbations which

result due to the noise may produce measurable control forces. Hence, Chapter 2 extended the high authority optical disturbance rejection problem to include these noise effects. Two main effects were noted. First, since the control cost to reject an optical disturbance is constant below some upper bound on frequency and the magnitude of physical perturbations due to process noise decreases with increasing stiffness, a stiff suspension is better than a soft one. Effectively, these actuation noises determine a lower bound on good suspension frequencies. Second, the puturbation of the performance metric due to the actuation noise places an upperbound on the maximum performance which may be attained. In other words, attainment of more performance requires not only a larger actuator, but also one with a cleaner signal, or less noise. This second effect is the fundamental motivation for actuator staging.

Progression of design studies to a full three stage ODL model illuminated difficulties in posing the problem to obtain viable LQG controllers. Not being told otherwise, LQG assumes that all actuators have infinite bandwidth and infinite dynamic range. Therefore, it uses the cheapest actuator, the PZT in the case of ODLs, to perform the compensation task. This usage, however, is incompatible with the device characteristics. Relaying the neceesary information to LQG requires posing the problem with a good choice of normalized state variables. Absolute position states generally result from representing the system from a Newtonian mechanics perspective. Such states, however, require at least nine significant figures in order to discern nanometer level displacements in the presence of meter level values. To maintain a uniform degree of precision in the problem, the corrdinates should be transformed such that the states are the relative stage displacements. This also provides a means with which to directly penalize relative stage displacements within the LQG problem. To limit device bandwidths, the control penalties must be frequency weighted such that, for example, high frequency use of the lead screw is penalized much more heavily than low frequency use. Such frequency weighted penalties were found to be necessary to obtain acceptable device usage. Unfortunately, such weighting was found to introduce problems of numerical scale within the mathematics. To alleviate these scaling difficulties, the equation states were further normalized to units of percent stage stroke,

actuator force, sensor range and required performance. Such scaling was found to be necessary to obtain viable solutions to the Riccati equations which are solved during LQG controller sysnthesis.

To provide more insight into the ODL problem, the SITE optical delay line requirements were used for an example design problem. First, fundamental performance requirements and constraints were utilized to estimate the device dynamic ranges required to perform the task. Then, the SITE optical disturbance autospectrum was used in a simple model to evaluate an upper bound on good suspension frequencies. The disturbance spectrum magnitude was increased by a factor of three to provide a performance margin. In addition, the sharp spikes in the disturbance autospectrum were reduced in magnituded and broadened to provide some performance robustness to frequency uncertainties in the disturbance. An upper bound of 0.5 Hz on the suspension frequency was determined. Afterwards, a three stage model was used to obtain a single design which would meet the 25 nm RMS OPD performance objective. Frequency weighted control weights were successfully implemented to produce acceptable stage bandwidths of 2.8, 103, and 385 Hz for the lead scre, voice coil, and PZT, respectively. Time domain simulations were then performed to evaluate actuator sizes and relative stage strokes. With the exception of the time during which shuttle attitude control system thrusters were firing, the design was successful in mitigating the OPD.

To augment analytical investigations, the JPL Phase B optical delay line was extensively characterized to identify performance limitations and control costs for a real ODL. The influence of magnetic forces which are present with voice coil type actuators was identified as destiffening the optical cage suspension. Although magnetic forces are generally non-linear, they exhibit linearity over the range of the voice coil stage stroke. Benefits of decoupling internal dynamics was illustrated by reactuating the PZT stage. Such reactuation is deemed more beneficial for the voice coil stage, but the additional mass and power are somewhat prohibitive in a space-based system. LQG control designs were synthesized for the Phase B ODL and implemented on open-loop test data for the voice coil force input to laser measurement output.

The incremental gains of sensor quality and actuator size were evaluated in terms of loop crossover frequency, bandwidth, number of compensator states, gain and phase margins and sensitivity. Due to high frequency dynamics, attaing a loop crossover frequency in excess of 100 Hz is discouraged due to a significant increase in required sensor and actuator capabilities to mitigate numerous flexible modes between 100 Hz and 500 Hz which become gain and phase critical simultaneously. These particular dynamics are both internal to the ODL and due to dynamics elsewhere on the optical bench on which the tests were conducted. Since the disturbances at these frequences tend to be within the dynamic range of the PZT, increasing the control bandwidth of the voice coil stage beyond 100 Hz is not deemed efficient due to decreased stability margins.

During the controller reduction process, basic modal cost analysis was found to be a poor choice for selecting which compensator states to retain when gain and phase critical regions exhibit high modal density. In such cases, small changes in the peaks and valleys, however small, near crossover frequencies become important to maintaining good stability margins and minimizing loop sensitivity. Placing the controller in tri-diagonal real modal form such that the states directly corresponded to compensator modes provided a good basis from which to reduce the controller. This permitted the state costs to be evaluated in terms of both their contribution to the shape of the overall transfer function and its local impact on gain and phase critical regions.

Finally, Chapter 4 discussed a variety of topics in optical and mechanical design to complete the ODL issues. In addition, Chapter 4 presented an optical cage suspension configuration as an alternative to the traditional inverted pendulum design. The alternate design utilizes axial flexures to provide a more true axial deflection in comparison to the combined axial and shear deflection of the inverted pendulum. The drawbacks to the axial flexures are local flexure stability issues which must be mitigated through careful flexure design and environmental testing. The pendulum flexures are traceable to past and future designs, however, since the destiffening pendulum effect vanishes on-orbit, the issue of frequency uncertainty in the optical cage

suspension must be addressed.

Due the the vast number of issues addressed by this work, the most important consideration in high performance ODL design is that it should be conducted from a multi-disciplinary perspective.

References

[1] Bahcall, J. N., "The Decade of Discovery in Astronomy and Astrophysics," tech. rep., National Research Council, 1991.

[2] Miller, D. W., S. L. Crawford, T. T. Hyde, B. P. Masters, E. F. Crawley, G. H. Blackwood, M. M. Colavita, J. W. Yu, M. Shao, and R. Laskin, "System-wide design issues for the Stellar Interferometry Technoilogy Experiment," *Proceedings, Spaceborne Interferometry II*, Orlando, FL, Vol. 2477, 1995.

[3] Holm, R. W., *A High-Speed, High-Resolution Optical Delay Line for Stellar Interferometry Applications*, Master's thesis, Department of Electrical Engineering, M.I.T., Cambridge, MA, 1986.

[4] Eldred, D. and M. O'Neal, "The JPL Phase B Testbed Facility," *Proceedings, ADPA Active Materials and Adaptive Structures Symposium and Exhibition*, 1991.

[5] Colavita, M. M., B. E. Hines, M. Shao, G. J. Klose, and B. V. Gibson, "Prototype High Speed Optical Delay Line for Stellar Interferometry," *Proceedings, SPIE Proc. Active and Adaptive Optical*, Vol. 21–23, 1991.

[6] Shao, M., M. M. Colavita, B. E. Hines, D. H. Staelin, D. J. Hutter, K. J. Johnston, D. Mozurkewich, R. S. Simon, J. L. Hershey, J. A. Hughes, and G. H. Kaplan, "The Mark III Stellar Interferometer," *Astron. Astrophys.*, Vol. 193, 1988, pp. 357–371.

[7] O'Neal, M., D. Eldred, D. Liu, and D. Redding, "Experimental Verification of Nanometer Level Optical Pathlength Control on a Flexible Structure," *Proceedings, Proc. Annual Rocky Mountain Guidance and Control Conf.*, Keystone, CO, 1991.

[8] Spanos, J. and Z. Rahman, "Optical Pathlength Control on the JPL Phase B Interferometer Testbed," *Proceedings, Fifth Annual NASA/DoD CSI Technology Conf.*, Lake Tahoe, NV, 1992.

[9] Crawley, E. F., B. P. Masters, and T. T. Hyde, "Conceptual Design Methodology for High Performance Dynamic Systems," *Proceedings, AIAA Proc. Structures, Dynamics and Materials*, New Orleans, LA, 1995.

[10] Miller, D. W., R. B. Sepe, E. Saarmaa, and E. F. Crawley, "The Middeck Active Control experiment (MACE)," *Proceedings, Fifth Annual NASA/DoD CSI Technology Conf.*, Lake Tahoe, NV, 1992.

[11] Glaese, R. and D. W. Miller, "On-Orbit Modeling of the Middeck Active Control Experiment from 1-g Analysis and Experiments," *Proceedings, 12th International Modal Analysis Conference (IMAC)*, 1994, pp. 1107–1113.

[12] Grocott, S., J. How, D. W. Miller, D. MacMartin, and K. Liu, "Robust Control Design and Implementation on the Middeck Active Control Experiment," *Journal of Guidance, Control, and Dynamics*, Vol. 17, No. 6, 1994, pp. 1163–1170.

[13] Smith, M. J., K. M. Grigoriadis, and R. E. Skelton, "Optimal Mix of Passive and Active Control in Structures," *Journal of Guidance, Control, and Dynamics*, Vol. 15, No. 4, 1992, pp. 912–919.

[14] Jacques, R. N. and D. W. Miller, "Physical Insight into the Simultaneous Optimization of Structure and Control," *Proceedings, Fifth Annual NASA/DoD CSI Technology Conf.*, Lake Tahoe, NV, 1992.

[15] Colavita, M., B. E. Hines, and M. Shao, "A High Speed Optical Delay Line for Stellar Interferometry," *Proceedings, ESO Proc. High Resolution Imaging by Interferometry II*, Garching, Germany, Vol. 15–18, 1991.

[16] Brogan, W. L., *Modern Control Theory*, Prentice-Hall, New Jersey, 1991.

[17] Grocott, S., *Comparison of Control Techniques for Robust Performance on Uncertain Structural Systems*, Master's thesis, Department of Aeronautics and Astronautics, M.I.T., Cambridge, MA, 1994.

[18] Jacques, R. N., *An Approach to the Preliminary Design of Controlled Structures*, Master's thesis, Department of Aeronautics and Astronautics, M.I.T., Cambridge, MA, 1991.

[19] Gregory Jr., C. Z., "Reduction of Large Spacecraft Models Using Internal Balancing Theory," *Journal of Guidance, Control, and Dynamics*, Vol. 7, No. 6, 1984, pp. 725–732.

[20] Skelton, R. E., P. C. Hughes, and H. B. Hablani, "Order Reduction for Models of Space Structures Using Modal Cost Analysis," *Journal of Guidance, Control, and Dynamics*, Vol. 5, No. 4, 1982, pp. 351–357.

[21] Blackwood, G., *Active Vibration Isolation for Controlled Flexible Structures*, Ph.D. thesis, Department of Aeronautics and Astronautics, M.I.T., Cambridge, MA, 1994.

2556-29